Veli Heikkinen

Tunable laser module
for fibre optic communications

Tunable laser module for fibre optic communications

Veli Heikkinen

VTT Electronics

Truth is the shattered mirror strown
In myriad bits; while each believes
His little bit the whole to own.

Richard F. Burton – Kasidah

Abstract

This thesis deals with the design, realisation, and testing of the wavelength tunable 1540-nm laser modules that are intended for fibre optic communications. The short external cavity laser uses an electrically controlled silicon micromachined Fabry–Perot interferometer (FPI) device as the tuning element.

First, the most common techniques for the diode laser wavelength tuning and applications for these devices are reviewed. Then the ways of coupling laser power into the single-mode (SM) optical fibre are considered and the characteristics of the fibre attachment methods are studied.

The design, assembly and testing of three prototypes is introduced. Their discontinuous tuning spans range between 8 and 13 nm and their output power between 100 and 570 µW. The modules produce multimode tuning having an rms spectral width of about 1 nm. In addition, one prototype is capable of single-mode tuning with a side mode suppression ratio of 26 dB. The measured wavelength span is threefold compared to our earlier work near 980 nm and the widest reported single-mode tuning range obtained from a short external cavity Fabry–Perot diode laser without temperature tuning. This is also the first directly modulated external cavity laser that has a 3dB bandwidth of over 600 MHz.

The study confirms that it is possible to realise the laser-to-SM-fibre coupling using adhesive bonding. Further studies are needed in order to improve the speed and repeatability of the assembly process together with the long-term reliability of the fibre attachment.

The prototype test results show that the FPI-tuned diode lasers have potential for applications where moderate performance suffices and low cost is mandatory. The hybrid arrangement uses standard laser components and therefore can

provide a cost-effective and easily configurable solution for fibre optic communication and sensor applications. However, before the device characteristics can be optimised the theoretical understanding of the FPI-tuned laser operation must be enhanced. In addition, the packaging techniques of the modules need to be improved taking into account both the reliability requirements and the cost of production.

Preface

Oulu, March 2004

Veli Heikkinen

Contents

List of symbols and abbreviations

3D   Three-dimensional

α Optical loss,
Parameter that relates to the spring force of the Fabry–Perot interferometer structure

α_f Far field divergence angle of the single-mode fibre

α_{fx} Far field divergence angle of the single-mode fibre in the x-z plane

α_{fy} Far field divergence angle of the single-mode fibre in the y-z plane

α_H Correction factor for diode laser line width

α_i Internal loss of the laser cavity

α_m End face mirror loss

α_s Far field divergence angle of the source

α_{sx} Far field divergence angle of the source in the x-z plane

α_{sy} Far field divergence angle of the source in the y-z plane

β Complex propagation constant, also called the wave number

$\Delta\lambda$ Change of wavelength,
Spectral width

$\Delta\lambda_{-20dB}$ Spectral width at the level that is 20 dB below the central peak

$\Delta\lambda_m$ Spacing between adjacent longitudinal modes

$\Delta\lambda_{MM}$ Wavelength separation between the interference maxima in the effective reflectance spectrum in multimode operation

$\Delta\lambda_{SM}$ Wavelength separation between the interference maxima in the effective reflectance spectrum in single-mode operation

$\Delta\lambda_{tune}$	Tuning wavelength range
$\Delta\nu_{STH}$	Schawlow–Townes–Henry line width for diode lasers
$\Delta\theta_x$	Angular misalignment tolerance in the x-z plane
$\Delta\theta_{x\_1dB}$	Angular misalignment tolerance in the x-z plane for 1 dB excess loss
$\Delta\theta_y$	Angular misalignment tolerance in the y-z plane
$\Delta\theta_{y\_1dB}$	Angular misalignment tolerance in the y-z plane for 1 dB excess loss
Δn	Change of refractive index
ΔT	Change of temperature
Δx	Misalignment tolerance in the x direction
Δx_{1dB}	Misalignment tolerance in the x direction for 1 dB excess loss
Δy	Misalignment tolerance in the y direction
Δy_{1dB}	Misalignment tolerance in the y direction for 1 dB excess loss
Δz	Misalignment tolerance in the z direction
Δz_{1dB}	Misalignment tolerance in the z direction for 1 dB excess loss
ε	Emissivity of the surface
ϕ	Half of the phase difference between successive multiple reflections in the Fabry–Perot interferometer
η	Coupling efficiency
λ	Wavelength
λ_0	Nominal laser wavelength
λ_c	Centre wavelength of the emission spectrum
λ_N	Wavelength of the Nth longitudinal mode of the laser

λ_p	Gain peak wavelength of the laser diode
ν	Frequency
θ	Angular misalignment of the fibre mode regarding the source mode
$\theta_{e,x}$	Angular misalignment in the x-z plane where the coupling efficiency falls off by 1/e
$\theta_{e,y}$	Angular misalignment in the y-z plane where the coupling efficiency falls off by 1/e
σ	Stefan–Bolzmann constant $\approx 5.67 \cdot 10^{-8}$ W/m^{2}K^4
$\tau_{a,x}$	Coupling efficiency in the x-z plane in perfect alignment
$\tau_{a,y}$	Coupling efficiency in the y-z plane in perfect alignment
τ_x	Coupling efficiency in the x-z plane
τ_y	Coupling efficiency in the y-z plane
ω	Angular frequency
A	Alignment product, Surface area, Cross-sectional area
a	Gain parameter
A_N	Normalised alignment product
AR	Anti-reflection
c	Speed of light in vacuum $\approx 3.0 \cdot 10^8$ m/s
CCD	Charge coupled device
CNR	Carrier-to-noise ratio
CWDM	Coarse wavelength division multiplexing

d	Offset misalignment of the fibre mode regarding the laser mode, Separation between the laser diode and Fabry–Perot interferometer
$d_{e,x}$	Lateral misalignment in the x-z plane where the coupling efficiency falls off by 1/e
$d_{e,y}$	Lateral misalignment in the y-z plane where the coupling efficiency falls off by 1/e
DBR	Distributed Bragg reflector
DFB	Distributed feedback
DH	Double-heterostructure
DOE	Diffractive optical element
DWDM	Dense wavelength division multiplexing
E	Energy
E_c	Minimum energy of the conduction band
EDFA	Erbium-doped fibre amplifier
E_F	Energy of the Fermi level
E_{Fc}	Energy of the quasi-Fermi level for electrons in the conduction band
E_{Fv}	Energy of the quasi-Fermi level for holes in the valence band
E_g	Energy gap between conduction and valence bands
E_i	Electric field amplitude of the Fabry–Perot interferometer input beam
E_p	Gain peak photon energy
ESEC	Extremely short external cavity
E_t	Electric field amplitude of the Fabry–Perot interferometer output beam

E_v	Maximum energy of the valence band
f	Focal length of the lens, Frequency
FBG	Fibre Bragg grating
FM	Frequency modulation
FMCW	Frequency-modulated continuous wave
FP	Fabry–Perot
FPI	Fabry–Perot interferometer
FTTC	Fibre to the curb
FTTH	Fibre to the home
FWHM	Full width between half maximum
g	Optical gain
GI	Graded index
GIF	Graded index fibre
GIO	Graded-index oval-core
g_p	Optical gain peak
GRIN	Graded index
H	Thickness of the material layer
h	Planck's constant $\approx 6.63 \cdot 10^{-34}$ Js
h_{conv}	Convection heat transfer coefficient
HFC	Hybrid fibre coax
HR	High reflection

I	Current, Irradiance
I_a	Current controlling the optical power of the tunable laser
IR	Infrared
I_t	Current controlling the emission wavelength of the tunable laser
I_{th}	Threshold current of the laser
ITU	International Telecommunication Union
j	Imaginary unit
k	Electron wave vector, Wave number of the radiation $= 2\pi/\lambda$, Thermal conductivity
k	Boltzmann's constant $\approx 1.38 \cdot 10^{-23}$ J/K
k_0	Free space propagation constant
L	Length of the laser cavity
l	Length of the Fabry–Perot etalon
l_0	Distance between the Fabry–Perot interferometer mirrors at zero control voltage
LD	Laser diode
LED	Light emitting diode
LTCC	Low-temperature co-fired ceramics
m	Order of interference
MEMS	Microelectromechanical systems
MM	Multimode

MQW	Multiple quantum well
N	Injected carrier density, Integer denoting the longitudinal mode number of the laser cavity
n	Refractive index
n'	Real part of the refractive index
n"	Imaginary part of the refractive index
NA	Numerical aperture
n_{air}	Refractive index of the air, $n_{air} \approx 1$
n_{AR}	Refractive index of the anti-reflection coating
$n_{cladding}$	Refractive index of the fibre cladding
n_{core}	Refractive index of the fibre core
n'_{eff}	Real part of the effective refractive index
$n_{g,eff}$	Effective group index that includes the dispersion of $n'_{eff}(\lambda)$
n_{Si}	Refractive index of silicon
n_{sp}	Spontaneous emission coefficient
N_{tr}	Transparency carrier density
O/E	Optical-to-electrical
OMI	Optical modulation index
P	Optical power
P_1	Optical power per laser facet
P_{conv}	Heat transfer rate in convection
P_D	Power dissipated in the laser chip

PD	Photodiode
P_{elec}	Electrical power
PM	Polarisation maintaining
QW	Quantum well
R	Radius of the Gaussian wavefront, Reflectance of the optical surface
R_1	Reflectance of the low reflection coated laser facet
R_2	Reflectance of the high reflection coated laser facet
R_3	Reflectance of the movable Fabry–Perot interferometer mirror
R_4	Reflectance of the stationary Fabry–Perot interferometer mirror
R_{eff}	Effective reflectance of the external cavity
R_f	Wavefront radius of the fibre mode
R_{FPI}	Reflectance of the Fabry–Perot interferometer
RIN	Relative intensity noise
rms	Root mean square
R_s	Wavefront radius of the source mode
s	Distance between the beam waist of the source mode and beam waist of the fibre mode
s_e	Axial misalignment where the coupling efficiency falls off by 1/e
SG-DBR	Sampled-grating distributed Bragg reflector
SM	Single-mode
SMSR	Side mode suppression ratio

T	Temperature
T_a	Total coupling efficiency between two perfectly aligned beams
TEC	Thermoelectric cooler
TEM	Transverse electric and magnetic
T_{FPI}	Transmittance of the Fabry–Perot interferometer
U	Voltage
U_{FPI}	Control voltage of the Fabry–Perot interferometer
U_{piezo}	Control voltage of the piezoelectric transducer
UV	Ultraviolet
VCSEL	Vertical cavity surface emitting laser
v_g	Group velocity of the photons
W	Fermi-Dirac occupation probability distribution, Width of the active region of the laser
w	Radius of the Gaussian beam
w_0	Beam waist radius of the Gaussian beam
$w_{0,x}$	Beam waist radius of the Gaussian beam in the x-z plane
$w_{0,y}$	Beam waist radius of the Gaussian beam in the y-z plane
w_{0f}	Beam waist radius of the fibre mode
$w_{0f,x}$	Beam waist radius of the fibre mode in the x-z plane
$w_{0f,y}$	Beam waist radius of the fibre mode in the y-z plane
w_{0s}	Beam waist radius of the source mode
$w_{0s,x}$	Beam waist radius of the source mode in the x-z plane

$w_{0s,y}$	Beam waist radius of the source mode in the y-z plane
W_c	Fermi–Dirac occupation probability distribution for electrons in the conduction band
WDM	Wavelength division multiplexing
w_f	Radius of the fibre mode
$w_{f,x}$	Radius of the fibre mode in the x-z plane
$w_{f,y}$	Radius of the fibre mode in the y-z plane
w_s	Radius of the source mode
$w_{s,x}$	Radius of the source mode in the x-z plane
$w_{s,y}$	Radius of the source mode in the y-z plane
W_v	Fermi–Dirac occupation probability distribution for holes in the valence band
x	Mole fraction of Ga in the $In_{1-x}Ga_xAs_yP_{1-y}$ quaternary alloy, Horizontal axis in the xyz Cartesian coordinate system
y	Mole fraction of As in the $In_{1-x}Ga_xAs_yP_{1-y}$ quaternary alloy, Vertical axis in the xyz Cartesian coordinate system
z	Longitudinal axis in the xyz Cartesian coordinate system
z_f	Distance between the wavefront and beam waist of the fibre mode
z_s	Distance between the wavefront and beam waist of the source mode
Z_T	Thermal impedance

1. Introduction

1.1 Background and motivation

The research into fibre optic communications at VTT Electronics began at the end of the 1980s. At that time we studied both the intra-machine communications using multimode (MM) fibres and the packaging technology of single-mode (SM) laser sources applied in long-haul telecommunications. The studies of the intra-machine data transfer concentrated on the passive bi-directional bus having a maximum speed of 1 Mbit/s and network size of 30 to 500 m (Karioja et al. 1989, Karioja et al. 1995). The objective of the packaging research was to realise prototypes of the SM fibre coupled 1,310 nm band laser modules capable of transmitting up to 565 Mbit/s (Heikkinen et al. 1991). Both of these studies clearly showed that, due to looser alignment tolerances, MM fibre modules are much easier to realise than SM components.

Since the 1980s our work with optical fibres has continued in several projects, where the main focus has been in the realisation of fibre optic sensors and instruments. At present our competence in MM fibre packaging is reasonable (Karioja et al. 2000), whereas capabilities in the SM technology are much weaker. One of the main challenges is how to effectively couple light from the source into the SM fibre and control the stringent alignment tolerances of the critical components.

Today, despite the recent depression, there is a great deal of interest in developing optical networks to support the increasing bandwidth demand of applications such as analog and digital television, telephone, teleworking, video conferencing and Internet browsing (Bonenfant and Rodriguez Moral 2002, Day et al. 2002, NEMI 2002, Rodriguez Moral et al. 2000). When using both the 1,310 nm and 1,550 nm transmission windows, optical fibre provides a huge bandwidth of 50 THz with a low loss of 0.5 dB/km (Borella et al. 1997). Fibre is also thin, flexible, reliable in a corrosive environment and immune to electro-magnetic interference. However, in order to fully exploit this bandwidth, developers must first realise switching equipment, such as all-optical switches that can route individual data packets in the optical domain (Morris 2001).

Currently, the maximum data rate for one wavelength is 10 Gbit/s (Hecht 2002), which is less than 10^{-3} of the potential fibre bandwidth. Therefore, wavelength division multiplexing (WDM) is one promising approach to taking better advantage of the fibre transmission capacity. In WDM the optical transmission spectrum is divided into a number of non-overlapping wavelength bands. Each wavelength supports a single communication channel that can operate at the maximum speed of the electronics (Laude 2002, p. 3).

Dense wavelength division multiplexing (DWDM) has been very successful in long-haul telecommunications. For example, the "EuroRings" network spans over 15,000 km and connects 41 European cities, including Helsinki (Harroff 2001). Its Nordic Ring consists of 96 fibre strands capable of delivering 80 wavelengths per fibre at 10 Gbit/s per wavelength. So, its total transmission capacity is almost 80 Tbit/s. DWDM also has potential for applications in metropolitan-area networks (Balnicki 2001, Wilson et al. 1999).

The rapid progress in optical communications motivated VTT Electronics to launch the strategic project "Optical Technologies for Wireless Communications" in 2000. The purpose of this project was to strengthen our compentence in optical technologies. One of the project tasks was named "Tunable laser for DWDM applications", where the objective was to realise prototypes of the wavelength tunable SM fibre coupled laser modules.

The development of tunable lasers is justified because they can save money by simplifying the spare part inventory while making the optical networks more flexible (Bruce 2002, Coldren et al. 2004, NEMI 2002). Current WDM transponders incorporate fixed lasers operating near 1,550 nm and a 160-wavelength system must store 160 reserve transponders as spares to fix failures. One tunable laser can serve as a backup for multiple channels, so fewer modules need to be stocked.

Secondly, fibre optic networks have been fixed, offering little reconfigurability, which makes it impossible to change the deployment of the capacity in real time. One problem is the difficulty in choosing a wavelength for a channel, because as traffic is routed through the network some wavelengths may already be in use in certain links. Tunable lasers will facilitate switching to alternative channels without changing the hardware or reconfiguring the network resources. Tunable

lasers can also provide flexibility at multiplexing locations, where wavelengths are added to and dropped from the fibres, by letting the carriers remotely reconfigure additional channels as necessary. This helps the operators to satisfy different customer requirements and manage wavelengths and transmission bandwidths throughout the networks more effectively (Bruce 2002).

Because of the potential importance of the tunable lasers for future all-optical networks, their market forecasts have been optimistic. The Yankee Group predicted that the market would jump from USD 50 M in 2001 to USD 2,300 M by 2005 (Fuller 2001). This seems to be rather optimistic, because the total worldwide diode laser sales in 2002 were just USD 2,400 M. The telecommunications segment covered USD 665 M, out of which lasers operating in the range 980 to 1,550 nm encompassed 94 % and comprised 1.8 million units (Steele 2003). Some analysts believe that tunable lasers will not see volume deployments for another two to three years because carriers are concerned about the long-term reliability of the devices (Fuller 2001).

The tuning operation of the module described here rests on the extremely short external cavity (ESEC) principle, where a movable mirror is placed very near the anti-reflection (AR) coated diode laser facet. In this thesis ESEC means that the external cavity length is less than about 100 µm. The invention made at VTT Electronics applies an electrostatically tunable silicon micromachined Fabry–Perot interferometer (FPI) device as the moving mirror (Figure 1).

The advantage of this configuration is the possibility of using off-the-shelf components; thus it is potentially inexpensive in small to medium-sized production volumes (Sidorin et al. 1999a). The structure of the FPI (Pat. US 5,561,523 1996) and the principle of the ESEC laser using the FPI have been patented (Pat. US 6,192,059 2001). So far, we have demonstrated the operation principle of the ESEC laser and obtained a tuning range of 4 nm near the 980-nm wavelength (Aikio and Karioja 1999, Sidorin et al. 1999b).

The prototype described in this thesis was designed to operate in the 1,550-nm band. It has the potential for use in wavelength division multiplexing applications, such as the up-link transmitter in the hybrid fibre coax (HFC) networks (Rantanen 2000, Järvenpää 2001). Thus the concrete motivation for

my work was to determine the performance of the FPI-tunable laser and evaluate its feasibility for the HFC up-stream applications.
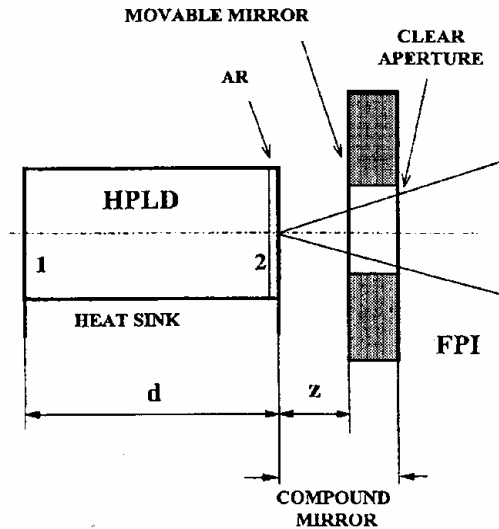
Figure 1. Principle of the FPI-tuned laser (Sidorin et al. 1999a).

1.2 Scope and objectives of the thesis

This thesis reviews principal tunable diode laser types and presents the prime details of the design, realisation and testing of the novel fibre-coupled laser modules. These prototypes apply the short external cavity principle and use the silicon micromachined Fabry–Perot interferometer device as the tuning element.

Module integration is teamwork, and many of the people that are acknowledged in the preface participated in the development of the prototypes. Working as the task manager meant taking part in all activities, although my personal studies focused on the optical coupling between the laser diode and single-mode optical fibre and the evaluation of the prototype performance. This included the survey of the characteristics of different coupling methods, and the measurements and analysis of the realised alternatives, and all the prototype measurements presented here.

The fundamental characteristics of tunable lasers were studied from the viewpoint of an engineer rather than that of a physicist. This meant that the key phenomena behind the laser operation was only introduced at an elementary level so the reader could better understand the operational parameters and performance trade-offs of the various schemes. The actual modelling of the FPI-tuned laser characteristics was carried out by the other team members (Aikio 2004), thus it is only presented very briefly here.

The discussion concerning the prototype design is restricted to issues of the first level packaging – that is, module packaging (Tummala and Rymaszevski 1989, p. 7). Here, the optical elements, electrical components in chip or submount form, and the mechanical parts are integrated into a single module. In real-life communications applications the module will first be assembled onto a printed circuit board that will then be inserted into the device cabinet. The issues relating to the packaging of these second and third levels have been left out of this thesis.

The main objective of this thesis is to concisely present how the FPI-tunable fibre-coupled laser module was realised and what the main characteristics of the prototypes were.

1.3 Contribution of the thesis

This thesis brings together information on the areas of optics, electronics, mechanics and module packaging, and uses it in the design and realisation of the novel tunable laser prototypes. The main elements of this thesis are:

❑ This thesis reviews the characteristics of various laser to SM fibre coupling methods, and shows how the desire for the high coupling efficiency leads to tight alignment tolerances of at least one of the coupling components.

❑ This thesis presents an analysis of the chosen laser to SM fibre coupling options and compares the simulations with the measurements. The results confirm that at least in simple cases modern simulation software can reasonably well forecast the fibre coupling efficiency and alignment tolerances of the components.

❑ This thesis reviews the alternatives commonly used in the attachment of the SM fibres, and shows that only a few publications deal with adhesive bonding. The thesis confirms that it is possible to realise fibre attachment using ultraviolet (UV) curable adhesives, although further studies are needed in order to improve the process yield and device reliability.

❑ This thesis summarises the design, realisation and testing of the novel tunable laser modules. It is easy to find information that present laboratory measurements of laser characteristics or tuning behaviour, details of optical design, peculiarities in laser welding or soldering processes, etc. However, it is hard to find publications that describe how complete modules were designed, assembled and tested.

❑ This thesis shows that the FPI-tunable modules have potential for fibre optic applications where moderate performance suffices and low cost is mandatory. The measured wavelength span is threefold compared to our earlier work near 980 nm and the widest reported single-mode tuning range obtained from a short external cavity Fabry–Perot diode laser without temperature tuning. This is also the first directly modulated external cavity laser that has a 3dB bandwidth of over 600 MHz.

2. Fibre optic communications

2.1 Evolution of fibre optic communications

Glass fibres have a long history. The Egyptians were making coarse fibres by 1600 BC and using them as decorations on pottery. In the Renaissance period, Venetian glass makers employed fibres to decorate the surfaces of glass vessels. During the 19th century glass fibres were woven into fabrics or assembled into imitation ostrich and egret feathers to decorate hats. These fibres were brittle, ragged and less than three meters in length, and therefore had little practical use (Hecht 1999a, p. 29).

The basic concept of the total internal reflection lying behind fibre optics was first documented in the 1840s when scientists used jets of water to guide light in laboratory demonstrations, Figure 2 (Colladon 1842). The idea was used during the second half of the 19th century to create impressive illuminated fountains at many of the European and American exhibitions (Hecht 1999a, p. 16). The total internal reflection was also observed to work with bent glass rods, and Babinet proposed the application of dental illuminators (Babinet 1842).
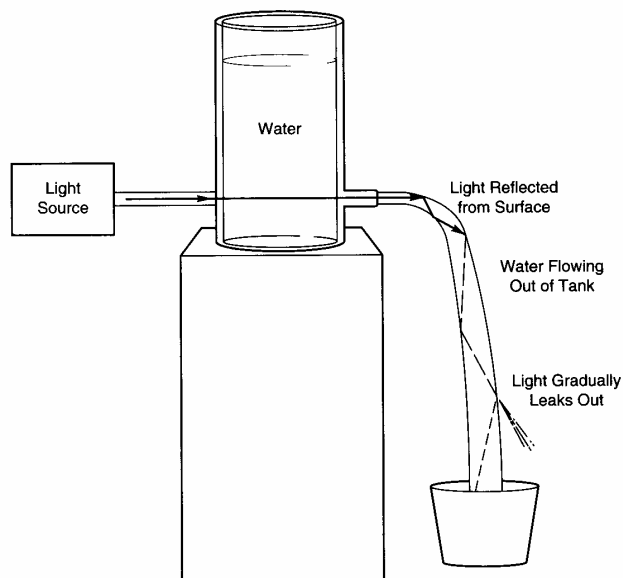

Figure 2. Light guided down a water jet (Hecht 1999b, p. 4).

The use of flexible glass fibres to transmit light was introduced in the first half of the 20th century. One of the earliest applications was the endoscope, which allowed physicians to look inside the body without surgery. Because the fibres were unclad, the quality of the obtained images remained poor until the 1950s, when Møller Hansen realised the importance of the fibre cladding (Hecht 1999a, p. 50).

The invention of the ruby (Maiman 1960) and semiconductor lasers (Hall et al. 1962) created a growing interest in optical communications. The diode lasers were particularly attractive because changing the drive current modulated their optical power and their small size made it possible to build compact solid-state transmitters. Unfortunately, the performance of the first laser diodes was very poor. They only operated at liquid nitrogen temperature (−196ºC), needed drive currents of 100 amperes, produced short 10 µs pulses with low repetition rates, and burned out quickly and unpredictably (Hecht 1999a, p. 147). Also, the attenuation of the fibres was high, about 1 dB/m at best, preventing their use in telecommunications.

When Kao thoroughly analysed the absorption and scattering characteristics of glass (Kao and Hockham 1966) and Jones delicately measured them (Jones and Kao 1969), it became obvious that the attenuation of pure silica is very low. Soon after this, Corning developed the first low-loss optical fibre that had attenuation lower than 20 dB/km (Kapron et al. 1970). Because this fibre had a titanium dioxide (TiO_2) doped silica core with a pure silica cladding, its manufacturing process required several heating and cooling processes to make the titanium transparent, which made the fibre fragile (Hecht 1999a, p. 145). Corning solved the problem by replacing TiO_2 with germanium oxide (GeO_2) and produced the first practical telecommunication fibre (Keck et al. 1973).

The characteristics of the semiconductor lasers also improved gradually. The first laser diodes were made of one material comprised of p- and n-type gallium arsenide (GaAs). The efficiency of the laser action increased and the threshold current decreased when a layer of gallium aluminium arsenide (GaAlAs) was placed next to the p-n junction, forming a heterojunction laser (Rupprecht et al. 1967). These lasers operated at room temperature but could only produce short, low repetition rate pulses. Finally, the continuous wave operation was attained in 1970 when the double heterojunction laser was realised (Hayashi et al. 1970).

Since the first half of 1970s fibre optic telecommunications has developed rapidly. The experimental links were tested on live telephone traffic in 1977, and within the next ten years long-distance companies were laying fibre cables for their national backbone systems (Hecht 1999a, p. 181).

The first generation of fibre optic communications used GaAlAs light emitting diodes (LED) or lasers working around 850 nm and graded index multimode fibres. Multimode fibre was preferable to single-mode technology because of its looser source-to-fibre and fibre-to-fibre alignment tolerances. In addition, the material dispersion of silica is fairly large at 850 nm, which reduced the bandwidth advantage of SM fibre over the MM waveguide. The systems were capable of transferring digital signals up to 140 Mbit/s over distances of several kilometers (Berry et al. 1978).

The next window having lower fibre attenuation (Figure 3) and material dispersion opened when indium gallium arsenide phosphide (InGaAsP) LEDs and lasers were developed (Hsieh and Shen 1977). At the beginning of the 1980s telephone companies began to install the second generation systems using laser sources and graded index fibres that extended transmission distances up to tens of kilometers and provided data rates of tens Mbit/s (Hecht 1999a, p. 193).
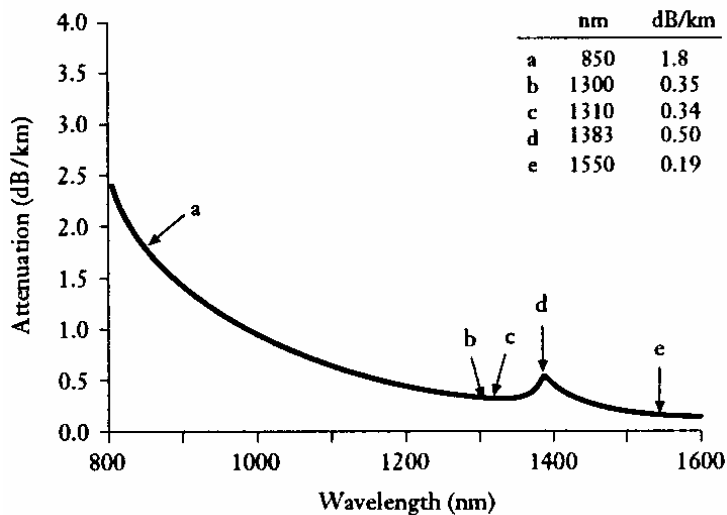

Figure 3. Spectral attenuation of SM silica fibre (Corning 2002).

Shortly after this, the third generation, based on single-mode technology, superseded graded-index fibres. Now the transmission speed of 1,310 nm could be increased up to 565 Mbit/s and simultaneously obtain a repeater spacing of about 50 km (Smith 1982). British Telecom installed the first single-mode systems in 1983, and the first transatlantic fibre-optic cable (TAT-8) connecting Europe to North America started to operate in 1988 (Hecht 1999a, p. 213).

The fourth generation systems operate in the 1,550-nm window, where silica fibres have the minimum attenuation. This made it possible to lengthen repeater spacings to over 100 kms, which could be further extended after the invention of erbium-doped fibre amplifiers (EDFA) (Mears et al. 1987). Although the material dispersion of silica is higher at 1,550 nm than at 1,310 nm, transmission speeds could be increased up to several Gbit/s by developing narrow line-width lasers and external modulation techniques together with faster transmitter and receiver electronics (Korotky et al. 1987, Linke 1984, Okiyama et al. 1988).

When reviewing the evolution of optical fibre technology, we can say that today fibre optics is the key element in global telecommunications. For example, in the year 2000 there was 580,000 km of undersea optical cables that carried 80 % of the total transoceanic communications (Mandell 2000). Single-mode fibres take care of the long-distance high capacity traffic, whereas graded-index multimode fibres usually serve in the short-span systems such as intra- and inter-office links (Hecht 1999b, p. 435).

Because EDFAs have bandwidths of tens of nanometers, transmission speeds in the 1,550 nm window can be raised using wavelength division multiplexing. Current submarine cables operate at 10 Gbit/s using 42 wavelengths, giving a total capacity of 420 Gbit/s per fibre (Mandell 2000), and laboratory experiments have surpassed the Tbit/s limit (Gnauck et al. 2002, Charlet et al. 2003).

Despite the great success of the long-haul fibre optic telecommunications, the worldwide high-speed optical network is not complete until it can deliver its traffic all the way to and from people's homes. The applications consist of analog and digital television, telephone and Internet browsing, and new demands that will arise in the future. How this network will be implemented is an elaborate and interesting problem.

2.2 WDM systems

Wavelength division multiplexing has become important because it can multiply the transmission capacity of the fibre without installation of new cables. WDM is analogous to the frequency division multiplexing used in radio wave transmission, where many signals are sent through the same media at different carrier frequencies.

Wavelength division multiplexing combines signals at different wavelengths to travel through a single fibre. A simplified view of the WDM system using four wavelengths is depicted in Figure 4. Signals pass along the shared fibre with minimal interaction to the demultiplexer, which separates and routes them to their individual destinations.
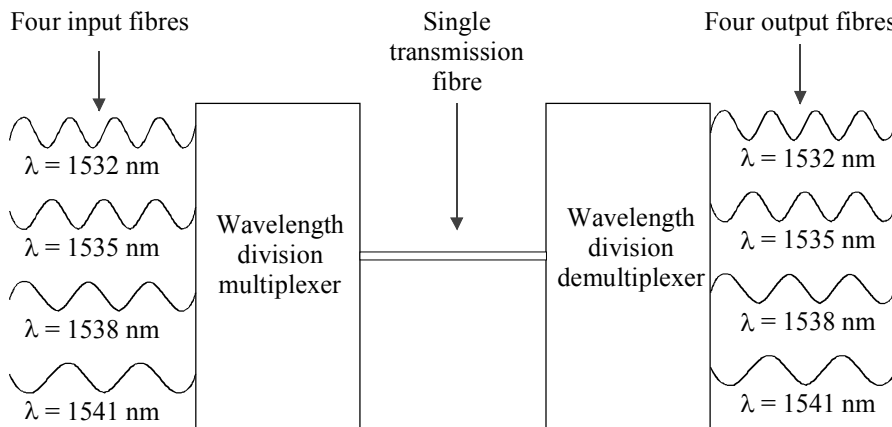
Figure 4. Principle of wavelength division multiplexing.

Operational WDM systems include several other components that are not shown in Figure 4, such as light sources, modulators, amplifiers, regenerators, splitters, switches, routers, filters and receivers. Readers interested in this subject can obtain information on the principles and components from (Kartalopoulos 2000, Laude 2002), and on the optical networks from (Goralski 2001).

The first practical WDM communication applications appeared in the early 1980s (Laude 2002, p. 245). These networks used multimode fibres and, often, only two wavelengths, 800 nm and 1,300 nm. It soon became obvious that the

use of SM fibres was necessary to achieve the bandwidth required in high bit rate connections.

Present telecommunication DWDM systems operate in the 1,550-nm window, where they can utilise erbium-doped fibre amplifiers. The International Telecommunication Union (ITU) has set a DWDM standard in which the base frequency is 193.1 THz ($\approx$ 1,552.5 nm) and the spacing between adjacent channels 100 GHz or its multiples or submultiples. The 100 GHz grid corresponds to about 0.8-nm wavelength separation (ITU 1998). At this moment, the smallest grid is 12.5 GHz and covers approximate nominal central wavelengths from 1,530.04 to 1,624.89 nm (ITU 2002).

ITU has also set a global standard for coarse wavelength division multiplexing (CWDM) applications. This grid covers wavelengths from 1,271 to 1,611 nm and supports 18 channels with a 20-nm spacing. The standard is targeted to cost-sensitive applications, such as metropolitan networks and designed to permit the use of uncooled sources with relaxed wavelength selection tolerances along with wide passband filters (ITU 2003).

Many attempts have been made with a variety of architectures to realise fibre to the curb (FTTC) serving 10 to 20 homes, or fibre to the home (FTTH) networks (Wilson et al. 1999). The idea behind the extensive use of fibre optics is to reduce the number of active components between the headend facility and the subscribers, thus ensuring reliability, sufficient capacity and quality in signal transmission. Actual deployments have been limited primarily because of the difficulty of generating enough revenue on these networks to justify their high installation costs.

Installing fibre optics deep into the network also allows the hybrid fibre coax operators to build up their systems with various interactive services in mind (Järvenpää 2001, Ovadia 2001, Rantanen 2000). The implementation of these services requires network segmentation and return path technology, Figure 5.

Here, the fibre optic receivers (O/E) convert the broadband optical downlink signals to an electronic form that is compatible with the coaxial cable networks assembled to the buildings. When introducing data access services, the cable operators must implement upstream transmission into the HFC networks. This

can be realised with return path transmitters using electrical frequencies from 5 to 300 MHz and operating at the 1,310 nm or 1,550-nm wavelength band can be added into the O/E blocks. The total uplink capacity can be upgraded using CWDM or DWDM transmitters.
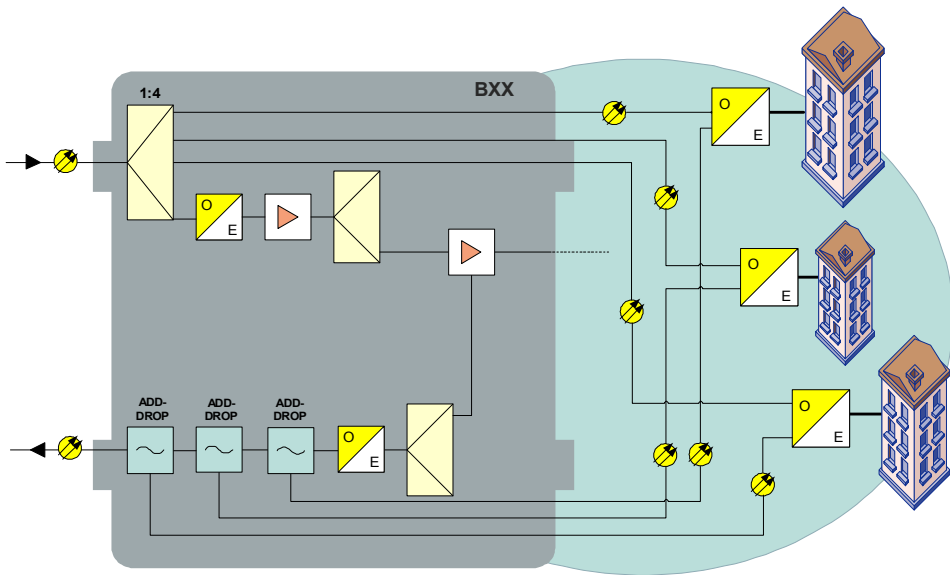

Figure 5. Example of the HFC network (courtesy of Teleste Corp.).

3. Tunable laser diodes

Laser diodes were first reported in 1962, when it was also noticed that changing their drive current shifts the emission spectrum (Hall et al. 1962). At the beginning of the 1970s temperature-tuned diode lasers operating in the vicinity of 10 µm were proposed for the detection of air pollution gases, such as ethylene, N_2O, and SO_2 (Hinkley and Kelley 1971, Norton et al. 1971). In those days Soviet scientists also demonstrated the external cavity tuning of a GaAs laser operating at the 900-nm band (Bogatov et al. 1973).

This chapter reviews some of the techniques developed to realise tunable laser diodes, which can be divided into two principal classes: monolithic structures and external cavity lasers. The literature dealing with tunable diode lasers is vast; by 1998 over 1,000 papers had been written about them (Amann and Buus 1998, p. xi). Since then the interest in research has further increased and laser characteristics are developing rapidly. Therefore, the review mainly concentrates on recently introduced structures that have lead to commercial components used in fibre optic transmission systems.

For those readers who are not familiar with the physics of diode lasers or tuning schemes, there is a short introduction in Appendix A. The fundamental characteristics of tunable lasers were studied from the viewpoint of an engineer rather than that of a physicist. This meant that the key phenomena behind the laser operation was only introduced at an elementary level so the reader could better understand the operational parameters and performance trade-offs of the various schemes. This information may be helpful when comparing the performance of the FPI-tuned prototype with other tunable lasers.

3.1 Monolithic tunable lasers

From a practical point of view, compact and robust laser sources with simple handling are preferred. Therefore, tunable lasers that can be produced as monolithically integrated devices are favoured. Three basic monolithic architectures exist: distributed feedback (DFB), distributed Bragg reflector (DBR), and vertical cavity surface emitting lasers (VCSEL).

3.1.1 DFB lasers

Distributed feedback grating structures were proposed in the early 1970s and the principle was soon applied to semiconductors (Laude 2002, p. 86). Today, DFB lasers are used in almost all installed DWDM networks. A grating is formed along the active layer in these lasers, Figure 6. The grating reflects a single wavelength back into the cavity, inducing only one resonant mode within the laser, and producing a stable, very narrow, bandwidth output. The period of the grating controls the wavelength at which the feedback occurs.
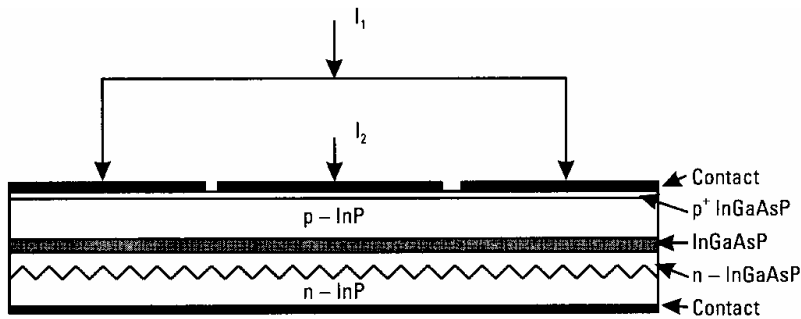

Figure 6. Multisection tunable DFB laser for 1,550 nm (Laude 2002, p. 87).

DFB lasers are tuned by changing the cavity temperature that alters the refractive index, which tunes the operating wavelength: $\Delta n/n = \Delta\lambda/\lambda$ (Delorme 1998). Because the obtainable index modulation is quite small (Table 1), a large temperature difference is required to tune across only a few nanometers. For example, in Nortel's LCW508ET the 3-nm tuning is achieved by varying the laser temperature from 0 to 40 °C (Nortel 2002a).

Because the tuning range of one cavity is small, typically under 5 nm, DFB lasers with wide tuning ranges incorporate multiple cavities. In Nortel's three-cavity module the grating pitches in DFB sections are chosen to produce emission at increasing wavelengths, in steps of 4.8 nm (Adams et al. 2001). A particular ITU frequency is accessed by selecting the DFB section that has the emission wavelength nearest to the target frequency and then adjusting the chip heatsink temperature. The DFB sections that lie between the operating one and the output fibre are biased to transparency. A continuous tuning of 5 nm is achieved by changing the chip temperature from − 5 to + 50 °C.

Table 1. Refractive index change and switching speed of different phenomena used in tunable lasers (Delorme 1998).

Phenomenon	Refractive index change ($\Delta n/n$)	Switching speed	Associated effects
Carrier injection	~ 0.01	Few ns	Low output power and large line width variations
Thermal heating	~ 0.01	Few ms	Large output power and low line width variations
Electro-refraction	~ 0.002	~ 100 ps	Large output power variations

For a really wide tuning range, several multicavity lasers, each spanning a different wavelength range, can be integrated into one unit, Figure 7. Control electronics are used to select and operate one of the multiple cavities and to adjust its temperature. The electronics used for stability control and wavelength selection are integrated on a single silicon substrate with the laser diode chip.
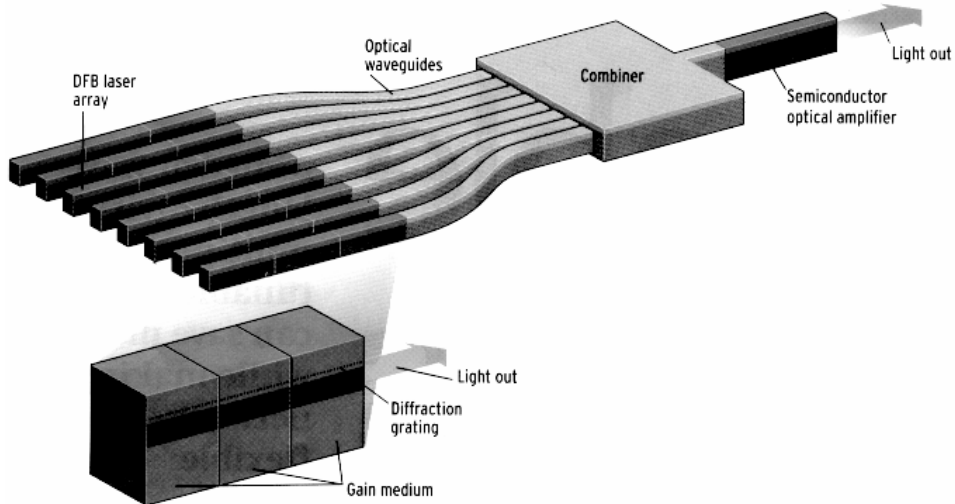

Figure 7. Wide tuning range DFB laser structure from Fujitsu (Bruce 2002).

The NEC Corporation reports a monolithically integrated wavelength-selectable source containing a four-element DFB-laser array, a coupler, a semiconductor optical amplifier and an electro-absorption modulator. Each laser can cover a range of 2.6 nm when the temperature is varied from 10 to 40 °C. The array tunes over a wavelength range of 9.5 nm and couples more than 20 mW into a SM fibre (Morimoto et al. 2002).

NTT Photonics Laboratories has demonstrated a wavelength-selectable array consisting of 16 DFB lasers and having a quasi-continuous tuning range of 47 nm. When the chip temperature changes from 19 to + 48 °C, the lasing wavelength of each laser tunes by 3 nm (Tohmori et al. 2002).

Santur Corp. uses a DFB laser array and a tilt mirror made by microelectro-mechanical systems (MEMS) technology, Figure 8. Here the MEMS mirror selects the laser, whose wavelength is tuned by the chip temperature. The mirror also loosens the assembly tolerances, since the fine optical alignment is done electrically. The authors report a total tuning range of 33 nm with a channel spacing of 50 GHz and a tuning time of 1 s (Pezeshki et al. 2002).
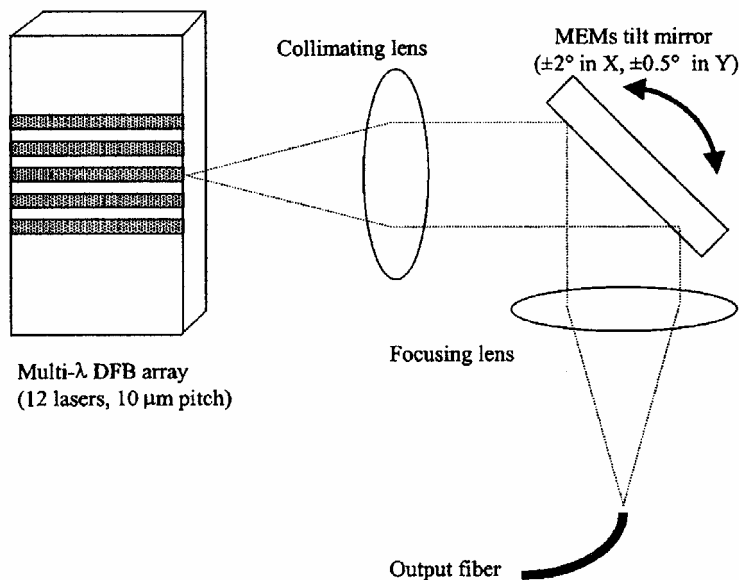

Figure 8. Widely tuned DFB laser using a MEMS mirror (Pezeshki et al. 2002).

The characteristics of commercial DFB laser modules for transmission systems are shown in Table 2 (Alcatel 2002, Fujitsu 2000, JDS Uniphase 2002, Nortel 2002a). The references of this thesis give more information concerning the DFB lasers of Fujitsu (Miyata et al. 2000) and Nortel (Adams et al. 2001).

3.1.2 DBR lasers

In the distributed Bragg reflector lasers the grating is placed outside the active region, which simplifies the epitaxial process. The device may use two gratings or one grating with the reflection from the other cleaved cavity facet. In a typical tunable DBR structure the refractive index of the grating section is controlled either thermally or by injection current, and there is normally a phase control section between the grating and the gain section, Figure 9. The phase section aligns a cavity mode with the reflection peak, and so does the fine-tuning.
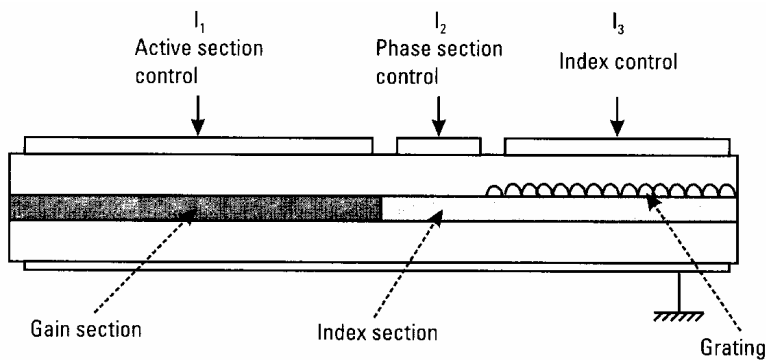
Figure 9. Principle of DBR laser (Laude 2002, p. 89).

The tuning range in standard three-section DBR lasers seldom exceeds 10 nm. Wider tuning ranges can be achieved using a specialised structure, called a sampled grating, which incorporates periodically spaced blank areas (Bruce 2002). A tunable sampled-grating DBR (SG-DBR) laser uses several such gratings with different blank area spacing. During tuning, the gratings are adjusted so that the resonant wavelengths of each grating are matched.

Since tuning with the sampled-grating technique is not continuous, the circuitry for controlling multiple sections is more complex than in standard DFB lasers,

Figure 10. The output power is typically less than 10 mW, but SG-DBR lasers can have a wide tuning range and high side mode suppression (Shi et al. 2002).
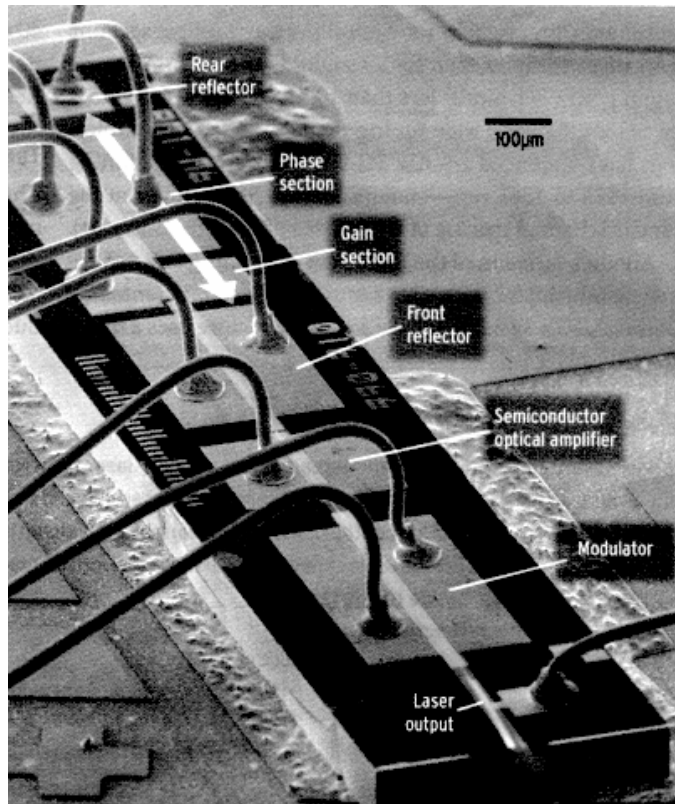
Figure 10. SG-DBR device from Agility Communications (Bruce 2002).

There is one DBR laser-related project in the 5th framework programme of the European Community. The objective of the NEWTON (New Widely Tunable Lasers for Optical Networks) is to develop new types of widely tunable laser diodes. At least two structures will be realised, the sampled grating Y-branch laser and the SG tunable twin-guide laser (Newton 2001, Wesström et al. 2002).

The characteristics of commercial DBR laser modules for transmission systems are shown in Table 2 (ADC 2002, Agere 2002, Agility 2002, Multiplex 2002). The references to this thesis give more information concerning the DBR lasers of ADC (Wesström et al. 2001), Agere Systems (Ackerman et al. 2001) and Agility (Mason et al. 2000).

Table 2. Characteristics of commercial tunable DFB and DBR laser modules for transmission systems.

Manufacturer	Base technology	Available wavelength range (nm)	No. of channels @ ITU spacing (GHz)	Maximum output power (mW)	Wavelength tuning speed (ms)	Modulation bit rate (Gbit/s)
ADC	DBR	1,530 ... 1,561	160 @ 25	≥ 2	2	$-^a$
Agere Systems	DBR	1,529 ... 1,564	20 @ 50	≥ 0.6	$-$	≤ 2.5
Agility	DBR	1,525 ... 1,565	81 @ 50	4	< 10	$-^a$
Alcatel	DFB	$-$	8 @ 50	20	$-$	$-^a$
Fujitsu	DFB	1,529 ... 1,607	4 @ 100	10	$-$	$-^a$
JDS Uniphase	DFB	1,527 ... 1,610	2 @ 100	10	$-$	≤ 2.5
Multiplex	DBR	$-$	16 @ 50	1.6	< 0.01	10
Nortel	DFB	1,528 ... 1,605	8 @ 50	20	$-$	$-^a$

[a] Module is used with an external modulator.

3.1.3 Vertical cavity lasers

Vertical cavity lasers are based on a quantum well active region inside a short cavity consisting of stacked mirrors made from multiple $\lambda/4$ layers. They generally emit a circular diffraction-limited beam with a low numerical aperture. Therefore, VCSELs can be coupled to optical fibres more easily and efficiently than edge-emitting lasers. Due to the small active volume, their typical threshold current is in the order of 1 mA. VCSELs offer single longitudinal mode operation, low power consumption, and enable wafer-level testing and burn-in, resulting in a lower device cost. In addition, they can potentially be integrated into two-dimensional arrays.

VCSELs have been commerically available at 850 nm for several years. However, the low index contrast and poor thermal conductivity of the lattice-matched DBR mirrors have hampered the use of InP-based devices in the longer wavelengths (Boucart et al. 2003). At present, GaAs substrate is believed to be a candidate for 1.3 µm VCSELs, because it is compatible with the growth of lattice-matched GaAs/GaAlAs DBR mirrors that have excellent reflectivity (Dowd et al. 2003, Tan 2002).

The tuning of VCSELs is based on mechanical modification of the laser cavity using MEMS technology, Figure 11. With MEMS, a movable mirror can be fabricated at one end of the cavity. VCSELs have achieved relatively wide tuning ranges up to 30 nm. The main challenges for tunable VCSELs are single-mode output power limitations, chirp, long-term reliability of the tuning mechanisms, and the cost of volume manufacturing (Bruce 2002, NEMI 2002).

There is one tunable VCSEL project in the 5th framework programme of the European Community. The objective of the TUNVIC (Micromechanical Widely Tunable VCSEL for WDM Telecommunication Systems) is to develop a laser source that is tunable from 1,530 to 1,565 nm with a 100 GHz channel spacing and has a tuning speed faster than 100 µs and output power higher than 0.5 mW (Halbritter et al. 2004, Tarraf et al. 2004, Tunvic 2001).

The characteristics of some commercial tunable VCSELs for transmission system applications are shown in Table 3 (Bandwidth9 2002, Nortel 2001,

Nortel 2002b). The references to this thesis give more information concerning the VCSELs of Bandwidth9 (Boucart et al. 2003, Kner et al. 2003, Li et al. 2001) and Nortel (Jiang et al. 2001, Knopp et al. 2001).
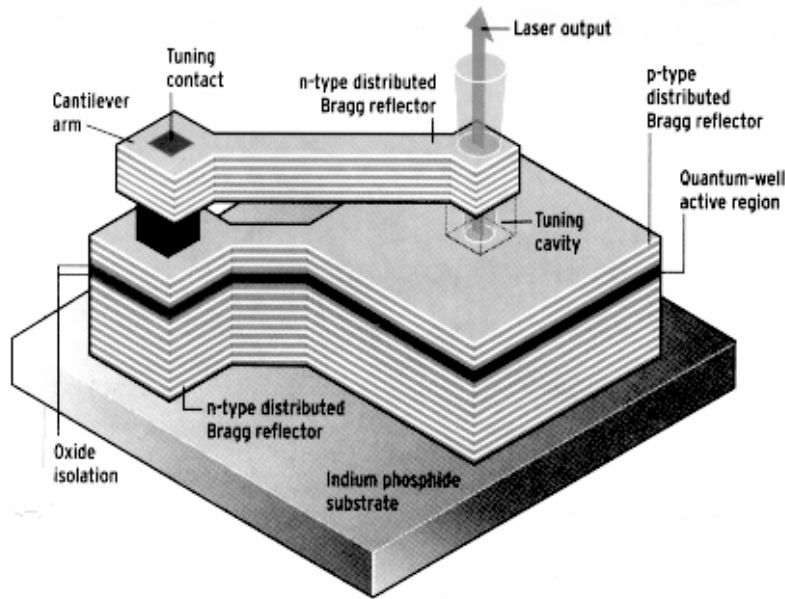
Figure 11. Tunable VSCEL structure from Bandwidth9 (Bruce 2002).

3.2 External cavity tunable lasers

External cavity diode lasers contain a cleaved facet on one side and a wavelength selective reflector, usually a grating, on the other side. Adjusting the wavelength selective component in the correct way produces the desired wavelength. External cavity lasers with a long cavity can produce high output powers, have the narrowest line width and are easily tunable over the gain spectrum of the active material (Laude 2002, p. 91). They are, therefore, widely used in optical testing and measuring equipment (Bruce 2002). However, their reliability as telecommunication sources has been questionable due to their thermal and mechanical instabilities.

The Littman-Metcalf external cavity laser uses a diffraction grating and a movable reflector, Figure 12. This design has the advantage that it can be built

around a standard and fairly inexpensive laser diode. The movable reflector enables a wide tuning range but with a low tuning speed. External cavity lasers can achieve tuning ranges greater than 40 nm but their tuning speed is fairly low, Table 3. Typically, it takes tens of milliseconds to change the wavelength (Bruce 2002).
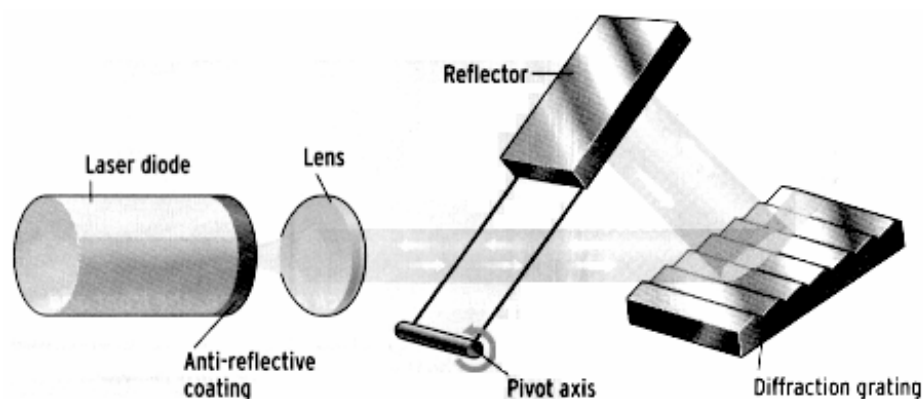
Figure 12. Littman-Metcalf external cavity laser from New Focus (Bruce 2002).

The characteristics of commercial tunable external cavity lasers for transmission system applications are shown in Table 3 (Blue Sky 2002, Iolon 2002, New Focus 2001). The references to this thesis give more information concerning the external cavity lasers of Iolon (Berger et al. 2001) and New Focus (Day 2001).

Numerous configurations have been proposed for tunable external cavity diode lasers. Despite this, there do not appear to be any publications where the use of silicon micromachined Fabry–Perot interferometer device has been applied. However, there are some papers introducing diode lasers that are tuned by a moving mirror or a glass plate.

In the 1970s Soviet scientists demonstrated a tunable GaAs laser by bringing a flat silver-plated mirror close (d ≈ 0.5 mm) to the chip facet. Using a piezoelectric positioner, they obtained a single longitudinal mode output with a fine-tuning range of 0.5 nm (Bogatov et al. 1973).

Cassidy's group applied a piezoelectric positioner to move a gold-plated mirror near (d = 100 … 250 μm) the laser facet. Using both external cavity length and laser temperature (- 60 … + 60 °C) adjustments, they obtained a maximum tuning range from 1,485 to 1,527 nm – that is, 42 nm (Cassidy et al. 1991). Ruprecht and Brandenburger also employed a piezoelectric positioner that moved a 150-μm thick uncoated glass plate having a 50-μm separation from the laser. Using laser temperature adjustment, they obtained a tuning range of 5 nm (Ruprecht and Brandenburger 1992).

NTT Research Laboratories used both silicon (Si) and nickel (Ni) micromachining when making a diode laser tuned by an electrostatically actuated mirror. The Ni mirror was placed very near (< 5 μm) the AR coated laser facet and a 20-nm quasi-continuous tuning range was achieved near 1,550-nm (Uenishi et al. 1996). The Si mirror-tuned laser produced a discontinuous tuning of 3 nm in the 855-nm wavelength band (Uenishi et al. 1995).

Recently, Nanyang Technological University demonstrated a miniaturised Fabry–Perot (FP) laser prototype that is tuned by a silicon micromachined mirror and has a size of $2 \cdot 1.5 \cdot 1$ mm^3. An electrostatic comb-drive moves the gold-plated flat mirror positioned at a 10-μm separation from the back facet of the laser. A butt-coupled fibre was placed at a 15-μm distance from the front facet. Using a mirror driving voltage of 10 ± 3 V, a discontinuous tuning range of 16 nm was achieved in the 1,550-nm band. The full width between half-maximum (FWHM) line width was ~ 0.1 nm and the side mode suppression ratio (SMSR) ~ 60 dB. The SM fibre-coupled power was only about 1 nW (Liu et al. 2001, Liu et al. 2002). This year the group published a modified design that employs a curved tuning mirror. The laser tunes discontinuously 13 nm by a constant step of 1.69 nm. The SMSR is better than 13 dB and the SM fibre output power about 1 mW (Zhang et al. 2004).

Table 3. Characteristics of commercial tunable VCSEL and external cavity laser modules for transmission systems.

Manufacturer	Base technology	Available wavelength range (nm)	No. of channels @ ITU spacing (GHz)	Maximum output power (mW)	Wavelength tuning speed (ms)	Modulation bit rate (Gbit/s)
Bandwidth9	VCSEL	1,530 ... 1,610	20 @ 100	≥ 1	≤ 1	2.5
Blue Sky Research	Ext. cavity	1,529 ... 1,613	81 @ 50	20	100	–[a]
Iolon	Ext. cavity	1,529 ... 1,613	81 @ 50	20	15	–[a]
New Focus	Ext. cavity	1,528 ... 1,565	81 @ 50	20	–	–[a]
Nortel	VCSEL	1,528 ... 1,604	81 @ 50	≥ 20	≤ 10	–[a]
Nortel	VCSEL	1,528 ... 1,604	81 @ 50	1 ... 2	≤ 10	10

[a] Module is used with an external modulator.

3.3 Tunable laser applications

Communications, sensing and measurement are the major application areas for tunable laser diodes (Amann and Buus 1998, p. 3). The most important characteristics required are continuous tunability, tuning range, optical power, spectral line width and frequency modulation (FM) bandwidth, Table 4.

Continuous tunability means that any wavelength within the tuning range can be accessed unambiguously and smoothly without mode hops, hysteresis or any other irregularities. While continuous tuning is desired in almost any application, it is indispensable in coherent optical detection, optical frequency-modulated continuous wave (FMCW) radar, and spectrum analysis.

The tuning range represents the most specific parameter for a tunable laser, and a wide range improves its suitability for all practical applications. Usually, constant optical power throughout the tuning range is also important. In many applications – such as coherent optical detection, optical FMCW radar, and spectrum analysis – high coherence is required and the spectral purity and line width are crucial specifications. It was realised early in the tunable laser research that wavelength tuning by carrier injection can significantly broaden the spectral line width, for example 4 MHz to 20 MHz (Amann and Schimpe 1990).

Finally, the dynamic behaviour of the tuning – such as FM bandwidth – is important in applications where tunable lasers are used as modulated light sources or where fast wavelength switching is required. This includes optical communications, optical FMCW radar (Nöding and Amann 1998), and device characterisation (Iiyama et al. 2000). We can conclude from Table 4 that coherent optical communication techniques and optical radar are perhaps the most demanding applications for tunable lasers.

Table 4. Major applications and specific performance demands of tunable laser diodes (Amann and Buus 1998, p. 4).

Performance demand	Optical communications			Sensing		Measurement		
	Wavelength division multiplexing	Coherent optical communications	Wavelength reference	Optical radar	Spectro-scopy	Fibre characteri-sation	Device characteri-sation	Optical spectrum analysis
Continuous tuning		●	●	●		●	●	●
Tuning range	●	●		●	●	●	●	●
Power		●	●	●	●	●		
Line width		●	●	●	●			●
Modulation bandwidth	●	●		●			●	

The widespread deployment of tunable lasers in optical communications depends on their ability to achieve the same performance level as their fixed wavelength counterparts. Therefore, tunable lasers must tune at least across the C-band (1,529 to 1,561 nm) and provide 10 mW of optical power if they are to perform in the trunk network applications. So far, tunable lasers in the long-haul installations have been either DFB or DBR lasers (Fuller 2001). According to the NEMI 2002 roadmap, the companies with the greatest market penetration in optical communications are Iolon and Aglity. Iolon uses a Littman-Metcalf external cavity design, Figure 12, whereas Agility employs SG-DBR lasers, Figure 10 (NEMI 2002).

Besides optical communications, tunable laser diodes are used in various measurement applications. A tunable diode laser absorption spectrometer was developed to measure very low moisture concentrations in air. This is useful, for example, in the semiconductor manufacturing industry and in atmospheric chemistry research. The device exploits the strong water vapour absorption at 1,393 nm using a commercially available DFB laser and has a sensitivity of a few parts in 10^9 by volume at atmospheric pressure. The lasing frequency was coarsely tuned up to a few hundred GHz by varying the chip temperature and fine-tuned by the injection current (Edwards et al. 2001).

Bozóki et al. also constructed a sensor system for water vapour detection using photoacoustic spectroscopy and a tunable diode laser in the Littman configuration, Figure 12. The step motor-driven micrometer screw moved the tuning mirror and the system was found to be single-mode tunable from 1,120 to 1,150 nm (Bozóki et al. 1999). Lübken et al. installed lead salt laser diodes into the rocket to measure water vapour and carbon dioxide (CO_2) in the 4.3-µm band in altitudes from 50 to 90 km and 120 km (Lübken et al. 1999).

A frequency-quadrupled external cavity diode laser applied to ultraviolet absorption spectroscopy has been used to measure the spectra of nitric oxide (NO) and sulphur dioxide (SO_2) near 215 nm (Koplow et al. 1998). UV spectroscopy has a wide range of applications in atmospheric monitoring, industrial process and emissions control, and combustion studies.

The temperature and species concentration profiles of low-pressure flames have also been measured in the infrared (IR) wavelengths using cryogenically cooled

lead salt diode lasers and monochromators (Daniel et al. 1996). Aizawa's team measured OH radical concentration in combustion environments using a 1,550 nm DFB laser tuned with the operational temperature ($- 5 \ldots + 40 °C$) and sawtoothed injection current ramp from 40 to 90 mA (Aizawa et al. 1999).

The Tokyo Gas Company developed a portable remote methane sensor based on FM spectroscopy using a 1,650 nm DFB laser whose wavelength is tuned by temperature. The operators can utilise this absorption lidar when searching for small gas leaks within a range of several meters (Iseki et al. 2000).

A chemical sensor consisting of tandem tunable DBR lasers monolithically integrated with a field combiner and photodetector has been presented. A portion of the waveguide of one laser is unclad, so that its evanescent field can sense small changes in the refractive index of the surrounding due to impurities or binding antigens. The other laser serves as the reference. Changes in the chemical concentration of the measurement point induce a shift in the heterodyne frequency (Cohen et al. 2001).

Iiyama et al. apply FMCW reflectometry to characterise long optical fibres by measuring their Rayleigh backscattering. The device is composed of a frequency swept external-cavity 1,552 nm DFB laser and a two-beam interferometer, where the fibre under test is located in the measurement arm. The laser frequency is modulated about 600 MHz by changing the position of the external cavity mirror attached to a piezoelectric transducer. A spatial resolution of 100 m was obtained when using 11-km long fibres (Iiyama et al. 2000).

Nöding and Amann also studied the frequency tuning behaviour of widely tunable (> 500 GHz) 1.5 µm DFB lasers used as a FMCW optical lidar. The frequency is swept by applying a current ramp to the tuning section of the laser. The calculations show that the nonlinear tuning characteristics have to be corrected for high-speed three-dimensional (3D) imaging applications (Nöding and Amann 1998).

Abou-Zeid and Wiese introduce a profilometer that uses a 780-nm diode laser as a wavelength tunable light source. The idea of the non-counting interferometer is to hold the phase between the measurement arm and reference arm at a constant value. This was done by tuning the laser wavelength with drive current to

compensate the changes in the measured distance. A mode-hopping-free tuning range of 0.2 nm was obtained. The authors measured distances up to 100 μm with an uncertainty of better than 10 nm (Abou-Zeid and Wiese 1998).

Tunable lasers are also useful in the interrogation of multiplexed fibre Bragg grating (FBG) sensors (Chan et al. 2001). FBGs have been studied for a variety of mechanical sensing applications, including monitoring the condition of highways, bridges, buildings and dams, smart manufacturing and nondestructive testing of composites and laminates, and remote sensing in oil wells, power cables and pipelines (Miller et al. 1998).

4. Laser-to-fibre coupling

Efficient laser-to-fibre coupling became important in the 1970s when the characteristics of the laser diodes and silica fibres were being developed to enable their use in optical communications. Simple butt coupling, where the flat (Schicketanz and Schubert 1972) or rounded (Kato 1973) fibre end is brought close to the laser facet and aligned with the emitting beam, usually satisfied the multimode fibre coupling requirements. For example, Schicketanz and Schubert obtained a coupling efficiency of 98 % by filling the gap between the laser and the 70-µm-core fibre with an index matching liquid.

Simple and efficient coupling between the laser diodes and single-mode fibres was difficult to realise. Various methods have been proposed since the beginning of the 1970s (Cohen and Schneider 1974, Weidel 1974), but it still seems that the ideal solution has not been found. This chapter first introduces the coupling theory between two Gaussian beams and then reviews some methods for the SM diode laser to SM fibre coupling.

4.1 Coupling optics

4.1.1 Coupling between two Gaussian beams

The objective of the laser-to-fibre coupling design is to optimise the power transfer efficiency and component alignment tolerances. This thesis discusses the coupling methods based on the theory of the coupling efficiency between two Gaussian beams (Joyce and DeLoach 1984). The Gaussian beam is equivalent to the lowest order transverse mode, TEM_{00}, whose flux density is ideally Gaussian over the beam cross section, Figure 13.

In practical applications the beams are typically only approximately Gaussian. However, the Gaussian approach shows the principal design trade offs and produces results that define the performance of the ideal coupling. For crude estimations the real beam can be represented by a two-point fit, for example at 1/e irradiance points.
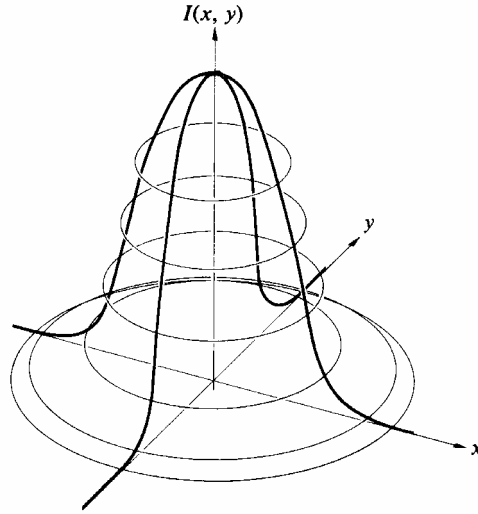
Figure 13. Gaussian irradiance distribution (Hecht 1990, p. 584).

The coupling between two Gaussian beams and the key parameters are depicted in Figure 14, which shows one projection of the three-dimensional problem. We can consider this, for instance, as a top view of the laser-to-fibre coupling, where the x-z plane is aligned with the p-n junction of the laser diode. In this thesis the first beam is referred to as the source mode and the second as the fibre mode, although this coupling schematic is also valid for other optical arrangements, such as fibre-to-fibre and optics-to-optics couplings.

The source emits a beam that has a waist diameter of $2w_{0s}$. Here, the convention is that the irradiance is $1/e^2$ of its maximum value on the edge of the beam diameter, e.g. $x = \pm w_{0s}$. This beam expands as it proceeds, so that at a distance z_s from the waist it has a diameter of $2w_s(z_s)$ and a wavefront radius $R_s(z_s)$. The equivalent parameters of the second beam are $2w_{0f}$, $2w_f(z_f)$ and $R_f(z_f)$. The parameter s equals the distance between the beam waist of the source mode and the beam waist of the fibre mode when projected on the z-axis. The fibre mode has an offset misalignment of d and an angular misalignment of θ in the alignment plane. The alignment plane is important when analysing tilt misalignments and contains the intersection of the two optical axes when d = 0.
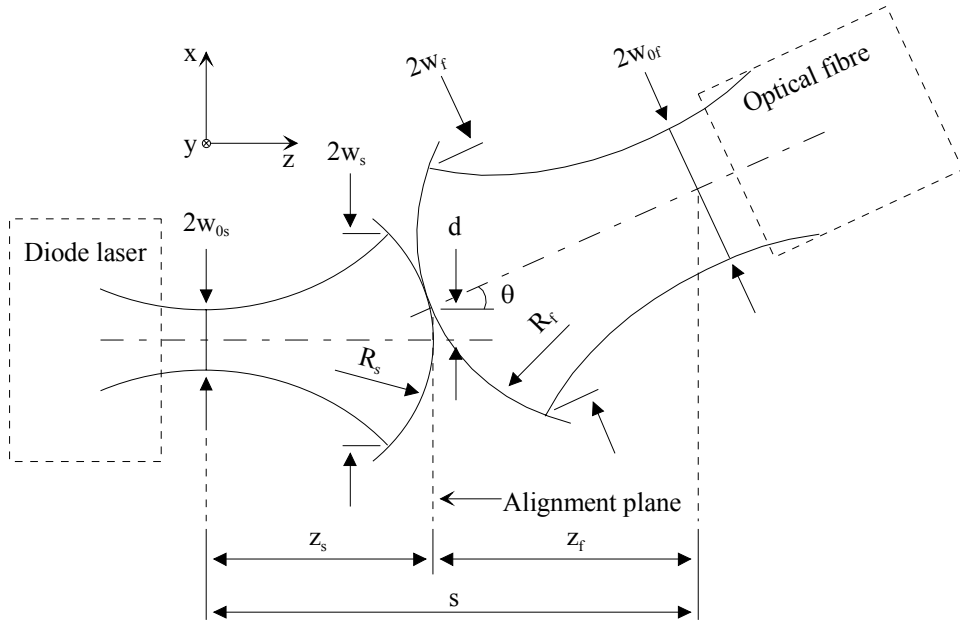
Figure 14. Schematic coupling between Gaussian beams.

The radius of the beam and the radius of the wavefront are defined as (Joyce and DeLoach 1984)

$$w(z) = w_0 \left[1 + \left(\frac{2z}{kw_0^2} \right)^2 \right]^{1/2} \tag{1}$$

$$R(z) = z \left[1 + \left(\frac{kw_0^2}{2z} \right)^2 \right] \tag{2}$$

where $k = 2\pi/\lambda$ and λ the wavelength of the radiation. The diode laser beams are often elliptical and the coupling efficiency and alignment tolerances are usually different in the x-z and y-z planes. With perfect lateral and angular alignment ($d = \theta = 0$), the coupling efficiency in the x-z plane, $\tau_{a,x}$, is (Joyce and DeLoach 1984)

53

$$\tau_{a,x} = \frac{2}{\left[\left(\dfrac{w_{0s,x}}{w_{0f,x}} + \dfrac{w_{0f,x}}{w_{0s,x}}\right)^2 + \left(\dfrac{2}{kw_{0s,x}w_{0f,x}}\right)^2 s^2\right]^{1/2}} \tag{3}$$

where the beam waists $w_{0s,x}$ and $w_{0f,x}$ are measured in the x-z plane. A similar equation defines the coupling efficiency, $\tau_{a,y}$, in the y-z plane. The total coupling efficiency, T_a, between the beams is

$$T_a = \tau_{a,x}\tau_{a,y}. \tag{4}$$

From Equations 1 and 2 we can see that if the beam waists of the source and the fibre are made equal ($w_{0s,x} = w_{0f,x}$ and $w_{0s,y} = w_{0f,y}$) and are brought together ($s = 0$), the coupling efficiency is 1 – that is, 100 %. This means that with perfect alignment it is possible, in principle, to couple all the power emitting from the source into the fibre.

Offset and tilt misalignments between the beams lower the coupling efficiency. In addition, angular misalignments can significantly reduce the speed of the automated alignment processes using the hill-climbing algorithm (Tang et al. 2001a). When the fibre mode has a lateral offset, d, in the x-z plane, the coupling efficiency, τ_x, becomes (Joyce and DeLoach 1984)

$$\tau_x(d) = \tau_{a,x}e^{-(d/d_{e,x})^2} \tag{5}$$

where

$$d_{e,x} = \frac{2^{1/2}}{\tau_{a,x}\left(\dfrac{1}{w_{0s,x}{}^2} + \dfrac{1}{w_{0f,x}{}^2}\right)^{1/2}}. \tag{6}$$

The parameter $d_{e,x}$ corresponds to the lateral misalignment that causes the coupling efficiency to decrease to 1/e ($\approx$ 37 %) from the perfectly aligned

figure. A similar equation defines the coupling efficiency, $\tau_y(d)$, where d is the lateral offset in the y-z plane.

When analysing the angular misalignment, we must first choose an alignment plane – that is, the plane by the point on the z-axis about which the rotation takes place. Typically, more than one alignment plane is of interest, as detemined, e.g., by the manipulator errors during the module assembly or the z position of the x or y axis of rotational strain of each component with respect to its mounting. In the presence of tilt in the x-z plane (Figure 14) the coupling efficiency is (Joyce and DeLoach 1984)

$$\tau_x(\theta) = \tau_{a,x} e^{-(\theta/\theta_{e,x})^2} \tag{7}$$

where

$$\theta_{e,x} = \frac{2^{3/2}}{k\tau_{a,x}\left(w_{s,x}{}^2 + w_{f,x}{}^2\right)^{1/2}}. \tag{8}$$

A similar equation defines the coupling efficiency, $\tau_y(\theta)$, where θ is the tilt in the y-z plane. We can also fit the axial dependence of the aligned coupling efficiency (s = 0) to the Gaussian form (Joyce and DeLoach 1984)

$$\tau_a(s) = \tau_a(0) e^{-(s/s_e)^2} \tag{9}$$

where

$$s_e = \frac{k\left(w_{0s}{}^2 + w_{of}{}^2\right)}{2^{1/2}}. \tag{10}$$

Equations 5, 6, 7, and 8 indicate that it is impossible to achieve a high coupling efficiency simultaneously with large offset and tilt misalignment tolerances. We can investigate this further by defining the alignment product A

$$A = \tau_a d_e \theta_e \qquad (11)$$

and find that (Joyce and DeLoach 1984)

$$0 \le A \le \frac{\lambda}{\pi}, \qquad (12)$$

or when using the normalised alignment product A_N

$$0 \le A_N = \frac{\pi A}{\lambda} \le 1. \qquad (13)$$

So, there is an upper limit for the product of the coupling efficiency, offset misalignment tolerances and angular misalignment tolerances. We can evaluate different designs by comparing their normalised alignment product both with each other and with this maximum theoretical value. When doing this it must be remembered that the Gaussian beam analysis presented above ignores many real-life phenomena, such as optical aberrations, material absorption and reflection losses. Athough A_N is a straightforward figure of merit with which to compare different coupling schemes, it is little used in practice. One reason for this is the difficulty in measuring angular tolerances without causing offset misalignments.

4.1.2 Butt coupling

Butt coupling is the simplest way of realising the optical power transfer from a diode laser into an optical fibre. The fibre is first cleaved, or cut and polished, so that its end face is a plane perpendicular to the optical axis of the fibre. The fibre end is then brought close to the laser facet and aligned with the emitting beam.

Typically, the efficiency of the butt coupling is fairly low. A standard SM telecommunication fibre has a small refractive index difference between the core and cladding, $\Delta n = n_{core} - n_{cladding} < 5 \cdot 10^{-3}$. This results in a weakly guided circular optical mode with a typical diameter of 10 μm (Corning 2002). Equation

1 (z → ∞) shows that the mode field diameter of the fibre, $2w_{0f}$, and its beam spread angle in the far field, α_f, are related

$$\alpha_f = \frac{\lambda}{\pi w_{0f}}.$$

(14)

When the fibre works as the receiver, the beam spread angle can be expected to correspond to the maximum acceptance of the incoming beam. According to Equation 14, this angle at 1,550-nm wavelength is about 6°, Figure 15.
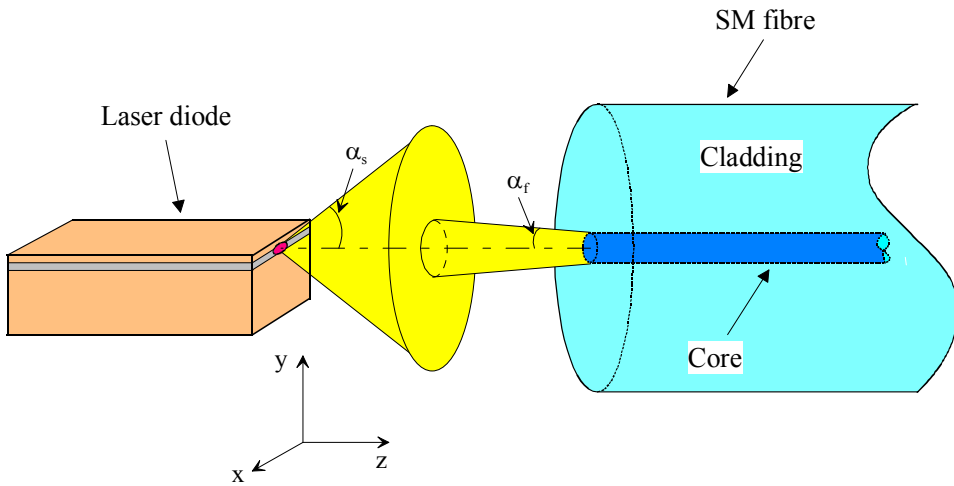

Figure 15. Butt coupling and the mismatch between the laser and fibre modes.

In the semiconductor laser waveguides Δn is generally larger than $1 \cdot 10^{-2}$ leading to a mode radius smaller than 2 μm (Moerman et al. 1997). Besides, the mode shape of the laser is highly asymmetric, causing an additional coupling loss between the laser waveguide mode and fibre mode. Typical divergence angles of the laser beam are $\alpha_{sx} = 10 \dots 30°$ and $\alpha_{sy} = 30 \dots 50°$.

In the butt coupling the maximum power transfer efficiency between the laser and SM fibre strongly depends on the divergence and ellipticity of the laser beam and, in general, is 10 to 20 %. Typical misalignment tolerances for a 1 dB extra loss are laterally $\Delta x_{1dB} = \Delta y_{1dB} = \pm 2$ μm and axially $\Delta z_{1dB} = +10$ μm (Chen and Wang 2000, Heikkinen et al. 1991, Wenke and Zhu 1983).

The efficiency of the butt coupling improves when the fibre is brought closer to the laser. However, when the external cavity formed by the laser facet and fibre end face is very short – that is, of the order of beam's Rayleigh range – the optical feedback becomes important. This may cause significant changes in the output power and wavelength (Sidorin and Howe 1997).

Because the efficiency of the simple butt coupling is poor, many alternatives have been developed to match the laser beam into the fibre mode. We can categorise them in four basic approaches:

1. Modification of the laser to increase its mode field diameter,

2. Modification of the fibre to decrease its mode field diameter,

3. Use of discrete coupling optics between the laser and fibre,

4. Combination of the above.

4.1.3 Lasers with integrated mode size converters

If butt coupling is used, the 10-dB loss between the laser and SM fibre is a significant part of the power budget in the optical network. Inserting optics between the laser and fibre can lower the loss, but this complicates the packaging structure and increases costs. Therefore, researchers have put a lot of effort into the development of lasers with monolithically integrated mode size converters to obtain a larger and more symmetric near field pattern at the device facet.

Ideally, converters match the laser mode with the fibre mode, giving a high coupling efficiency and large alignment tolerances with minimum packaging costs. Furthermore, the larger spot size near the laser facet reduces the optical power density, so that the catastrophic optical damage power level becomes higher, which means that the maximum output power and operating life time increases.

The mode size converters can be classified between lateral, vertical, combined and special taper designs. In the laterally tapered devices, Figure 16, the width of the guiding layers is changed, whereas in the vertically tapered chip the

thickness of the guiding layers changes along the device. In contrast to lateral tapers, where standard processing techniques can be used for the definition of the taper, special growth and etching techniques are required when fabricating vertical tapers. In a combined taper both the lateral and vertical dimensions of the guiding layers are changed (Moerman et al. 1997).
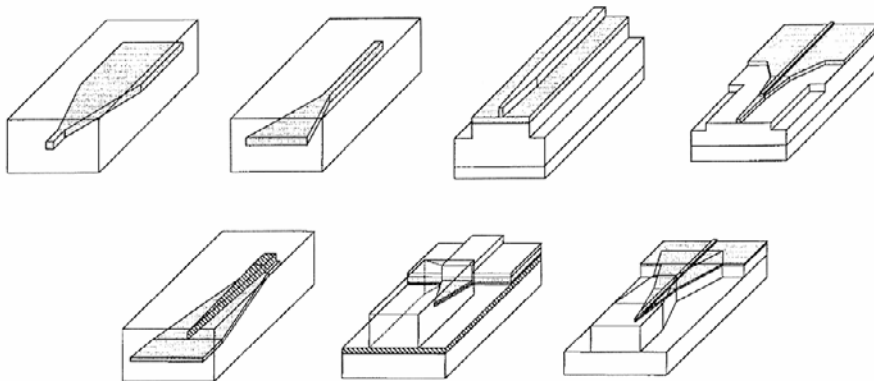
Figure 16. Lateral taper designs (Moerman et al. 1997).

Coupling losses of 3 dB ($\eta \approx 50$ %) between 1,550 nm laser diodes with integrated spot size converters and cleaved SM fibres can be easily obtained, and the best reported efficiencies lie around 80 % (Hübner et al. 1997, Vawter et al. 1997, Yan et al. 2002, Zengerle et al. 1995). Hübner's team achieved a coupling efficiency of 75 % and a lateral tolerance of ± 2 µm for a 1-dB additional loss. Usually there is a trade off between the reduction of the coupling loss and increase of the lasing threshold. For example, Galarza's group increased the coupling efficiency from 14 % to 55 % at the expense of the threshold current rise from 30 to 50 mA (Galarza et al. 2002).

Although laser diodes with integrated spot size converters would be the ideal source for fibre optic teleommunications, and their reported performance is excellent, they have not evolved into commercial standard components. Possibly, their fabrication requires so complex material growth and high precision control in lithography and etching processes that the production yield and component reliability is too low to enable their widespread use (Wongcharoen et al. 2001).

Fu et al. tried to reduce the fast axis divergence of the laser beam by integrating a cylindrical microlens on the output facet, Figure 17. The lens was directly fabricated on the emitting surface by focused ion beam SiO_2 deposition. When the focal length of the lens was 32 μm, the full angle divergence of the 635 nm laser reduced from 31 to 2.1°, and its coupling efficiency into the 10-μm core fibre increased from 42 to 80 % (Fu et al. 2000).
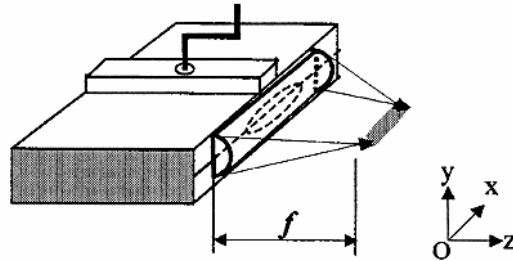

Figure 17. Cylindrical microlens integrated on the laser facet (Fu et al. 2000).

4.1.4 Tapered fibres

Fibre tapering reduces the mode mismatch between the laser diode and SM fibre. When the fibre core gets thinner, its mode field diameter decreases. Tapered fibres are attractive because they combine the simplicity of butt coupling with a reasonable coupling efficiency, reduced optical feedback into the laser, simplicity of fabrication, good mechanical stability and ease of packaging, Figure 18. The challenges in tapering are to transform the fundamental fibre mode without excess losses due to coupling to higher order modes and to make the process reproducible and suitable for mass production. Several different methods have been applied, including drawing in the small flame (Birks et al. 1990) or electric arc (Marshall 1986), chemical etching (Alder et al. 2000, Ghafouri-Shiraz and Aruga 1996), and mechanically grinding and polishing (Shiraishi et al. 1997).

Marshall made drawn tapers by melting the surface of the fibre in the fusion splicer arc, pulling one end and stretching the fibre to breaking point. The fibre tip was then melted in the arc until the surface tension formed a spherical end surface (Marshall 1986).

Alder et al. used wet chemical etching by immersing the Ge-doped fibres in hydrofluoric (HF) acid. Since the HF dilution evaporates at a constant rate during the process, the fibre length exposed to the acid decreases linearly with the etching time and a linear taper is formed. Using a 40 % dilution of HF at room temperature, the etching rate for the cladding was 15 nm/s and for the core 29 nm/s. The produced mode field diameters ranged between 10.6 μm and 0.8 μm and the average transformation loss was 0.13 dB (Alder et al. 2000).
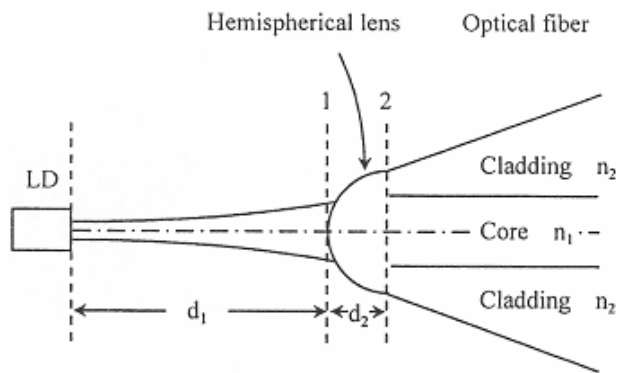

Figure 18. Coupling with a tapered and lensed fibre (An 2000).

Hunziker's group made elliptically lensed polarisation-maintaining (PM) fibres by first etching the taper and then melting the fibre tip with an arc discharge splicer. They claim that melting rounds and smooths the fibre surface, leading to a much better Gaussian mode shape than the etching alone. They measured a coupling loss of 2.6 dB (55 %) when using a 1,300 nm laser and PM fibre (Hunziker et al. 1992). In a similar set-up Presby and Edwards obtained an average efficiency of 71 % when they employed an aspherical lens fabricated by a pulsed CO_2 laser (Presby and Edwards 1992b).

A theoretical investigation of the coupling characteristics of the drawn and etched tapers found that drawn tapers give higher efficiency. When the drawn and lensed taper gave a coupling efficiency of 80 %, the etched version with the same geometric parameters produced only 53 %. The reason behind this is that only the cladding becomes thinner for an etched taper, whereas drawing tapers also the core, Figure 19. The tapered core leads to a mode with a curved wavefront, which matches better with the diverging Gaussian mode of the laser.

Drawn tapers are also less sensitive to the radius of the lens made on the taper tip, which eases the fabrication process (An 2000).
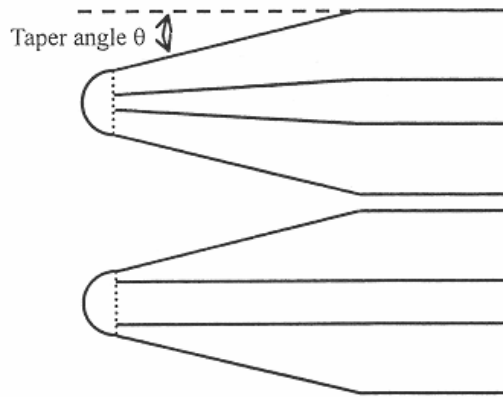

Figure 19. Tapered core and tapered cladding fibres (An 2000).

4.1.5 Fibre microlenses

One popular method for the laser-to-fibre coupling is to use fibre microlenses, whereby a specific optical surface is made on the end face without tapering the fibre. Microlenses are attractive because they combine the simplicity of butt coupling with a permanently aligned lens element and high coupling efficiency. Several lens geometries have been studied, including hemispherical, cylindrical, hyperbolic and wedge-shaped. Microlenses have been manufactured by various methods, such as etching (Eisenstein and Vitello 1982, Weidel 1974), laser micromachining (Presby and Edwards 1992a, Presby and Giles 1993), microjet printhead technology (Cox et al. 1996) and photolithography (Bachelot et al. 2001, Cohen and Schneider 1974, Saitoh et al. 2000).

Bachelot's team placed a drop of a photosensitive liquid at the end of the cleaved fibre and exposed it with an argon laser, Figure 20. After curing, the illuminated area of the formulation was polymerised and the unreacted liquid washed out with methanol. The authors varied the height and curvature of the lens by changing the height of the drop and the exposure time. The smallest radius of curvature produced was 0.6 μm (Bachelot et al. 2001). Saitoh et al. made convex glass microlenses by evaporating an As_2S_3 film onto the flat fibre

end and exposing it with a HeNe laser from the opposite end of the fibre. The unexposed film was etched in a NaOH solution (Saitoh et al. 2000).
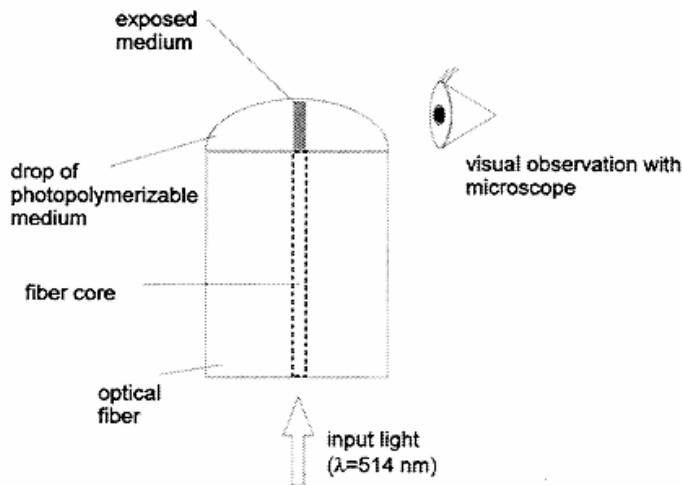

Figure 20. Exposing a polymer microlens on the fibre tip (Bachelot et al. 2001).

The working distances are very short in conventional lensed fibres having a hemispherical end radius of 5 to 15 μm. However, the coupling scheme should have a sufficiently long working distance so that no contact occurs between the laser and fibre during the assembly process, and to reduce the unstability of the laser due to the backward reflected light from the lensed fibre end face.

Chanclou et al. studied the coupling between a laser array and fibre ribbon by using a combination of graded index (GI) fibre acting as the lens and coreless silica fibre acting as the spacer. The GI fibre ribbon was first spliced to the silica fibre ribbon, which was then cut and spliced to the SM fibres. Finally the GI fibres were cut at the proper distance. The process is promising for the production of low-cost multichannel modules. The authors obtained an average coupling loss of 4.5 dB $\pm$ 0.04 dB at a working distance of 48 μm for the four-fibre ribbon. The measured misalignment tolerances were $\Delta x_{1dB} = \Delta y_{1dB} = \pm 1$ μm and $\Delta z_{1dB} = \pm 9$ μm (Chanclou et al. 1998). Shiraishi's group used a variation of the scheme when employing the GI fibre as a spacer and the coreless silica fibre with a hemispherical end face as the lens (Shiraishi et al. 1997).

Shiraishi and Kuroo propose a cascaded GI fibre (GIF) scheme that combines high coupling efficiency and moderate working distance, Figure 21. The first GIF collects the emitted laser light with a high numerical aperture (NA) and collimates the beam that is focused into the fibre by the second GIF. The hemispherical end face was made either by using an arc discharge fibre splicer or by mechanically grinding and polishing. The authors obtained a minimum coupling loss of 1.8 dB at the 40-µm working distance. The misalignment tolerances were $\Delta x_{1dB} = \pm 0.5$ µm and $\Delta y_{1dB} = \pm 0.5$ µm (Shiraishi and Kuroo 2000).
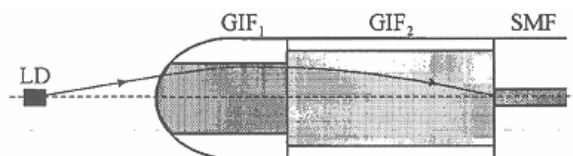

Figure 21. Coupling with cascaded GI fibres (Shiraishi and Kuroo 2000).

Chen and Wang extended the working distance by integrating a lensed fibre with a long period fibre grating, Figure 22. The hemispherical lens couples the laser beam mainly into the fibre cladding. The grating diffracts this beam into different orders and a certain part of the power will be coupled to propagate in the core. The grating was made by using UV exposure through an amplitude mask, and the lens by an arc discharge fibre splicer. A maximum coupling efficiency of 35 % at the working distance of 110 µm and misalignment tolerances of $\Delta x_{1dB} = \Delta y_{1dB} = \pm 2.6$ µm and $\Delta z_{1dB} = \pm 26$ µm were obtained (Chen and Wang 2000).
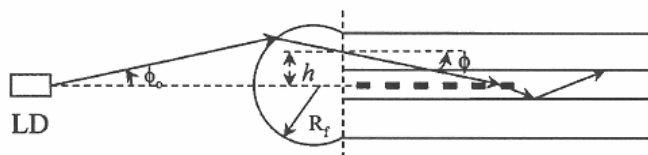

Figure 22. Coupling with a lensed fibre and grating (Chen and Wang 2000).

When the laser beam is highly elliptic, efficient coupling requires some means to convert the beam to the round shape. This can be accomplished by using an

anamorphic element that has different refractive powers in the two orthogonal directions (Smith 2000, p. 287).

Presby and Giles demonstrated the fabrication of asymmetric hyperbolic microlenses on the fibre end face using a pulsed CO_2 laser. The fibre rotated in a precision capillary tube that was held by an xyz manipulator, and the laser beam was turned on and off at the appropriate times to produce the required lens shape. The fabrication time was less than one minute. When using a 980-nm laser having an ellipticity of 3, the authors obtained a coupling efficiency of 84 % (Presby and Giles 1993). The coupling efficiency of the ideally shaped hyperbolic lens is only limited by the reflection losses and can, therefore, be over 95 % (Edwards et al. 1993, Vassallo and van der Keur 1992).

Shah et al. used a wedge-shaped fibre tip when coupling a 980-nm laser into a dispersion-shifted fibre. The end face was fabricated with a wedge-shaped polishing tool. They obtained a coupling efficiency of 47 % at the working distance of 6 μm. The misalignment tolerances were $\Delta x_{1dB} = \pm 1.8$ μm and $\Delta y_{1dB} = \pm 0.2$ μm. The authors also tried to enlarge the y-axis tolerance by uptapering the end section of the fibre in a fusion splicer, and then cleaving and wedge-shaping the uptapered portion. When the maximum outer diameter was 300 μm and the taper length 600 μm, Δy_{1dB} increased to ± 0.35 μm and the axial tolerance Δz_{1dB} was ± 5 μm (Shah et al. 1990).

Tang et al. theoretically analysed the coupling between the laser and wedge-shaped fibre end face. They found that in addition to the tight y-axis offset tolerance, the pitch angular tilt ($\Delta\theta_x$) is critical. Their calculations for a 980 nm laser resulted in a maximum coupling efficiency of 72 % with misalignment tolerances of $\Delta y_{1dB} = \pm 0.3$ μm, $\Delta\theta_{x\_1dB} = \pm 2.5°$, and $\Delta\theta_{y\_1dB} = \pm 4.2°$ (Tang et al. 2001b). If we combine the lateral offset tolerances measured by Shah et al. with the angular tolerances calculated by Tang et al., we can calculate that the normalised alignment product A_N is 0.32.

Modavis and Webb investigated a double wedge shape design consisting of two slope angles, Figure 23. Since the scheme only involves flat surfaces, it can be fabricated by standard grinding techniques. The optimum working distance using a 980 nm laser was 4 μm, the average coupling efficiency 78 %, and the

lateral misalignment tolerances $\Delta x_{1dB} = \pm\ 1.2\ \mu m$ and $\Delta y_{1dB} = \pm\ 0.3\ \mu m$ (Modavis and Webb 1995).

Yoda and Shiraishi propose a modification to the wedge-shaped fibre tip where a quarter-pitch long piece of the gradient index fibre is spliced to a standard SM fibre. The wedge-shaped end face converts the cylindrical laser wavefront to a plane, which the GI fibre stub then focuses into the SM fibre. The authors claim that this scheme is especially advantageous when using highly elliptic 980 nm pump lasers. The lowest simulated coupling loss was 0.22 dB ($\eta = 95$ %). The experimental case had a calculated loss of 2.2 dB, whereas the measured loss at a working distance of 55 μm was 5.2 dB. The authors believe that the difference was mainly caused by manufacturing errors in the fibre tip process (Yoda and Shiraishi 2001).
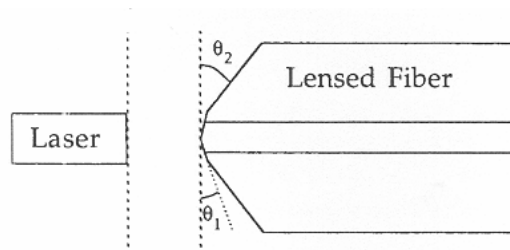

Figure 23. Coupling with a double wedge fibre tip (Modavis and Webb 1995).

4.1.6 Discrete lens coupling

There is an extensive variety of discrete lens coupling schemes, including single plano-convex, ball, aspheric or graded index (GRIN) lens configurations and combinations of two or more lens elements. A few examples of these designs are presented here.

The ball lens is one of the simplest and most economical discrete microlenses to fabricate and mount. However, because the divergence of the laser beam is usually fairly large, spherical aberration significantly reduces the coupling efficiency of the single ball lens system, Figure 24.

The coupling loss can be minimised by using a small diameter lens made from a high refractive index material and having high-quality anti-reflection coatings (Karstensen 1988). The measured coupling efficiencies obtained with a single ball lens vary between 30 and 56 % and the typical working distance is 50 μm (Ratowsky et al. 1997, Sumida and Takemoto 1982, Wilson 1998).
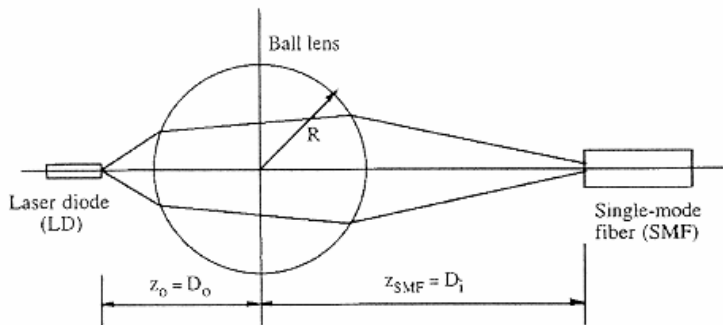

Figure 24. Coupling with a ball lens (Wilson 1998).

The use of diffractive optical elements (DOE) has also been studied, Figure 25. The integrated diffractive-refractive lens can be thinner and lighter than its traditionally implemented equivalent, and have a higher numerical aperture. DOEs can be fabricated using focused ion beam milling (Yong-Qi et al. 2000).
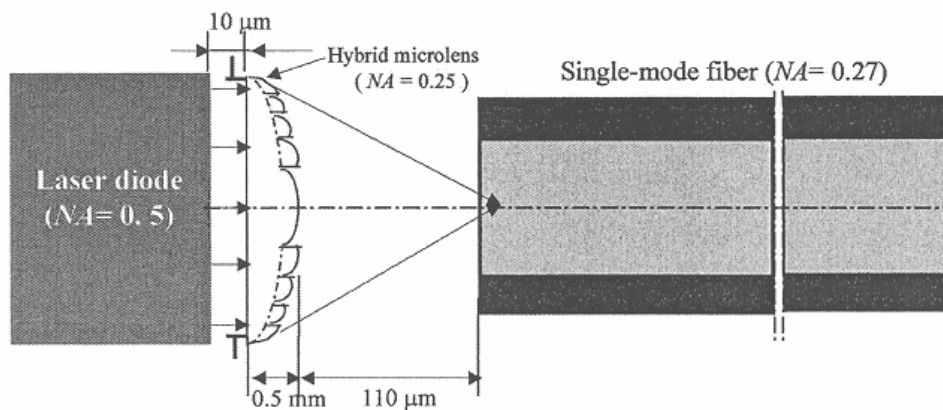

Figure 25. Coupling with a hybrid diffractive-refractive microlens (Yong-qi and Bryan 2001).

Ogura et al. used a graded-index oval-core (GIO) fibre to match the field profiles of laser diode and SM fibre, Figure 26. Here the elliptic output of the 980-nm laser is enlarged and focused on the end face of the GIO fibre by a lens system consisting of an aspheric and spheric element. The minimum coupling loss was 0.6 dB, and the lateral misalignment tolerances $\Delta x_{1dB} = \pm 12$ μm and $\Delta y_{1dB} = \pm 3$ μm (Ogura et al. 2001). The tolerance of the GIO fibre length for an additional 1 dB loss was ± 44 μm. From the reported misalignment tolerances we can calculate that the normalised alignment product A_N is 0.94.
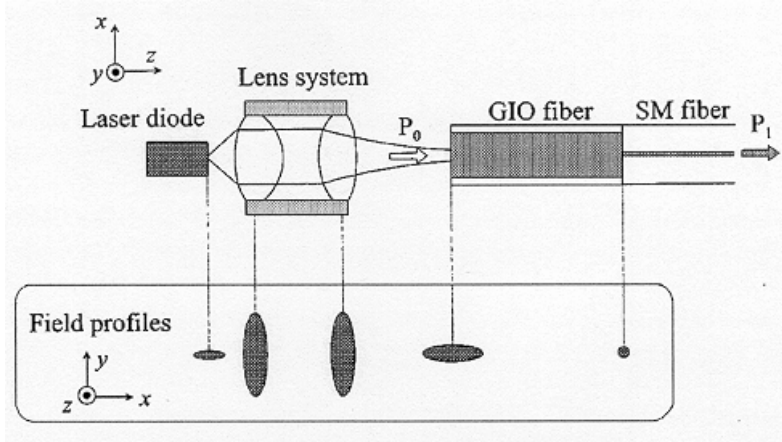

Figure 26. Coupling with a lens pair and GIO fibre (Ogura et al. 2001).

4.1.7 Comparison of coupling alternatives

Examples of the performance of various coupling options are shown in Table 5, where the alignment tolerances are given for the fibre movement. Fibre tapers and fibre microlenses have many desirable features, such as compactness, reasonable coupling efficiency, good mechanical stability, and ease of packaging. However, they also have disadvantages, namely short working distance, tight transverse alignment tolerances and critical fabrication process of the microlens. For example, hyperbolic microlenses must have submicron precision in order to fully realise the coupling enhancement. Microlenses are not compatible with the use of optical isolators.

When surveying commercially available fibre tapers and microlenses it was found that there are very few standard products, and their prices are high. For example, the unit price in 10-piece lots varied from 80 to 180 EUR and in 1000-piece lots they cost from 50 to 120 EUR. For comparison, the butt coupling fibre pigtail that has an FC connector on the other end costs 7 EUR in the 1000-piece lot.

Discrete lens coupling offers flexibility to the optical design by allowing a trade off between lateral misalignment tolerances and angular tolerances. Lens couplings also allow the use of optical isolators. Small high-performance lenses can be expensive, especially in small quantities. For example, the unit price of 10 aspheric glass lenses that we planned to use in our prototypes was 80 EUR.

Usually, the goal in the laser-to-fibre coupling is to maximise the efficiency and obtain as loose alignment tolerances as possible. However, this can lead to a solution that is susceptible to optical feedback from the fibre into the laser. External optical feedback can change the lasing threshold, output power and spectral line width, increase the intensity and phase noise, generate additional cavity modes, and produce mode hopping. The phenomena occuring in semiconductor lasers due to optical feedback are a complex and extensively studied subject (Henry and Kazarinov 1986, Kallimani and O'Mahony 1998, Marciante et al. 1997, Petermann 1995) and are not further explored in this thesis.

Using an optical isolator can eliminate optical feedback, but this raises costs and complicates the alignment procedure. One proposal to reduce the optical power feedback and increase the carrier-to-noise ratio (CNR) is to position the lensed fibre offset from the optical axis (Mondal and Shi 2001). Although the fibre misalignment lowers the coupling efficiency, this is more than compensated by the decrease in the intensity noise of the laser. Mondal and Shi calculate that a lateral shift of 0.7 μm decreases the coupling efficiency by 2 dB, but improves the CNR by 10 dB.

Table 5. Comparison of various coupling alternatives between SM laser diode and SM optical fibre.

Coupling method	Coupling efficiency (%)	Wave-length (nm)	Working distance (μm)	1 dB excess loss tolerance			Reference
				x (μm)	y (μm)	z (μm)	
Butt coupling	16	1,550	12	± 2	± 2	+ 10	Chen and Wang 2000
	21	830	10	± 1.1	± 0.9	+ 8.7	Wenke and Zhu 1983
Drawn taper	59	1,318	25	–	–	± 5	Li and Freude 1991
	66	830	30 ... 50	± 0.7	± 0.4	± 6.6	Wenke and Zhu 1983
Etched taper	63	830	5 ... 10	± 0.6	± 0.4	± 4	Wenke and Zhu 1983
	66	822	–	± 0.6	± 0.4	6.5	Ghafouri-Shiraz and Aruga 1996
Ground & polished taper	56	1,300	15	± 1.6	± 1.3	± 12	Shiraishi et al. 1997
GI fibre lens	35	1,300	48	± 1	± 1	± 9	Chanclou et al. 1998
Coreless fibre lens	43	1,300	100	± 2.3	± 2.2	± 24	Shiraishi et al. 1997
	56	1,300	150	± 0.75	± 0.65	± 5.6	Bludau and Rossberg 1985
Hyperbolic fibre lens	85	1,550	40	± 0.9	± 0.9	± 4	Kalonji and Semo 1994
	90	1,300	–	–	–	–	Presby and Edwards 1992a

Table 5. Comparison of various coupling alternatives ... continues.

Coupling method	Coupling efficiency (%)	Wave-length (nm)	Working distance (μm)	1 dB excess loss tolerance			Reference
				x (μm)	y (μm)	z (μm)	
Cascaded GI fibres	66	1,300	40	± 0.5	± 0.5	–	Shiraishi and Kuroo 2000
Lensed fibre + grating	35	1,560	110	± 2.6	± 2.6	± 26	Chen and Wang 2000
Wedge	47 80	980 980	6 10	± 1.8 –	± 0.2 –	– + 12	Shah et al. 1990 Annovazzi-Lodi et al. 1997
Double wedge	78	980	4	± 1.2	± 0.3	–	Modavis and Webb 1995
Ball lens	29 48	1,310 1,300	400 60	± 2.1 –	± 2.1 –	± 50 –	Heikkinen et al. 1991 Ratowsky et al. 1997
Aspheric glass lens	60	1,300	1,500	–	–	–	Kato and Nishi 1990
Two GRIN lenses	40	1,300	–	± 6	± 6	± 400	Kawano et al. 1989
Lens + GIO fibre	87	980	–	± 12	± 3	± 190	Ogura et al. 2001

4.2 Principles of fibre attachment

4.2.1 Packaging design aspects

Reliable, reproducible and high-yield packaging techniques are essential for meeting the cost and performance objectives of optoelectronic components. Until recently, they have mainly been assembled manually, which leads to poor productivity, low yield and high manufacturing costs (Pate 2001). Therefore, one objective for packaging designs is to apply production automation, with conventional pick and place equipment to load all the components and a reflow process to attach them in one step (Yang et al. 2002).

Several optical, mechanical, thermal and electrical factors complicate the packaging design of fibre coupled laser modules (Mickelson et al. 1997, p. 60).

- The threshold current, slope efficiency and emitting wavelength of the laser chip are temperature sensitive.

- Lasers generate heat, which can cause an excessive temperature rise in the active region due to the relatively poor thermal conductivity of compound semiconductors. For example, at T = 25 °C, k_{InP} = 67 W/mK, k_{GaAs} = 44 W/mK, whereas k_{Si} = 150 W/mK, k_{Cu} = 398 W/mK, and $k_{diamond}$ = 2,000 W/mK.

- The devices are quite sensitive to stress-induced degradation, so low-stress die attachment techniques must be used.

- The alignment tolerances of the critical optical components are small, typically below 1 μm.

- The parasitic capacitances, inductances and resistances of the package can severly constrain the frequency response of high-speed lasers.

The major challenge in SM fibre packaging is to position the optoelectronic chips and optical components with high accuracy in 3D space. This can be performed using either active or passive alignment. Active alignment applies iterative movements of the components while monitoring the output to acquire precise positioning. While this produces fine performance, it takes a long time,

72

needs expensive equipment and makes it difficult to automate the production (Kim et al. 2002).

Passive assembly of the module, which means that all components are assembled without electronically activating the dies and measuring the light output, decreases the number of assembly steps and reduces the manufacturing complexity. The passive alignment can be obtained by using fiducial marks that are photolithographically placed on the aligned components (Cohen et al. 1991, Shuke et al. 1999), or by making a micro-machined silicon or glass substrate (Aoki et al. 1999, Armiento et al. 1991, Boudreau et al. 1998, and Breedis 2001).

The self-alignment of the component is based on the surface tension of the molten solder (Sasaki et al. 2001) or the liquid adhesive (Kim et al. 2002). Several authors have used soldering to obtain passive alignment of lasers at the tolerance of less than ± 1 µm (Boudreau et al. 1998, Dautartas et al. 2002, and Sasaki et al. 2001). Since it is necessary to heat the attached devices above the melting point of the solder, heat sensitive components cannot be used. Furthermore, there can be problems when flux is used, such as reduction in chip reliability and optical efficiency due to flux residues (Kim et al. 2002).

When using passive alignment, butt coupling is typically used between the laser and the SM fibre. This limits the coupling efficiency to 5 ... 15 % (Armiento et al. 1991, Breedis 2001, and Cohen et al. 1991). Coupling loss can be decreased by using spot size converted lasers (Sasaki et al. 2001) or by filling the gap between the laser and the fibre with an index matching liquid (Shuke et al. 1999). Aoki et al. achieved a coupling efficiency of over 50 % when using a planar microlens array between the four-channel laser and the SM fibre array (Aoki et al. 1999).

Passive assembly with self-alignment requires components that have accurate dimensions and registration marks, and the manufacturing process must be delicately controlled. This is compatible with the mass production of low-cost devices. However, when assembling module prototypes or low-volume components, it is usually rational to use standard off-the-shelf components. Their tolerances – such as the dimensions of the chips or the focal length of the lenses – are not tight enough to enable passive assembly. Therefore, we must use

active assembly and arrange sufficient clearance for the final component attachment.

In the laser-to-fibre assembly we must activate the source, so that it is natural to first attach and electrically contact the laser chip and then assemble either the optics or the fibre. Typically, it is unnecessary to fasten the lens with submicron inaccuracy, because a minor lens misalignment can be compensated when positioning the fibre.

In the following discussion it is assumed that the final and most critical assembly step is the fibre attachment. The most commonly used methods are laser welding, soldering and adhesive bonding, and the discussion concentrates on them. Other techniques – such as electroplating (Pat. US 5,048,919 1991, Pat. US 5,311,610 1994) – have been introduced, but their industrial utilisation has remained marginal.

4.2.2 Laser welding

Nd:YAG laser welding has been used for joining metal and sealing lids in hermetic microelectronics packages for decades. It has become the most popular option for the fibre attachment because of the submicron accuracy, bonding strength, cleanliness, speed and long-term reliability of the joint. Laser welding requires metal housings, which increases component costs, and the laser beam must have direct access to the weld, which limits the packaging design flexibility (Shannon and Palen 2002).

The pulsed Nd:YAG laser is used in single shot mode and the welding is done simultaneously with two or three spots. The pulse energy, duration, shape and diameter can be tailored according to the needs of each attachment configuration. Typical welding pulse energy is 1 to 4 J and duration 2 to 5 ms, producing weld spots of 400 to 600 μm in diameter (Shannon and Palen 2002).

Laser weldable materials include kovar (NiFeCo alloy), nickel alloys, invar (FeNi alloy) and 304 stainless steel. For thermal expansion concerns, similar materials are usually welded, but some dissimilar materials – such as kovar and stainless steel – can also be joined together. The material composition needs to

be selective to minimise the carbon, sulphur, and phosphorus content, and highly reflective materials – such as copper – should be avoided. In addition, the thickness of the gold plating needs to be limited to about 1 to 2 μm in order to avoid crack formation in the seam area (Kuang et al. 1999, Shannon and Palen 2002).

The tip of the fibre is encapsulated in a cylindrical metal ferrule that provides the housing necessary for rigidity and welding, Figure 27. Usually, the clip is first welded to the metallic platform and then to the fibre ferrule. The rapid solidification of the welded parts and the associated material shrinkage leads to a relative movement between the pre-aligned components, which can significantly reduce the coupling efficiency and lower the packaging yield. The welding-induced misalignment is influenced by various factors, such as the intensity, irradiance balance (Kuang et al. 2001) and angle of the incident laser beams, welding positions, joint geometry, and welding point sequence (Lin et al. 2002b). The welding clip is usually fabricated to be mechanically soft, without any mechanical memory or residual spring component, to enable post-weld positioning correction (Shannon and Palen 2002).
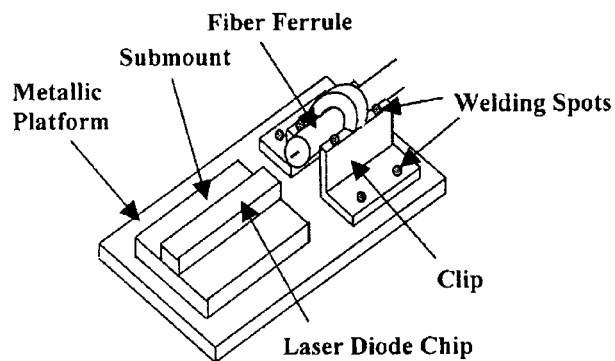
Figure 27. Laser and fibre subassembly in laser welding (Lin et al. 2002b).

NTT used Nd:YAG laser welding when attaching the SM fibre in the coaxial 1,300 nm laser module. An average assembly loss of 0.24 dB was obtained, which translated into a fibre displacement of ± 1.2 μm (Kato and Nishi 1990).

The fibre soldered into a metal ferrule can shift after the welding process due to temperature changes. Cheng et al. studied this phenomenon and discovered that hard solders performed better than soft solders. Cheng's team used an SM fibre soldered into the invar ferrule with an inner diameter of 400 μm and measured the transverse fibre shift after 500 temperature cycles from − 40 to + 85 °C. The fibre moved 1.5 to 1.9 μm when attached with a Pb37Sn63 solder having a melting point of 183 °C and 0.5 to 1 μm with a Au80Sn20 solder having a melting point of 280 °C (Cheng et al. 2001). When applying the most misalignment sensitive coupling schemes, a lateral fibre shift of 1 μm causes an excess loss of several dBs, Table 5.

Shaw et al. used glass solder when attaching a PM fibre inside the kovar ferrule. This approach has the advantage that non-metallised fibres can be used, which decreases the stress on the fibre inside the ferrule, and also slightly improves the decoupling of the stress from the package and decreases the heat conducted along the fibre to the welding platform (Shaw et al. 2001).

4.2.3 Soldering

Soldering is well-understood process for die bonding in electronics. It can be realised by electrical resistance heating (Datta et al. 2003, Datta and Dagenais 2003, Enochs 1987, Kondo 1991, Witham et al. 2000) as in Figure 28, contact heating or laser-assisted reflow. However, the use of soldering in fibre attachment can be problematic because the magnitude, direction and long-term stability of the shrinkage is difficult to predict and control (Kim et al. 2002, Powell 2000). Solder material creep, solder-to-fibre or solder-to-substrate delamination and solder joint fractures can also lead to optical misalignment and cause component failures (Rassaian and Beranek 1999). Furthermore, the use of flux can reduce chip reliability and optical coupling efficiency due to residues (Nangalia et al. 1997). Possibly due to these reasons, the number of publications describing soldering in SM fibre attachment is much lower than the volume of papers dealing with laser welding.

Enochs applied a planar structure, in which both the laser and conically lensed fibre were mounted on the same ceramic substrate with a high-temperature solder (Au80Sn20). Temperature cycling between − 60 ... + 70 °C produced an

output power variation of 0.2 dB, which corresponded to a calculated maximum lateral misalignment of $\pm\,0.25\mu m$ (Enochs 1989).
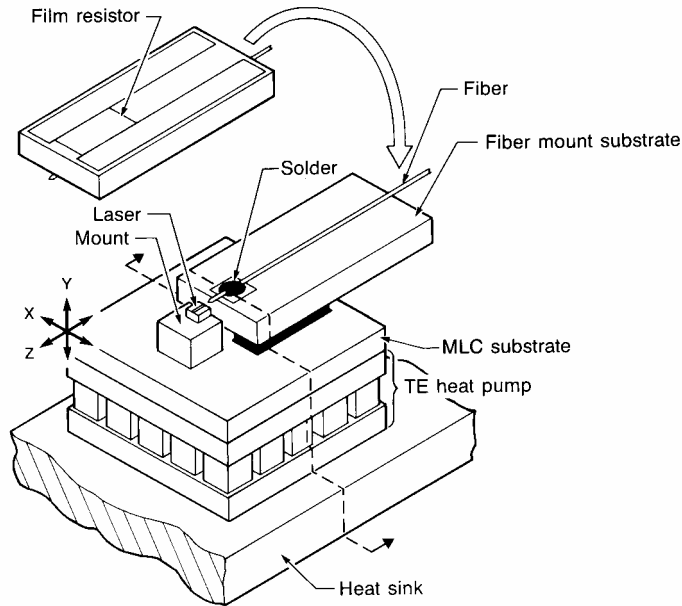

Figure 28. Fibre attachment by resistor heated soldering (Enochs 1987).

Datta et al. empolyed thin-film heaters and a combination of passive and active alignment when attaching conically lensed SM fibres. First, the metallised fibre was soldered (eutectic AuSn, T = 280 °C) inside the v-groove of the silicon holder. Then the holder was placed on the silicon optical board (SiOB) containing a solder preform (eutectic InSn, T = 117 °C), a thin-film heater and a laser chip. The coarse alignment was obtained using passive assembly. Heating and refreezing the solder with the heater and adjusting the position of the fibre carried out the final horizontal and vertical alignment. The measured coupling efficiency varied between 40 and 50 % (Datta et al. 2003). Datta and Dagenais tested soldering (eutectic AuSn, T = 280 °C) of bare metallised fibres and noticed that the average horizontal and vertical shift of the fibre was 1.36 mm and 0.78 µm respectively (Datta and Dagenais 2003).

Flanagan et al. used laser assisted solder reflow when attaching metallised fibres with a maximum lateral misalignment of $\pm\,0.2\,\mu m$. Over 60 % of the

attachments succeeded within the first reflow and the total yield using up to 10 reflows was 98 %. The authors claim that in volume production, that is, more than 3,700 pieces per year, laser soldering has lower cost than laser welding by enabling the use of smaller form-factor packages, by eliminating the fibre ferrule and welding clip, shortening the cycle time and increasing the yield (Flanagan et al. 2003).

Witham et al. measured the alignment shift when soldering metallised fibre to the alumina (Al_2O_3) substrate. When the fibre was positioned 89 μm above the substrate and cantilevered 1.5 mm from the fibre clamp, the vertical and horizontal alignment shifts were -4 μm and ± 2 μm. The reproducibility of the results was ± 1 μm (Witham et al. 2000).

4.2.4 Adhesive bonding

Adhesive bonding can combine dissimilar materials, fill gaps in uneven surfaces, and is an economic process with low equipment investment. The most important drawback is the component displacement induced during the adhesive curing process. It is also difficult to repeatedly dispense minute volumes. The curing UV or IR energy must be introduced to the bond selectively without distorting the assembly, and the adhesive support is poor both before and during the cure. There can also be residual volatile components escaping from the adhesive after the curing is complete.

Although adhesive bonding seems to have potential for the attachment of MM fibres (Matthews et al. 1990, Pat. US 4,329,190 1982, Pat. WO 02052324 2002), only a few publications describing its use in the assembly of SM laser modules could be found, and just one paper applied adhesives in the attachment of the actively aligned fibre. Selecting the right adhesive is important when minimising the component misalignment during curing. The adhesive should have low shrinkage and small Young's modulus (Lin et al. 2002c, Murata 1998). The geometry of the joint, the thickness and non-uniformity of the bonding layer, and the thermal expansion coefficients of the adhesive and attached parts also influence the mounting accuracy.

Sunaga's team pigtailed a TO-can packaged laser using active alignment and UV-curable adhesives, Figure 29. The fibre retainer, which had a precisely formed capillary, and the sleeve were made from transparent polymer by injection moulding. Axial alignment was done between the sleeve and the TO-can, and lateral alignment between the sleeve and the fibre retainer. The air holes let the UV-curable resin get into the capillary and the gap (Sunaga et al. 2000).
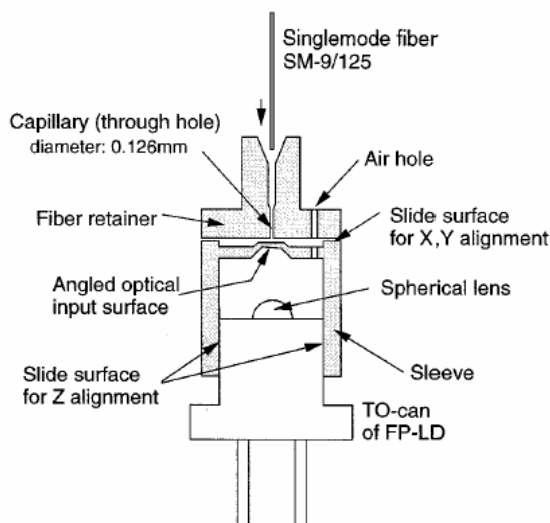

Figure 29. Fibre attachment using UV-cured adhesives (Sunaga et al. 2000).

Lin et al. used finite element analysis in their study of the relative misalignments between the fibres and lenses in the fibre array collimator assembled using UV-curable adhesives. Their results claim that the significance of the curing shrinkage ratio of the adhesive is negligible. When the ratio increased from 4 to 6 %, the misalignment of the fibre tip rose from 0.763 to 0.781 μm. However, the maximum compression and tension stress of the joint increased along with the shrinkage ratio. The thickness of the adhesive layer was 150 μm. When the elastic modulus of the adhesive was altered from 500 to 3,000 MPa, the fibre tip misalignment increased from 0.56 to 1.04 μm (Lin et al. 2002c).

Murata reports the development of the UV-curable precision adhesive that has a very low shrinkage of 1.2 % and thermal expansion coefficient of $20 \cdot 10^{-6}$ 1/K. He claims that by using this adhesive, the ball lens movement caused by the UV

curing can be reduced below 1 µm (Murata et al. 1996, Murata 1998). NTT's team has earlier reported the development of a UV epoxy having a shrinkage of 2 % and thermal expansion coefficient of $20 \cdot 10^{-6}$ 1/K. They used this adhesive when attaching a ball lens in front of a laser diode and obtained an inaccuracy of around 1 µm (Suzuki et al. 1990).

5. Module design and realisation

5.1 Functional design

The functional model of the tunable laser prototypes is shown in Figure 30. The diode laser emitting at the 1,550-nm band serves as the light source and the wavelength tuning FPI is placed close to the AR coated laser facet. Monitoring electronics measure the optical power and mean wavelength of the beam transmitted through the FPI and use this information to tune the operation voltage of the FPI and drive current of the laser. Operation point control electronics drive a piezoelectric transducer that adjusts the separation between the laser and the FPI.

The coupling optics transfer the radiation emitted from the high reflection (HR) coated laser facet into the SM fibre. Temperature stabilisation electronics measure the laser temperature with a thermistor and adjust it using a thermoelectric cooler (TEC). The module housing acts as the packaging platform and protects the internal components from adverse environmental effects.
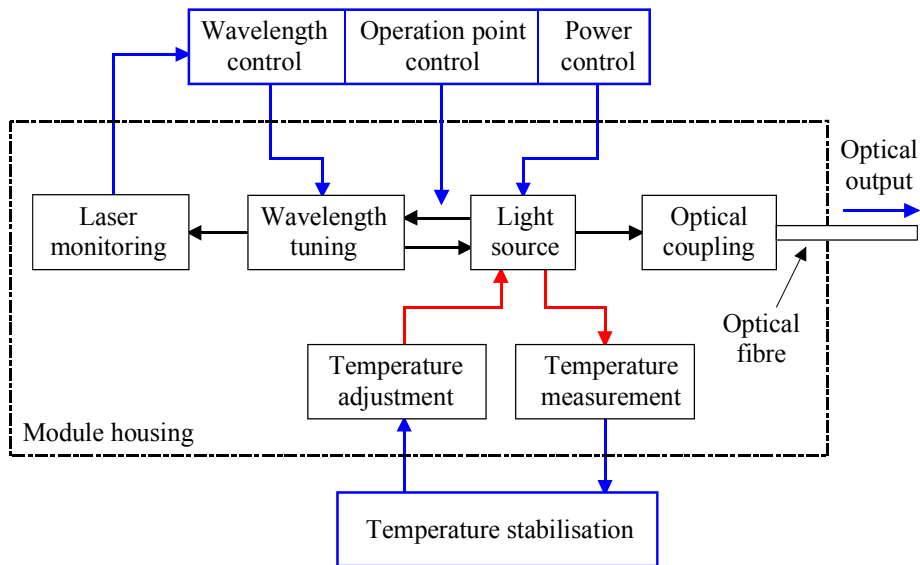

Figure 30. Functional model of the tunable laser prototypes.

5.2 Modelling of the tuning characteristics

5.2.1 ESEC laser model

The ESEC laser model comprises a laser diode (LD) and a tunable Fabry–Perot interferometer, Figure 31. LD has a length of L, diameter of the beam waist $2w_0$, and end facet reflectances R_1 and R_2. The laser chips were manufactured at the Ioffe Institute in St. Petersburg, Russia, and their inner structure is discussed in (Golikova et al. 2000). The FPI consists of a movable and stationary mirror having reflectances of R_3 and R_4, and etalon length l. The FPI's movable mirror stands at the distance d from the laser facet. P denotes the optical power, λ_0 the nominal laser wavelength, and λ the principal tuned wavelength – that is, the wavelength of the strongest longitudinal mode. The parameter values used in the calculations are shown in Table 6.
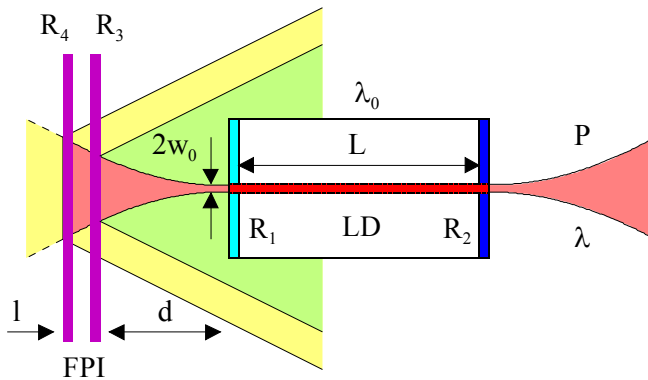
Figure 31. Schematic of the tunable laser modelling.

Table 6. Parameter values used in the ESEC laser modelling.

LD	FPI	Beam
$R_1 = 0.15$	$R_3 = R_4 = 0.97$	$w_{0,x} = 2.5\ \mu m$
$R_2 = 0.50$	$d = 19.88\ \mu m$	$w_{0,y} = 0.6\ \mu m$
$L = 700\ \mu m$	$l = 2.2 \ldots 2.4\ \mu m$	$\lambda_0 = 1{,}550\ nm$

5.2.2 Fabry–Perot interferometer

The silicon micromachined Fabry–Perot interferometer chips were fabricated at the VTT Microelectronics Centre in Espoo, Finland, and their characteristics were based on the patent (Pat. US 5,561,523 1996). The FPI chips had electrical contact pads in the corners and a clear aperture in the centre. The thickness of the chips was 500 μm, and other dimensions were as shown in Figure 32. The FPIs were designed to have an air space of 2.34 μm in the rest position, but the fabricated value was about 2.6 μm.
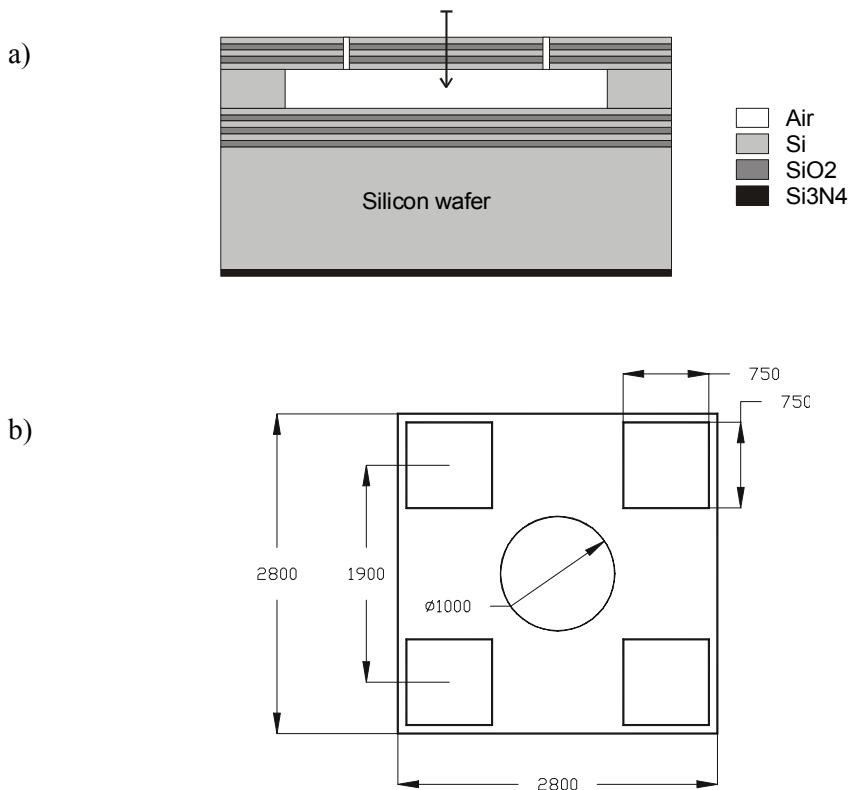
Figure 32. Schematic structure of the FPI chip. a) Cross section and b) dimensions in micrometers (courtesy of VTT Microelectronics Centre).

The Fabry–Perot interferometer makes use of multiple reflections between two closely spaced partially transmitting surfaces. We can study its operation by

83

assuming that it consists of two parallel plane mirrors with reflectances of $R_3 = R_4$ separated by an air space of l (Svelto 1998, pp. 140–145). If a plane wave enters the FPI, the output beam leaving the interferometer consists of a superposition of the beam resulting from a single pass through the two mirrors with the beams arising from all multiple reflections. Thus, the electric field amplitude of the output beam is obtained by adding the amplitudes of all these beams, taking into account their corresponding phase shifts.

The transmittance of the FPI consisting of lossless mirrors, T_{FPI}, is given by (Svelto 1998, p. 142)

$$T_{FPI} = \frac{|E_t|^2}{|E_i|^2} = \frac{(1-R_3)(1-R_4)}{\left[1-(R_3 R_4)^{1/2}\right]^2 + 4(R_3 R_4)^{1/2}\sin^2\phi} \tag{15}$$

where E_t is the electric field amplitude of the output beam, E_i the electric field amplitude of the input beam and 2ϕ the phase difference between successive multiple reflections. The reflectance of the lossless FPI is then, $R_{FPI} = 1 - T_{FPI}$. The phase difference can be calculated using (Svelto 1998, p. 141)

$$\phi = \frac{2\pi n l \cos\theta}{\lambda} \tag{16}$$

where n is the refractive index between the mirrors, θ the angle between the propagation vector of the plane wave inside the etalon and the normal of the FPI mirrors and λ the wavelength of the plane wave.

According to Equation 15, the transmission maxima occur when $\sin^2\phi = 0$. This takes place when $\phi = m\pi$, where m is a positive integer called the order of interference. Figure 33 shows the calculated (MathSoft Mathcad 2001) transmittance of the lossless FPI having $R_3 = R_4 = 0.97$ and $l = 2.6\ \mu m$. We see that this symmetric device has several maxima with a transmittance of 1. When the FPI operates in the converging or diverging beam, the transmittance is lower and the passband wider and shifted to shorter wavelengths than what is shown in Figure 33. The real FPIs used in this thesis were designed to operate in the third interference order in the wavelengths around 1.55 μm.
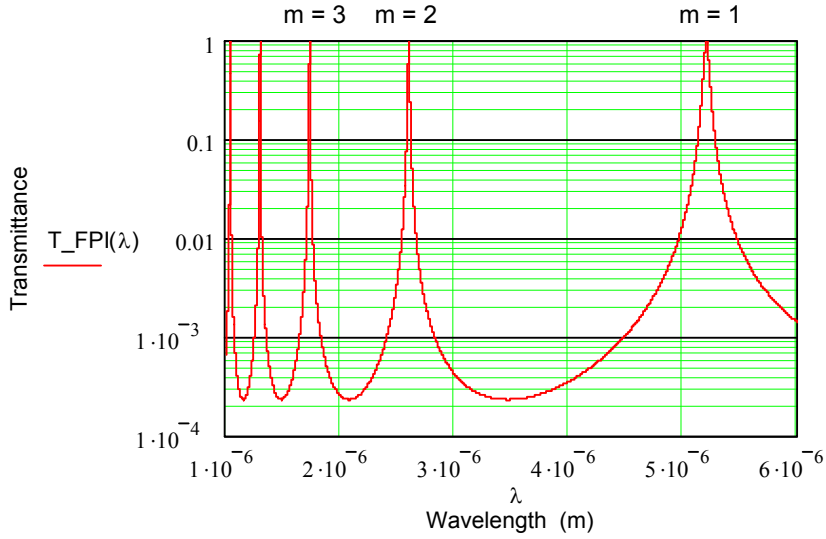
Figure 33. Calculated transmittance of the symmetric and lossless FPI that has l = 2.6 μm.

By applying voltage to the real FPI device, the top mirror is moved toward the fixed one and the spectral transmission band is tuned to shorter wavelengths. The distance between the mirrors is a nonlinear function of the control voltage (Sidorin et al. 1999b)

$$l(U) = \frac{l_0}{3}\left\{1 + 2\cos\left[\frac{1}{3}\arccos\left(1 - \alpha U^2\right)\right]\right\}$$ (17)

where U is the voltage across the FPI mirrors, l_0 the distance between the mirrors at zero voltage and α the parameter that relates to the spring constant of the FPI structure, area of the mirrors and l_0.

Figure 34 shows an example of the calculated distance between the mirrors as a function of the control voltage. Here, the third order transmittance maximum is set to 1,550 nm when U_{FPI} is 34 V. We see that the voltage-controlled movement of the top mirror increases at high voltages. The minimum separation between the mirrors is limited by the singular point in the derivative of Equation 17 when dl(U)/dU → −∞. Here, l(45 V) is 1.733 μm, which corresponds to a transmittance maximum of 1,155 nm. In practice this also seems to be the

critical point where the movable mirror sticks to the fixed mirror permanently and the FPI device becomes useless.
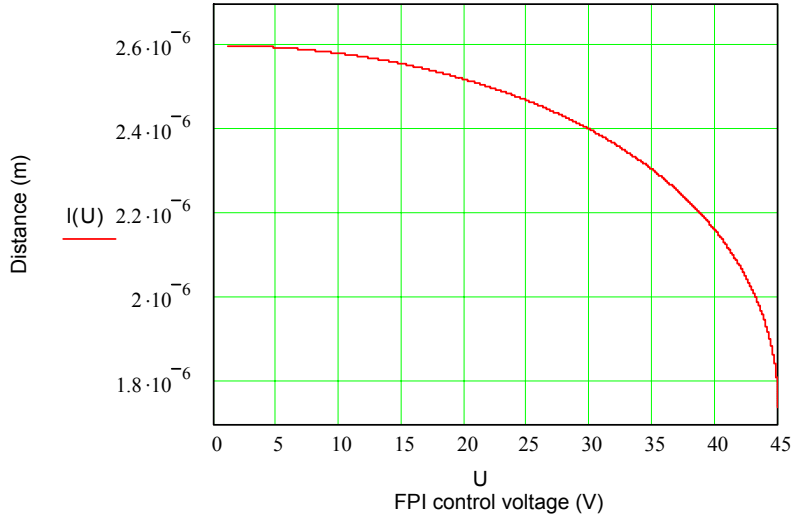

Figure 34. Calculated distance between the FPI mirrors.

The mirrors of the real FPI device consist of quarter-wave polysilicon and silicon dioxide layers as shown in Figure 32. Because the refractive index difference between silicon, $n_{Si}(1{,}550\text{ nm}) \approx 3.5$, and silicon dioxide, $n_{SiO_2}(1{,}550\text{ nm}) \approx 1.44$, is large, high reflectances can be obtained using relatively few layers. For the tunable laser modelling, the mirror reflectance was determined by first measuring the spectral transmittance of the FPI device in the nearly collimated beam. Then the measured data as shown in Figure 35 was fitted to the theoretical graph of an air-spaced Fabry–Perot etalon using thin film design software (Thin Film Center Essential Macleod). The absorption of the device was assumed to be zero.
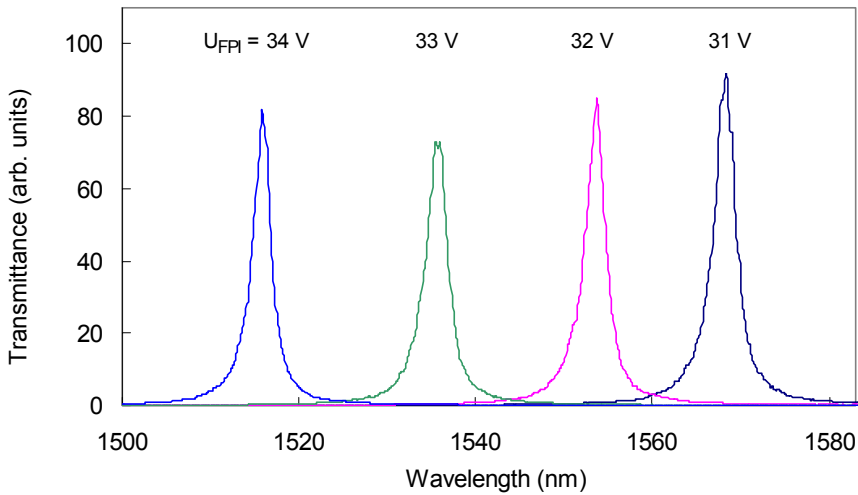
Figure 35. Example of the FPI transmittance measured using a low-NA beam.

The silicon nitride layer that has a quarter-wave optical thickness at the bottom of the FPI device acts as an anti-reflection coating and also decreases the unwanted interference effects caused by the silicon substrate etalon. The layer material that produces a zero reflectance has a refractive index, n_{AR}, (Smith 2000, p. 203) of

$$n_{AR} = \sqrt{n_{air} n_{Si}}$$

(18)

where n_{air} is the refractive index of air, $n_{air} \approx 1$ and n_{Si} is the refractive index of the silicon substrate. When $n_{Si}(1,550 \text{ nm}) \approx 3.5$, the optimal AR coating material has $n_{AR} \approx 1.87$.

5.2.3 Laser tuning simulations

The performance of the ESEC laser was predicted with a phenomenological laser model. Here, R_1 is replaced with an effective reflectance R_{eff} that describes the properties of the external cavity. As a complex number, R_{eff} takes into account the amplitudes of the multiple reflections and also carries information about their phases. In the laser tuning simulations (MathWorks Matlab 6.1) the micromachined FPI was replaced by two parallel plane mirrors that had a

reflectance of 0.97 and were separated by a variable air space of l. The details of the modelling theory are explained in (Aikio and Karioja 1999, Aikio et al. 1999, Aikio et al. 2002 and Aikio 2004).

The simulations showed that the performance of the laser could be adjusted by modifying the ESEC parameters and that a large tuning range is a compromise with the high output power. For example, enlarging the reflectance R_3 or decreasing R_1 increases the amount of light that is reflected from the FPI and coupled into the LD. This strengthens the interference effects at the laser facet and broadens the wavelength tuning range. However, a smaller R_1 transfers more light from the laser into the ESEC, which decreases the output power P. This can be partly compensated by decreasing R_2, but it must be large enough for the laser to operate. Decreasing d also boosts the interference at the laser facet and widens the tuning range.

The simulations indicated that the FPI could be used to tune the laser spectrum linearly or nonlinearly. When the laser operates near the FPI's resonance region, the phase of the light reflected from the FPI changes rapidly. This causes nonlinear wavelength tuning and variation in the output power, Figure 36. When the drive current of the laser is 70 mA, the calculated wavelength tuning range is 9 nm and the average output power 3.4 mW. The rapid discontinuous tuning only occurs at the discrete regions of distance d. These regions are 50 to 100 nm wide and can be found in $\lambda/2$ intervals.
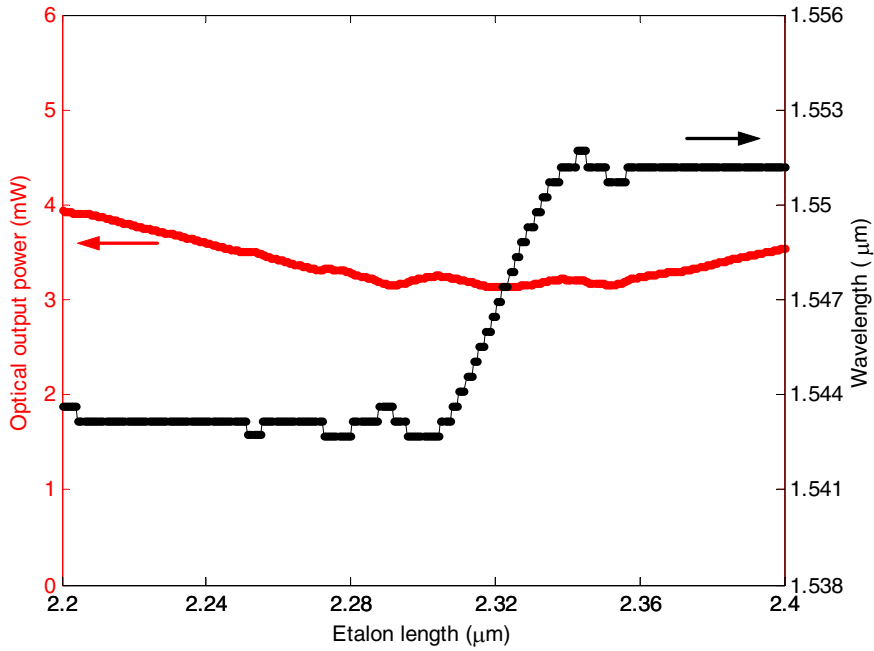
Figure 36. Simulated principal wavelength and power in nonlinear tuning.

The FPI can also be used as a movable mirror that changes the length of the external cavity. Then, the wavelength shift is linear and requires a larger movement of the top mirror than in the nonlinear tuning, Figure 37. All parameters used in these calculations are the same as in Table 6, except that l now varies from 2.3 to 3.1 μm. In practice the air space between the micromachined FPI mirrors cannot be larger than 2.6 μm, as is shown in Figure 34. The tuning range remains the same as in the nonlinear tuning, but output power is higher. When the laser current is 70 mA, the calculated average output power is 4.4 mW. The minimum output power occurs when the laser operates near the FPI's resonance region.
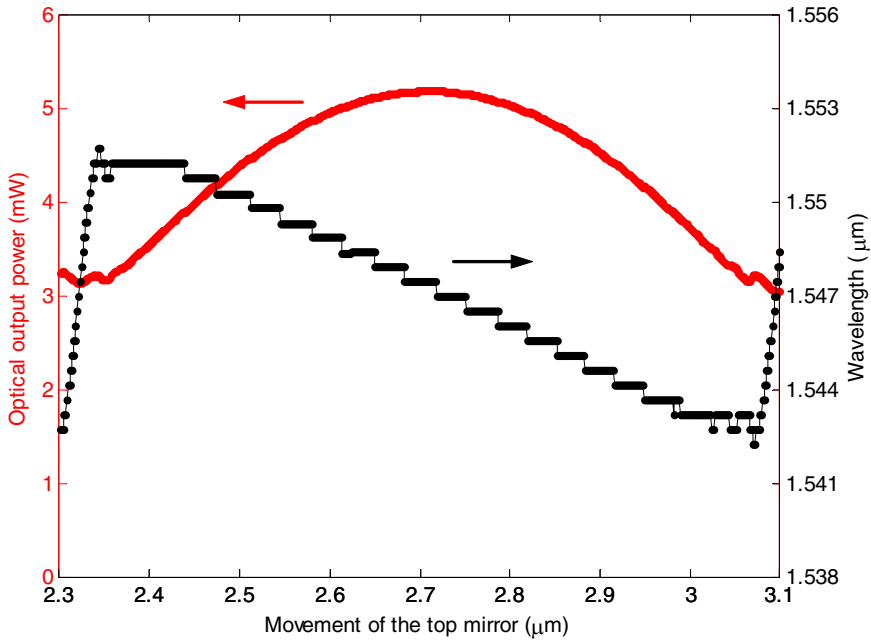
Figure 37. Simulated principal wavelength and optical power in linear tuning.

5.3 Laser-to-fibre coupling optics

5.3.1 Optical modelling of the laser and fibre

The main characteristics of the laser diodes were measured before starting to model the laser-to-fibre coupling optics. This included measuring the optical power as a function of drive current (PI curve), the beam divergence angles, and the emission spectrum. The PI curve is required when calculating the measured coupling efficiency. The divergence angles define the dimensions of the source, and the laser spectrum the dominating wavelength for the optical simulations. The spectrum of the free-running laser is also a useful reference when analysing how the tuning affects the laser characteristics. The measured laser diodes were divided into three groups based on their end facet reflectances, Table 7.

Table 7. End facet reflectances of the laser diodes.

Group	R_1	R_2
I	0.10	> 0.95
II	0.05 … 0.08	0.70
III	0.15	0.50

The PI curve was measured with the optical power meter (Ando AQ-1135E) and the large area detector (AQ-2711, $\varnothing$ = 5 mm) that was brought close to the emitting surface. The laser driver (ILX Lightwave LDC-3722) controlled the laser's drive current and temperature. The measured PI curves of the HR coated facet of the laser III-A are shown in Figure 38.
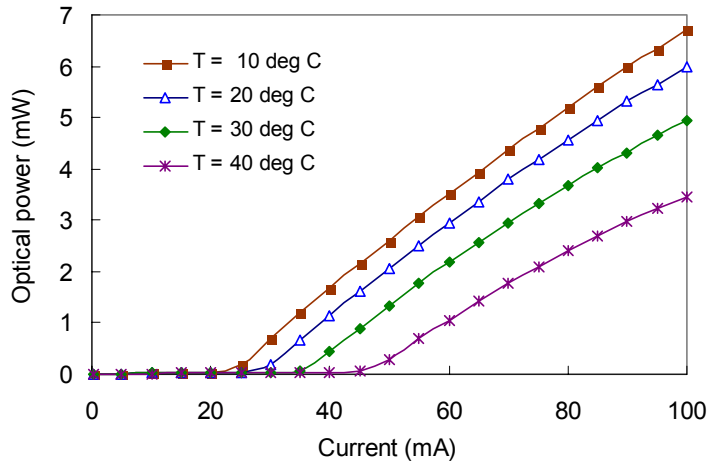
Figure 38. Measured HR facet PI characteristics of the laser III-A.

Both the threshold current and the slope efficiency of the laser depend on the temperature. The PI curves also exhibit bending caused by the heating of the active region (Golikova et al. 2000). All the laser chips used in the measurements were soldered (In50Pb50) active side up to the aluminium nitride (AlN) substrate.

In the divergence angle measurements the lasers lay on the rotation stage driven by a micrometer screw. The optical power meter (Ando AQ-2140 with AQ-2743 sensor) was set behind a 1-mm wide slit and positioned at a distance of 300 mm from the laser. The orthogonal direction was measured by turning the lasers through 90°.

The measured intensity distributions were fairly consistent with the Gaussian approximation in the x-z plane, Figure 39a. Typically, α_{sx} was 7° ± 0.5°, corresponding to a mean beam waist, $w_{0s,x}$, of 4.0 μm. In the y-z plane the conformity with the Gaussian was slightly poorer, and there were small ripples with an amplitude of ± 2 to ± 10 % of the maximum value, Figure 39b. The laser manufacturer believes that these ripples originate from some inhomogeneities in the waveguide and cladding layers. The typical α_{sy} was 40° ± 5°, corresponding to a mean $w_{0s,y}$ of 0.7 μm. Laser radiation was linearly polarised in the x-z plane with an intensity ratio greater than 100.
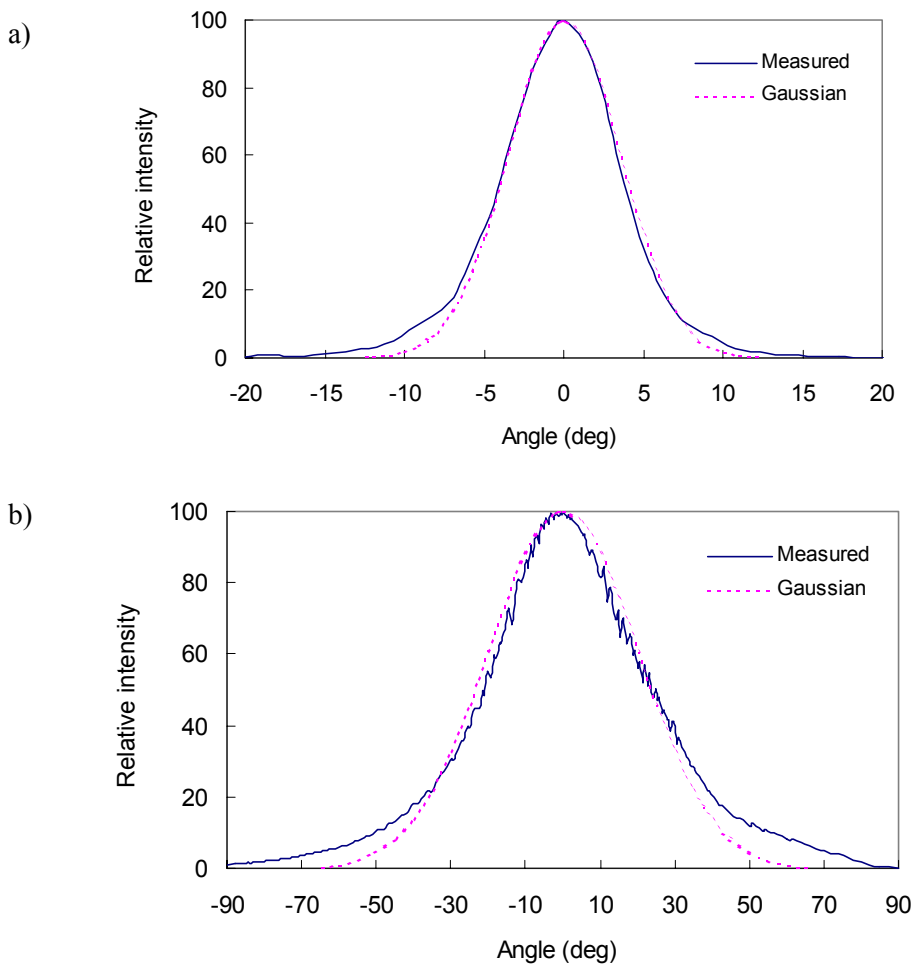
*Figure 39. Measured AR facet intensity distributions of the laser II-1. a) In x-z plane, b) In y-z plane.*

In the spectrum measurements part of the laser emission was coupled via an SM fibre to the optical spectrum analyser (Ando AQ-6315B). The analyser attained a resolution of 0.05 nm. The measured laser spectrum had a temperature coefficient of 0.6 nm/K, Figure 40. The typical mean wavelength at 25 °C was 1,535 nm and the spectral width (FWHM) varied between 1 and 2 nm.
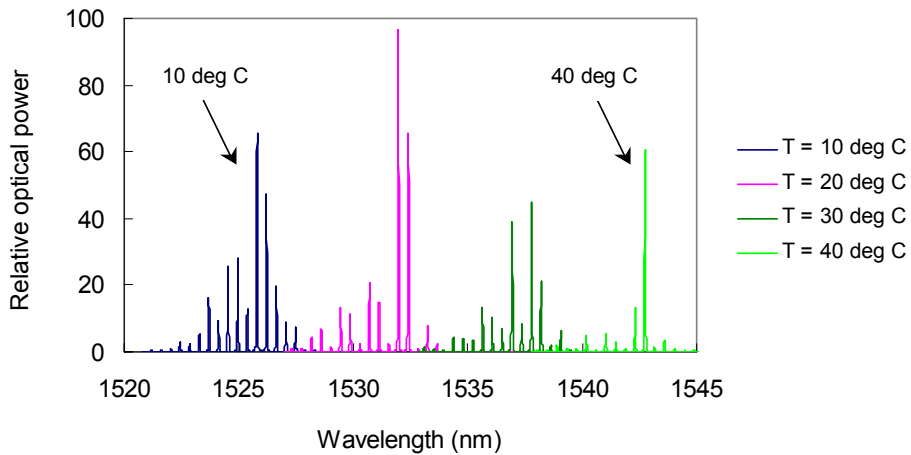

Figure 40. Measured spectrum of the laser II-1 when I_{LD} was 90 mA.

In the fibre characterisation laser light was coupled into the 2-m long SM fibre pigtail (Corning SMF-28) and its output end placed on the rotation stage. The measured intensity distributions corresponding to a w_{0f} of 5.2 µm matched nicely with the Gaussian approximation in both the x-z and y-z planes, Figure 41. The main parameters based on the measurements and used in the coupling simulations are shown in Table 8.
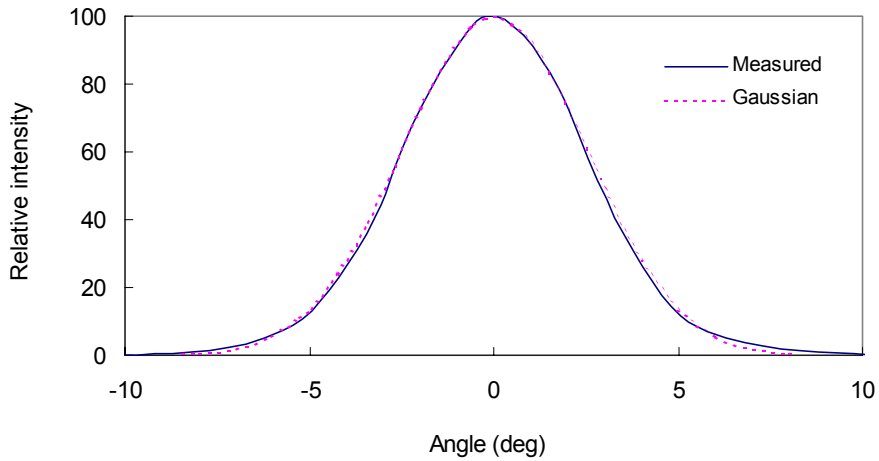
Figure 41. Measured intensity distribution of the SM fibre.

Table 8. Basic parameters for the laser-to-fibre coupling simulations.

Parameter	Symbol	Value
Operating wavelength	λ	1,535 nm
Spectral width	$\Delta\lambda$	2 nm
Beam waist radius of the laser	$w_{0s,x}$	4.0 μm
	$w_{0s,y}$	0.7 μm
Beam waist radius of the fibre	w_{0f}	5.2 μm

5.3.2 Butt coupling simulations

The performance of the laser-to-fibre coupling alternatives was simulated with the physical optics propagation feature of the Zemax® program that models the optical system by propagating wavefronts (Zemax 2003, p. 447). First, the butt coupling was studied to verify that simulations give accurate results by comparing them with values obtained using the Gaussian beam analysis described in Chapter 4.1.1.

It was assumed that the laser and fibre modes were monochromatic Gaussian beams and had the beam waists listed in Table 8. The simulations took into account the Fresnel reflection from the entrance fibre end (ca. 3.3 %). The simulated coupling efficiency and the results from the Gaussian theory are shown in Figure 42.

The simulated values are in fair agreement with the Gaussian theory. However, there is a minor deviation starting at the 5.74-µm working distance, where the simulated efficiency suddenly increases by 0.5 %. At this point Zemax changes its propagating operator (Zemax 2003, p. 448), which causes the discontinuation. The butt coupling is insensitive to wavelength tuning – e.g., at the 20-µm working distance a $\pm$ 10-nm shift in λ changes the coupling efficiency $\mp$ 0.05 %. The maximum coupling efficiency at $s = 0$ is 25 %.
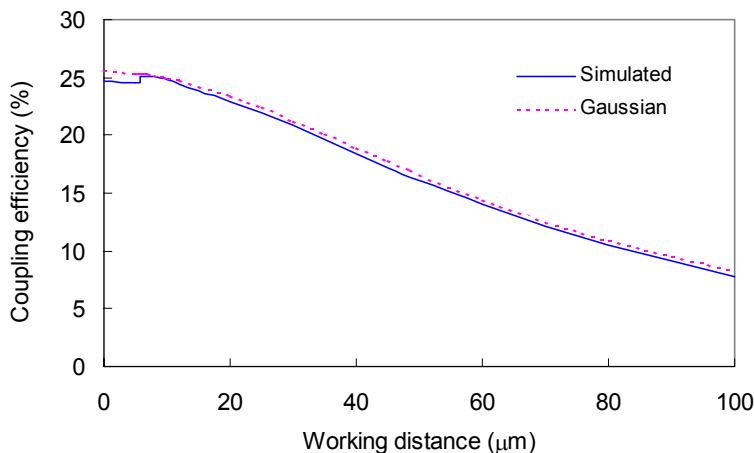
*Figure 42. Axial misalignment tolerance in the butt coupling.*

The lateral misalignment tolerances for the fibre end at the 20-µm working distance are shown in Figure 43. The error between the simulated values and the Gaussian theory is below 1 % when $|\Delta x| <$ 5 µm and $|\Delta y| <$ 10 µm. The excess loss tolerances are $\Delta x_{1dB}(20\mu m) = \pm$ 2.3 µm and $\Delta y_{1dB}(20\mu m) = \pm$ 1.9 µm.
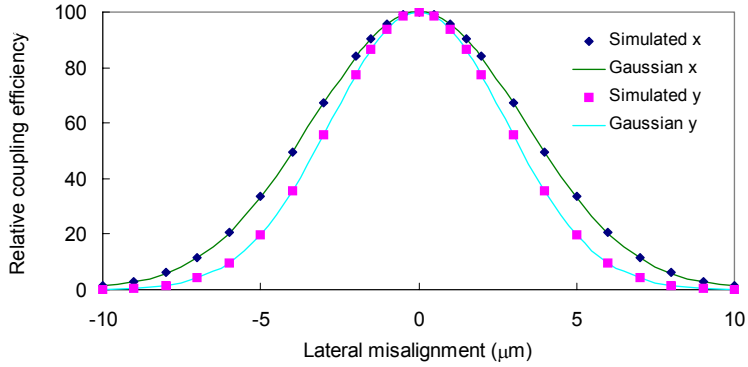
*Figure 43. Lateral misalignment tolerances in the butt coupling at s = 20 µm.*

The angular misalignment tolerances for the fibre end at the 20-µm working distance are shown in Figure 44. The error between the simulated values and the Gaussian theory remains below 1 % when $|\Delta\theta_x| <$ 7° and $|\Delta\theta_y| <$ 9°. The excess loss tolerances are $\Delta\theta_{x\_1dB}(20\mu m) = \pm$ 2.9° and $\Delta\theta_{y\_1dB}(20\mu m) = \pm$ 5.1°. When the distance between the laser and the fibre is zero, the normalised alignment product $A_N = 1$. When s increases, A_N decreases – for instance, $A_N (s = 20 \text{ µm}) = 0.36$ and $A_N (s = 100 \text{ µm}) = 0.04$.
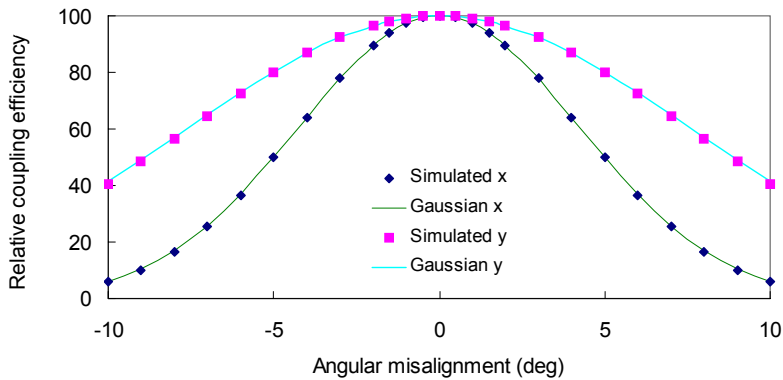

Figure 44. Angular misalignment tolerances in the butt coupling at s = 20 µm.

5.3.3 Coupling optics design

Three coupling methods – tapered fibres, fibre microlenses, and discrete lens coupling – were selected for more detailed evaluation. Standard components were applied in order to avoid the expense and time delay caused by the development of custom components.

Tapered fibres and fibre microlenses are attractive because they combine the simplicity of butt coupling with a reasonable coupling efficiency, reduced optical feedback into the laser, good mechanical stability and ease of packaging. Discrete lens coupling gives more design freedom and enables the use of optical isolators between the laser diode and fibre.

Tapered fibres usually have a spherical end surface acting as a lens. While studying its optimum radius, it was assumed that the fibre core is not tapered and the lens surface has an ideal AR coating (R = 0). The simulations forecast that the maximum coupling efficiency is 54 % when the lens radius is 14 µm and the working distance 17 µm, Figure 45.
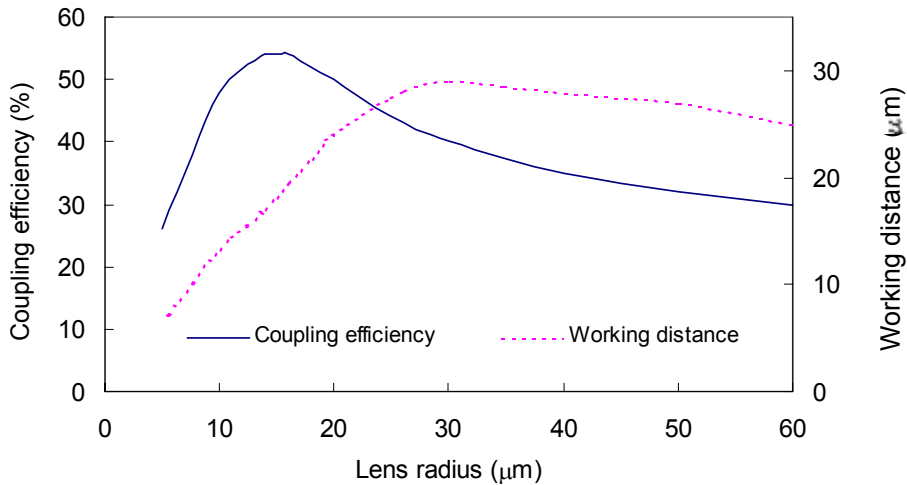

Figure 45. Simulated coupling efficiency and working distance of the spherically lensed fibre taper.

The calculated performance of the tapered fibres purhased for testing (OZ Optics TSMJ-X-1550-9/125-0.25-7-5-18-2 and TSMJ-X-1550-9/125-0.25-18-2.5-6-3-AR) is shown in Table 9. It is noteable that the tapers double the efficiency of the butt coupling at the expense of tighter lateral and axial alignment tolerances. The

tapered fibre coupling is insensitive to wavelength tuning. When the fibre position is fixed, a $\pm$ 10-nm shift in λ changes the coupling efficiency less than 0.4 %.

The ellipticity of the laser beam, $w_{0s,x}/w_{0s,y} \approx 5.7$, sets the upper limit for the coupling efficiency when using rotationally symmetric optics. A wedge-shaped fibre tip only has refractive power in one direction – that is, aligned with the fast axis of the laser beam. When studying the optimum wedge radius, it was assumed that the fibre core is not tapered and the cylindrical lens surface is ideally AR coated. The simulations forecast that the maximum coupling efficiency is 73 % when the lens radius is 8 µm and the working distance 10 µm, Figure 46. When the fibre position is fixed, a $\pm$ 10-nm shift in λ changes the coupling efficiency less than 0.3 %.
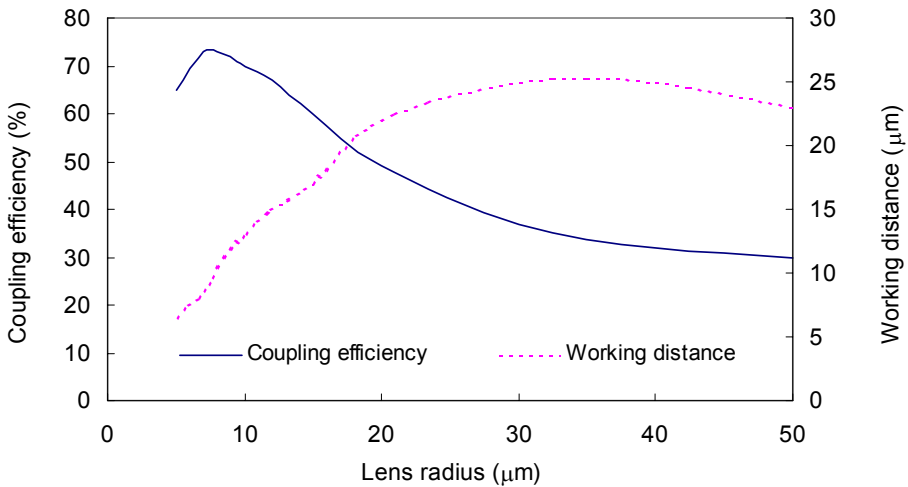

Figure 46. Simulated coupling efficiency and working distance of the wedge-shaped fibre tip.

Fibre tapers and microlenses produce tight lateral, but loose angular, misalignment tolerances. The lateral tolerances can be enlarged by using discrete optics between the laser and the fibre, Figure 47. Here an aspheric glass lens (ALPS FLAC1Z101A) makes a magnified image from the emitting laser surface to the flat fibre endface. The lens has a focal length of 1.01 mm and object side NA of 0.6. The maximum coupling efficiency at the working distance of 510 µm is 43 %, Table 9. When the fibre position is fixed, a $\pm$ 10-nm shift in λ changes the coupling efficiency less than 0.3 %.
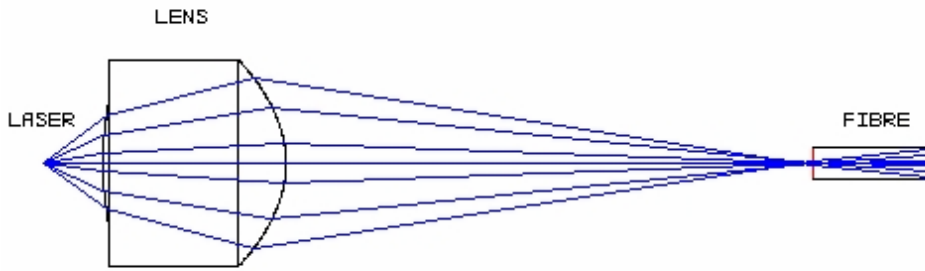
Figure 47. Aspheric lens coupling.

If laser-to-fibre coupling is realised with two lenses, an optical isolator can be used to reduce back-reflections into the laser, Figure 48. Here, aspheric lenses (Geltech 350230 and 350260) make a magnified image from the emitting surface to the fibre endface. Lens 1 has a focal length of 4.5 mm and an object space NA of 0.55. Lens 2 has f = 15.36 mm and an image space NA of 0.16. The maximum coupling efficiency at the working distance of 2.93 mm is 44 %, Table 9. When the fibre position is fixed, a $\pm$ 10-nm shift in λ changes the coupling efficiency less than 0.8 %.
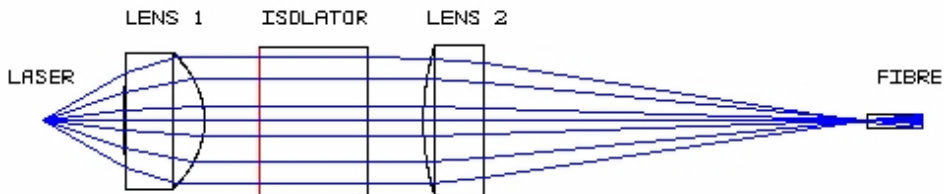
Figure 48. Coupling with an aspheric lens pair.

Table 9 shows the calculated characteristics of the coupling optics alternatives. Although the coupling efficiency is not normally exactly symmetrical with regard to the axial misalignment, Figure 59, the $\pm$ notation is used for ease of comparison. Both tapered and wedged fibres are attractive options for the laser-to-fibre coupling, if the fibre can be attached with sub-micron vertical inaccuracy. Because this was very demanding, the single lens coupling was also prepared.

Table 9. Calculated characteristics of the coupling optics alternatives.

Coupling method	Coupling efficiency (%)	Working distance (µm)	1 dB excess loss tolerance					
			x (µm)	y (µm)	z (µm)	θ_x (°)	θ_y (°)	θ_z (°)
Butt	23	20	± 2.3	± 1.9	+ 21	± 2.9	± 5.1	–
Taper A	45	20	± 1.6	± 0.88	± 9.9	± 4.5	± 14	–
B	48	7	± 1.4	± 0.49	± 3.2	± 8.0	± 16	–
Wedge	73	10	± 2.2	± 0.52	± 4.0	± 2.8	± 4.8	± 6.1
Aspheric lens	43	510	± 6.0	± 2.0	± 58	± 1.3	± 2.5	–
Two aspheric lenses	44	2,930	± 4.9	± 1.9	± 51	± 1.4	± 2.9	–

5.4 Packaging design

5.4.1 Schematic structure of the module

The schematic structure of the prototype modules is shown in Figures 49 and 50. The housing consists of a custom-made cover and a 20-pin metal package (Electrovac) typically used in hybrid electronics. The base plate, manufactured in VTT Electronics' low-temperature co-fired ceramics (LTCC) process, serves as the mounting platform and wiring board for the electrical connections inside the module. The LTCC substrates (Du Pont 951 system) contain precision cavities that helped in positioning the components. Typically, these cavity dimensions possess a horizontal and vertical inaccuracy of $\pm\ 20\ \mu m$ and $\pm\ 10\ \mu m$. The photodiodes (PD 1 and PD 2), monitoring module and FPI had LTCC substrates, whereas the other mechanical parts were made from aluminium alloy.
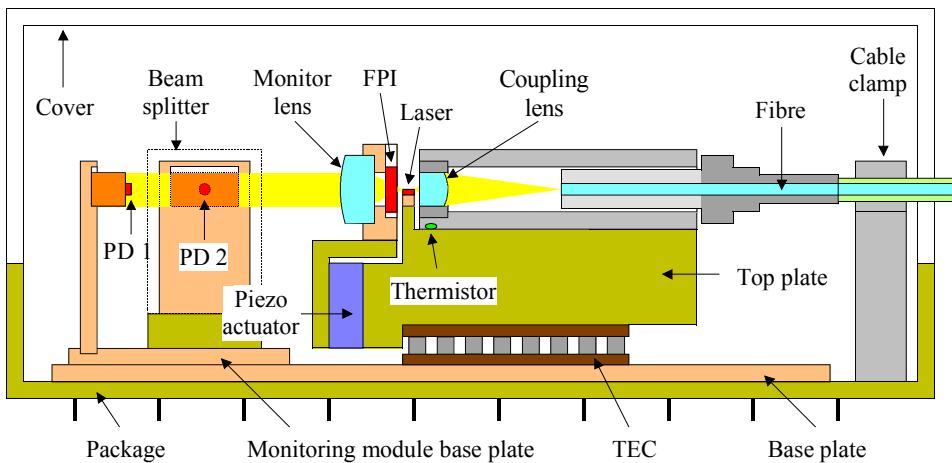
Figure 49. Schematic side view of the prototype module.

The thermoelectric cooler (Melcor ET1.9-35-F1N) attached to the base plate stabilises the temperature of the laser and the laser-to-fibre coupling optomechanics. This minimises the component misalignments caused by the varying ambient temperature. The laser chip lies on an aluminium nitride substrate (CeramTec Alunit®) that has high thermal conductivity ($k_{AlN}\ \geq$

180 W/mK). The thermistor (Shibaura Electronics PB7-43-52) placed near the laser monitors its temperature.
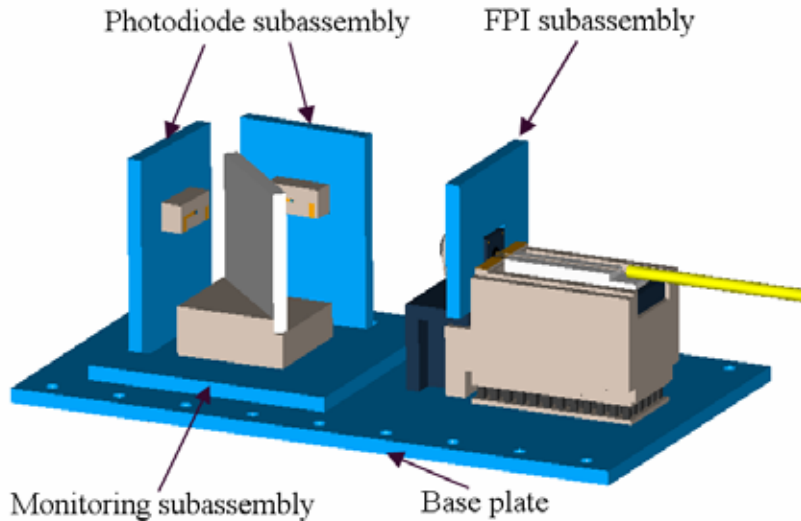
Figure 50. Layout drawing of the module structure.

The FPI attached to the LTCC substrate stands near the AR facet of the laser. Increasing the FPI control voltage extends the separation between the FPI and the laser chip. The laser modelling forecast that the nonlinear wavelength tuning would only occur at discrete regions of distance d. These zones are only 50 to 100 nm wide and can be found in $\lambda/2$ intervals. Because it is impossible to assemble the module with such accuracy, a piezoelectric actuator (Physik Instrumente PL-055.20) fine-tunes the separation between the FPI and laser. Increasing the piezo voltage shortens the length of the external cavity.

The monitor lens (Thorlabs 350390-C) collimates the divergent laser beam transmitted through the FPI and directs it to the laser-monitoring module. This consists of a wavelength-selective beam splitter (Optical Coating Japan) and two photodiodes (Fermionics FD300S2). The coupling lens (ALPS FLAC1Z101A) collects and focuses the HR facet laser beam into the output fibre (Corning SMF-28).

5.4.2 Thermal design

The thermal design can be divided into the temperature stabilisation of the laser chip and the matching of the structural parts in the laser-to-fibre coupling. The characteristics of diode lasers – such as threshold current, slope efficiency, emitting spectra and lifetime – vary with temperature. In WDM applications the stability of the emission wavelength is especially important.

Because the positioning tolerances in the optical coupling are tight, matching the thermal expansion coefficients of the structural parts is critical for achieving stable output power. The movement in x-direction can be minimised by using a symmetrical structure with regard to the optical axis. In y-direction the selection of appropriate materials and material thicknesses reduces thermal effects. The requirements for the coupling optomechanics become much more demanding if the module is not temperature controlled.

The power dissipated in the laser chip P_D is (Coldren and Corzine 1995, p. 56)

$$P_D = P_{elec} - P = UI - P \tag{19}$$

where P_{elec} is the electrical input power, P the optical output power, U the voltage across laser's terminals, and I the drive current. At a drive current of 100 mA, the voltage is 1.5 V and the optical power 20 mW, producing a heat load of 130 mW. The temperature rise in the active region is

$$\Delta T = P_D Z_T \tag{20}$$

where Z_T is the thermal impedance between the active region and the ambient.

There are three heat transfer mechanisms – conduction, convection and radiation – that can transport the dissipated power from the laser into the atmosphere. Here, only the steady state operation of the module is considered; any transient effects are ignored. In convection the heat transfer rate P_{conv} of a surface is (Holman 1997, p. 12)

$$P_{conv} = h_{conv} A \Delta T \tag{21}$$

where h_{conv} is the convection heat transfer coefficient, A the surface area, and ΔT the temperature difference between the surface and the ambient. For natural convection $h_{conv} \approx 5$ W/m²K.

If the temperature difference between the laser chip and the surrounding atmosphere is 5 °C, the heat transfer rate from the top surface and the sides of the laser chip (A = 5 · 10⁻⁷ m²) is about 10 µW. So, convection is not important in the cooling of the laser, Table 10.

Using the Stefan-Bolzmann law (Holman 1997, p. 14), the net radiant exhange P_{rad} between the laser at the temperature T_2 and its surroundings at T_1 can be approximated:

$$P_{rad} = \varepsilon\sigma A(T_2^{\,4} - T_1^{\,4})$$

(22)

where ε is the emissivity of the surface and σ the Stefan-Bolzmann constant ≈ 5.67 · 10⁻⁸ W/m²K⁴. If we assume that the laser chip is a blackbody (ε = 1) at the temperature of 303 K and T_1 = 298 K, the radiant heat transfer from the laser is about 15 µW. The emissivity of the real surfaces is smaller than 1 – for example, $\varepsilon_{Au} \approx 0.03$ (Holman 1997, p. 651).

Table 10. Importance of the heat transfer mechanisms in laser cooling.

Mechanism	Transfer rate	Percentage
Convection	10 µW	0.01
Radiation	< 10 µW	< 0.01
Conduction	> 129.98 mW	> 99.98
Total	130 mW	100

As Table 10 shows, conduction is the only significant heat transfer mechanism. Heat conduction can be increased by using large cross-section areas and thin material layers with high thermal conductivity. The schematic structure of the

laser assembly used in the prototypes is shown in Figure 51. Here the heat generated in the active region flows mostly downward to the upper surface of the TEC, because the thermal conduction through the bonding wires is low – for example, a 1-mm long gold wire with a diameter of 25 µm has a Z_T of 6,400 K/W.
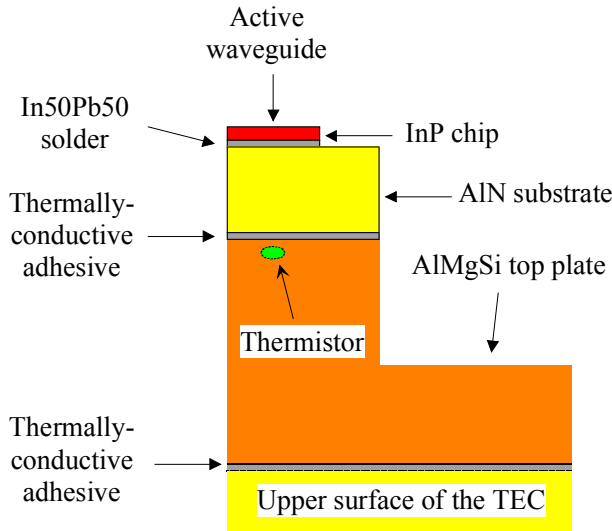

Figure 51. Laser assembly used in the prototypes.

When the laser chip is mounted p-side down, we can assume one-dimensional heat conduction from the active region to the laser substrate (Coldren and Corzine 1995, p. 56). Then the thermal impedance of each material layer is

$$Z_T = \frac{H}{kA} \qquad \text{1-D heat flow} \qquad (23)$$

where H is the thickness, k the thermal conductivity, and A the cross-sectional area of the material layer. Assuming uniform layers without any cracks or voids, the calculated thermal impedance between the upper surface of the TEC and the laser waveguide is as shown in Figure 52. The total impedance is 10 K/W, from which the adhesive bond between the laser substrate and the top plate produces 6 K/W.

When the laser is mounted p-side up, a two-dimensional heat flow must be applied when calculating Z_T (Coldren and Corzine 1995, p. 56)

$$Z_T \approx \frac{\ln(4H/W)}{\pi k L} \qquad \text{2-D heat flow} \qquad (24)$$

where W is the width and L the length of the active region. The total impedance is now 40 K/W, from which the laser chip contributes 30 K/W, Figure 52.
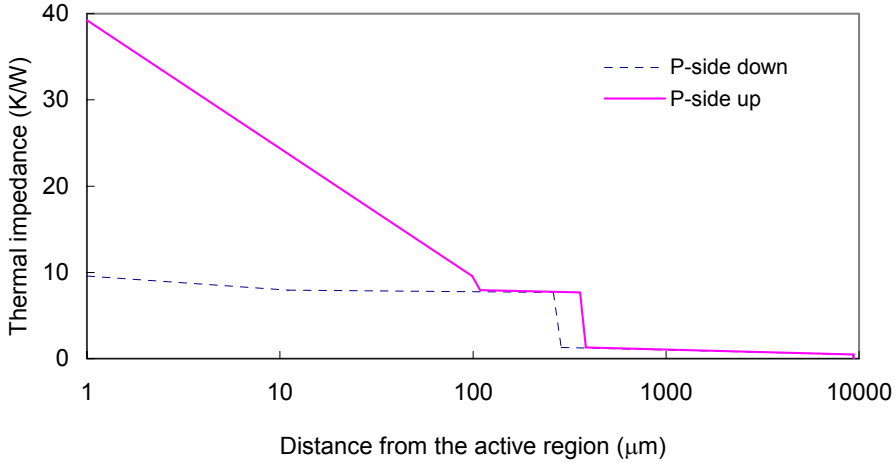

Figure 52. Calculated thermal impedance between the upper surface of the thermoelectric cooler and the laser waveguide.

Because the active waveguide is very near the p-side of the chip, there is a danger that die bonding short-circuits the laser. Therefore, the chip was soldered p-side up, although a p-side down mounting would have given better thermal performance. At the 100-mA drive current the calculated temperature difference between the active region and TEC upper surface is 5 °C.

If the drive current of the laser is varied, the temperature distribution in the underlying materials changes, causing misalignment between the laser and the fibre. The thermal impedance profile shown in Figure 52 and the measured PI curves were used to estimate the vertical movement. Assuming that the temperature of the TEC upper surface is constant, the steady state shift of the laser-to-fibre alignment due to changes in the drive current $\Delta y_{\text{LD-fibre}}/\Delta I_{\text{LD}} \approx$ 2 nm/mA. This is a fairly small figure when compared with the 1-dB excess loss tolerances, Table 9.

5.4.3 Mounting of the fibre

Analysis of the dimensional and assembly tolerances of the tunable laser prototypes showed that active alignment of the fibre is necessary. Since suitable equipment for laser welding or soldering was not available, various adhesives were tested in the fibre mounting; adhesive bonding has potential for the packaging of inexpensive modules because it is an economic process with low equipment investment.

The schematic structure of the fibre mounting is shown in Figure 53. First, a 100-µm-wide groove was sawn into the 1-mm thick glass substrate and the stripped and cleaved fibre was mounted on the substrate with UV-cured adhesive (Loctite 3525). The fibre end was then aligned with the laser beam using the precision positioning device. Finally, the fibre substrate was fixed to the top plate with UV-cured adhesive (Dymax OP-29). According to the data sheets it has shrinkage of 1.2 % during the curing.
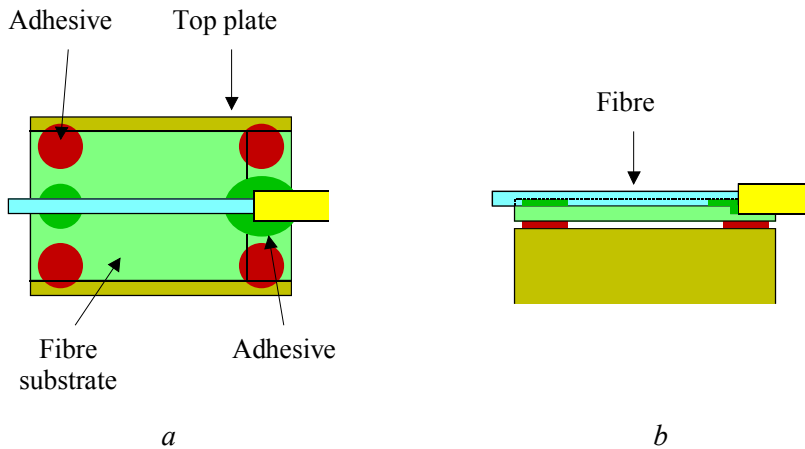

Figure 53. Schematic structure of the fibre mounting. a) Top view and b) side view.

5.5 Module realisation

Three prototypes were assembled using the procedure described below. First, the laser chip was soldered p-side up with a In50Pb50 preform to the Cr/Ni/Au-

metallised AlN substrate using the flip-chip bonder. The substrate was metallised by sputtering and had dimensions of $0.25 \cdot 0.9 \cdot 6.6$ mm^3 (thickness $\cdot$ length $\cdot$ width). The low reflectance laser facet was positioned level with the substrate edge so that the FPI could be brought sufficiently close to the emitting surface. The overhang of the laser chip had to be avoided because it reduces the heat conduction from the active region to the substrate. The top surface of the laser chip was connected to the AlN substrate with three 25-µm Au wires.

The monitoring photodiodes were mounted to their LTCC cavities with heat-curing epoxy and connected to the substrate metallisation with electrically conductive adhesive. The photodiode subassemblies were then assembled to the cavities in the monitoring subassembly (as shown in Figure 50) with UV-cured adhesive. The same adhesive was used to mount the beam splitter to its aluminum base plate, which was attached to the monitoring subassembly. The angle between the surface normal of the photodiodes and the optical axis of the monitoring beam was set at 5° in order to reduce the back-reflection to the laser.

The FPI chip was aligned with the center of its substrate cavity and attached with two drops of high-viscosity UV-cured adhesive as shown in Figure 54. This material is easy to use, has excellent adhesion to the LTCC surfaces and remains flexible after curing. Because the depth of the cavity was 390 µm, the front surface of the 500-µm thick FPI chip came out about 110 µm from the LTCC surface. This ensured that we could bring the FPI near to the emitting laser surface. The FPI was electrically contacted to its substrate via 25-µm Au wires.

The hot side of the TEC was bonded to the LTCC base plate with heat-conductive silicone. After that, the TEC was contacted to the package pins using the microwelding equipment. The piezo actuator was mounted between the top plate and the piezo beam with heat-curing epoxy, and its wires were connected to the package pins with electrically conductive adhesive. The thermistor was attached to the top plate with heat-conductive silicone and connected to the pins using the microwelding equipment.

The laser substrate was attached to the top plate with heat-conductive silicone, and was then bonded to the cold side of the TEC with the same adhesive. After that, the laser substrate was connected to the package pins with 200-µm thick wires that were fixed with electrically conductive adhesive. The LTCC base

plate was attached to the metal package with heat-conductive silicone and the remaining electrical contacts were connected to the package pins.

<center>*a*   *b*</center>
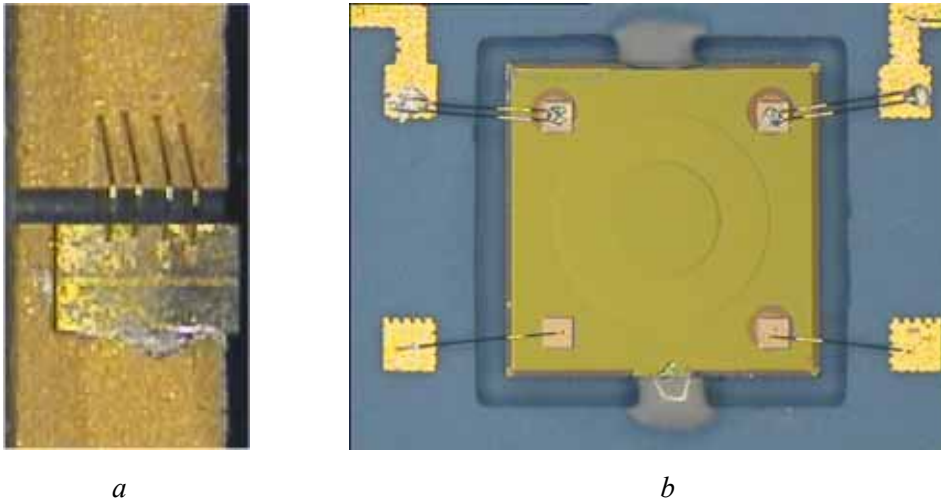
Figure 54. Laser chip and FPI chip assemblies.
a) Laser chip soldered and wire-bonded to the AlN substrate, AR facet on the right and b) FPI attached and wire-bonded to the LTCC substrate cavity.

The monitor lens was fixed to its mounting sleeve with flexible UV-cured adhesive and attached to the other side of the FPI substrate with UV-cured adhesive. The distance between the lens and the FPI was defined by the depth of the lens cavity that was set to 260 µm. Thus it was possible to obtain the collimation of the monitoring beam by using the passive assembly.

The alignment of the FPI subassembly with the laser was one of the most challenging assembly steps, Figure 55. It was performed using the low-pressure gripper and precision-positioning device while monitoring the positioning with two CCD cameras and an optical microscope. After the alignment the FPI subassembly was fixed with UV-cured adhesive. In the realised prototypes the measured values of the laser-to-FPI separation ranged from 42 to 115 µm. This rather large variation was caused by the residual angular errors and the movement of the aligned FPI subassembly during the adhesive curing.
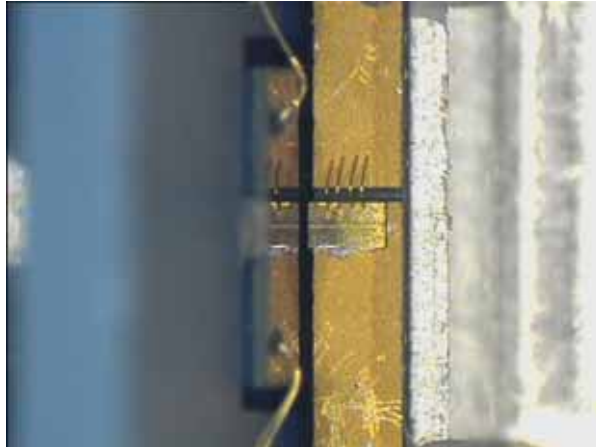
Figure 55. Top view of the laser-to-FPI assembly.

The SM fibre mounting using adhesive bonding was a demanding task. After several trials, the fibres were successfully mounted using the procedure described in Chapter 5.4.3. The additional coupling loss caused by the fibre attachment varied from 1 to 7 dB, depending on the misalignment tolerance of the fibre. This loss corresponded to an average lateral fibre shift of 3 µm.

After mounting, the fibre feed-through was filled with Loctite 3525 and the cover was sealed with Loctite 3109. Figure 56 is a photograph of the realised prototype before the fibre feed-through and the cover was attached.
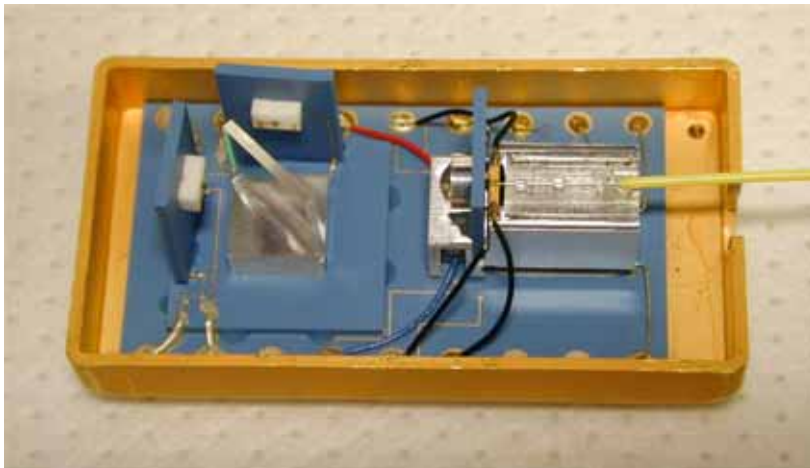
Figure 56. Prototype M1 before the fibre feed-through and the cover was attached.

6. Performance evaluation

6.1 Measurements of the optical coupling characteristics

6.1.1 Solitary laser diodes

The performance of the coupling optics alternatives was measured by attaching the SM fibre to the precision positioning device (Newport AutoAlign 8100), bringing the fibre end into the optimum position, and measuring its lateral and axial misalignment tolerances. All the results presented here were measured using the AR coated facet of the laser II-1. The fibre end was cut and polished in the butt and lens couplings, and had no AR coating.

A laser driver (Newport Modular Controller 8000 with 8605 LDD/TEC Driver) controlled the laser's drive current and temperature. A 2-km long lauch fibre package (NK Cables FSM-2000) was used between the fibre pigtail and the optical power meter (Newport 2832-C with 818-IS-1 Sensor) to ensure that only the single-mode power was measured. The coupling efficiency was calculated as the ratio of the linear slopes of the fibre-coupled PI curve and the AR coated laser facet PI curve.

The maximum measured butt coupling efficiency at the 20-µm working distance was 22 %, which corresponds well to the theoretical value of 23 %. The lateral misalignment tolerances are shown in Figure 57, where we can see that the measured values match the calculated graph better in the x-z plane than in the y-z plane.

In the butt coupling the output power showed a periodic undulation when the fibre moved along the optical axis, Figure 58. This was due to the optical feedback from the fibre end face into the laser cavity (Sidorin and Howe 1997), which had not been taken into account in the calculations. Tapered and wedged fibres that were not AR coated behaved similarly, whereas the lens couplings were fairly insensitive to the optical feedback from the fibre end, Figure 59.
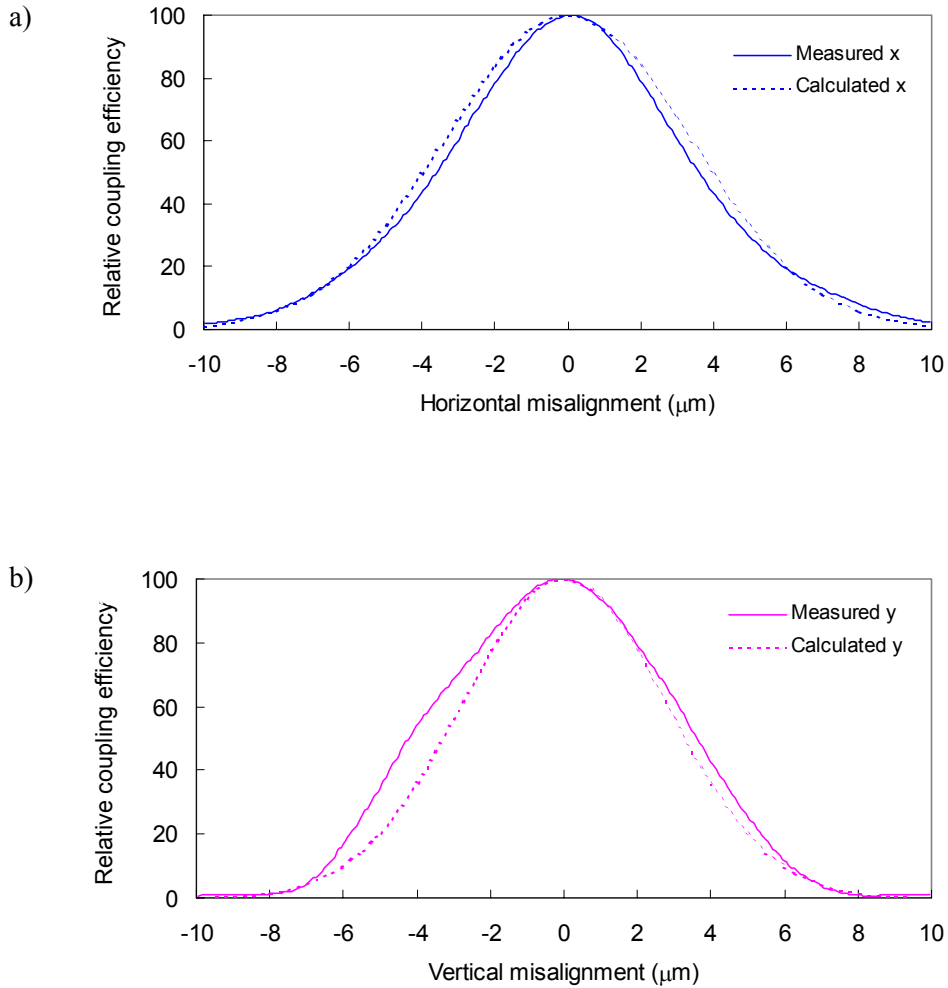
*Figure 57. Lateral misalignment tolerances for the butt coupling. a) In x-z plane and b) in y-z plane.*

The tapered fibres A and B obtained a maximum coupling efficiency of 38 % and 39 %, Table 11. Although taper A is a better option for our prototypes due to the looser alignment tolerances, it is still very sensitive to vertical misalignment. For example, a 2-µm centering error decreases the fibre-coupled power 5 dB.
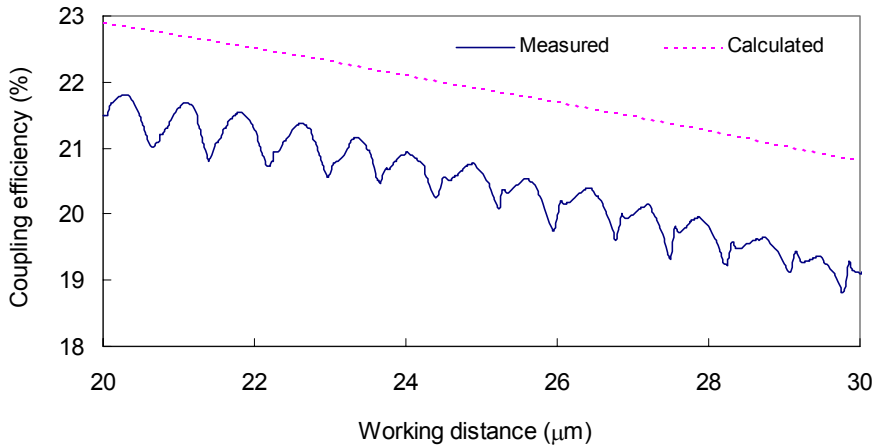
Figure 58. Axial misalignment tolerance for the butt coupling.
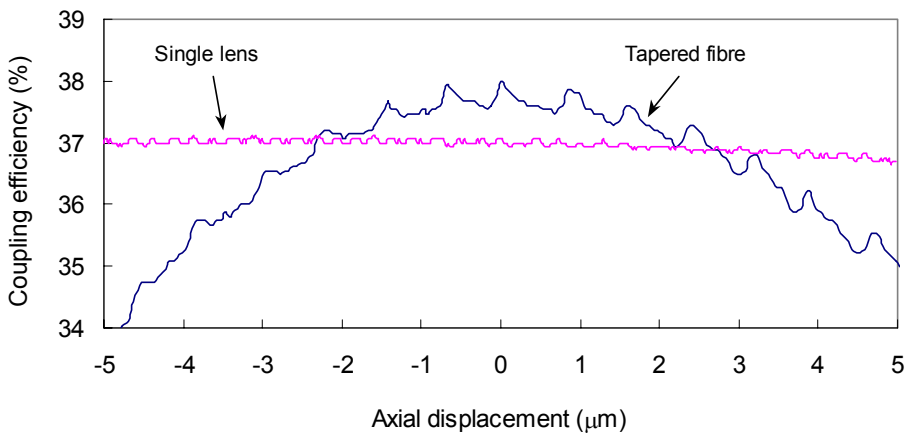
Figure 59. Output power fluctuation in the tapered fibre and lens couplings.

The best wedge-shaped fibre obtained a maximum coupling efficiency of 61 %, Table 11. Because the manufacturer (Seikoh-Giken, Japan) did not give the optical parameters – such as wedge radius and taper angle – the coupling characteristics were not calculated. The disadvantages of the wedged fibres are the very tight vertical misalignment tolerances and short working distance. It was also noticed that the non-AR coated fibre end near the emitting facet made the laser susceptible to power and wavelength variations.

Of the discrete lens options, the two-lens coupling attained the highest coupling efficiency and the widest alignment tolerances, Table 11. However, its dimensions are rather large with a mount diameter of 9.2 mm and laser-to-fibre distance of 23 mm. Therefore, the single lens coupling was selected to be used in the prototypes, which almost doubled the efficiency compared to butt coupling but did not tighten the lateral and axial misalignment tolerances.

Table 11. Characteristics of the alternative coupling optics.

Coupling method		Coupling efficiency (%)		1 dB excess loss tolerance					
				x (µm)		y (µm)		z (µm)	
		Measured	Calculated	Meas.	Calc.	Meas.	Calc.	Meas.	Calc.
Butt		22	23	± 2.1	± 2.3	± 2.0	± 1.9	+ 16	+ 21
Taper	A	38	45	± 1.4	± 1.6	± 0.89	± 0.88	± 8.2	± 9.9
	B	39	48	± 1.1	± 1.4	± 0.40	± 0.49	± 2.5	± 3.2
Wedge		61	–	± 2.0	–	± 0.37	–	± 1.7	–
Aspheric lens		37	43	± 3.1	± 6.0	± 2.1	± 2.0	± 37	± 58
Two aspheric lenses		45	44	± 4.3	± 4.9	± 2.2	± 1.9	± 56	± 51

6.1.2 FPI-tuned laser diodes

The coupling efficiency measurements carried out using solitary laser diodes indicated that the single aspheric lens (η = 37 %) would be the optimum choice for the tunable laser modules. However, when testing the assembled prototypes the maximum obtained efficiency was only about 10 %, which implied that the FPI standing near the AR-coated facet deteriorated the laser-to-fibre coupling.

This was studied by bringing a small mirror (2.8 · 2.8 mm^2, R $\approx$ 90 %) close to the AR facet of the solitary laser and measuring the transverse profile of the HR facet beam using a 2-m long SM fibre (Corning SMF-28). The drive current was 90 mA and the laser-to-fibre distance 500 μm, giving an angular resolution of about 1°.

When the mirror was far away (> 4 mm) from the laser, the HR facet beam irradiance profile conformed to the Gaussian distribution with divergence angles of α_{fx} = 4.9° and α_{fy} = 5.8°, Figure 60a. As the mirror was brought closer to the laser the beam became distorted, especially in the y-z plane, Figure 60b–d.

Efficient SM fibre coupling requires a Gaussian laser beam, and ripples in the distribution decrease the performance. Jeon et al. found that quite small far-field pattern ripples having amplitude of about ± 5 % lowered the coupling efficiency to lensed fibres from 70 to 63 % (Jeon et al. 1997). Presby and Giles (1993) noticed similar results. In our prototypes the laser beam departs from the Gaussian distribution much more than in these publications.

It was also found that wavelength tuning transforms the power distribution of the laser beam, which changes the fibre output power. Figure 60 indicates that reducing the FPI-to-laser separation decreases the amplitude of the power fluctuations. However, it was not possible change the FPI-to-laser separation in the realised prototypes. Because of the rather poor performance of the lens coupling, the prototypes were modified to apply butt joint.

a)
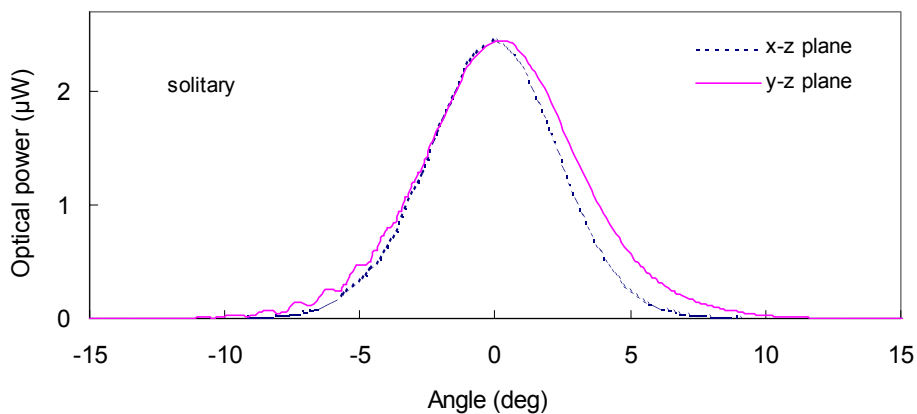
b)
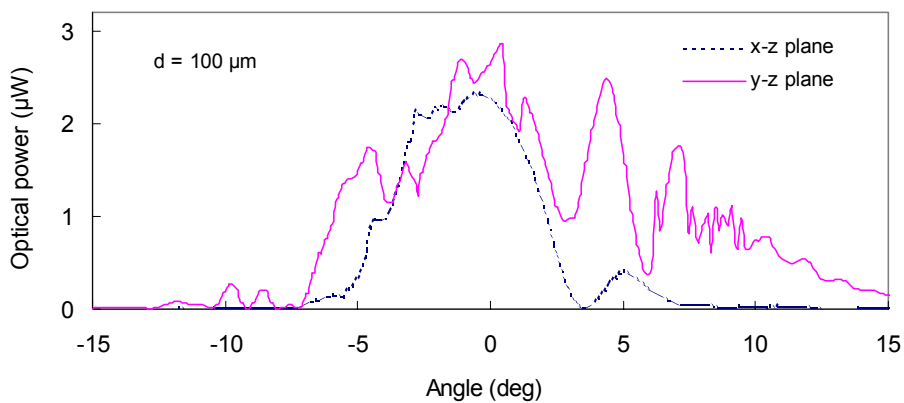
Figure 60. HR facet beam distribution of the laser III-A. a) Solitary laser and b) mirror-to-laser separation = 100 μm.

c)

d)
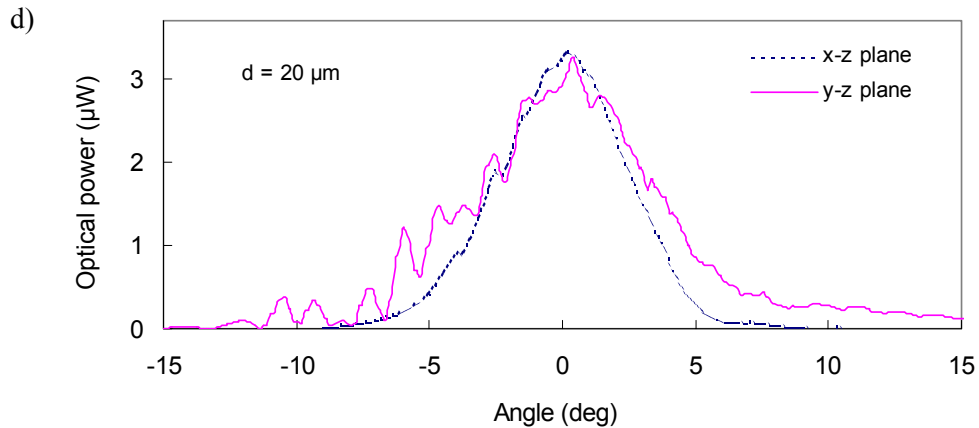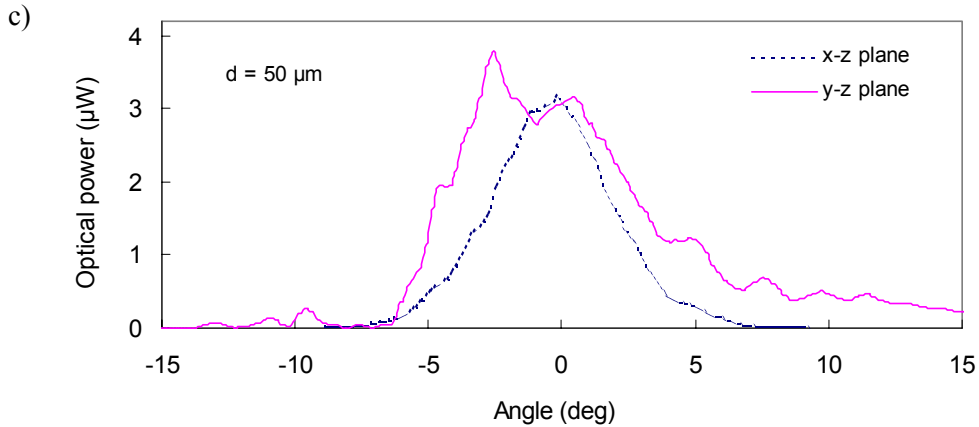
Figure 60. HR facet beam distribution of the laser III-A. c) Mirror-to-laser separation = 50 μm and d) mirror-to-laser separation = 20 μm.

Ventrudo and Cassidy studied short external cavity lasers and found that interference occurs between the light emitted from the HR laser facet and the light emitted from the AR laser facet that is reflected by the external mirror. For an isolated laser, the light emitted from each facet propagates in opposite directions and does not, therefore, interfere with each other (Ventrudo and Cassidy 1993).

In our prototypes the insertion of the FPI partially reflected the light emitted from the AR facet, and this light interfered with the HR facet beam, Figure 61. Because InP is transparent at the emitting wavelengths, light also travels through the laser chip (Streetman and Banerjee 2000, pp. 19 and 110).

a)

b)
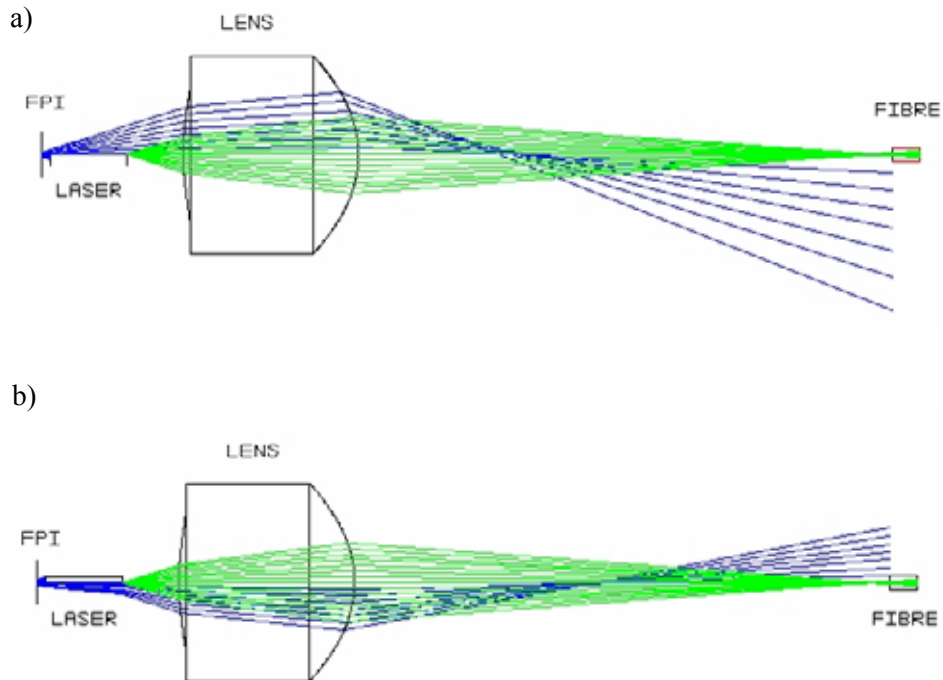
Figure 61. Ray paths of the interfering wave fronts. a) Above the laser axis and b) below the axis through the laser chip.

It is also possible that the distribution of the solitary laser beam emitted from the AR-coated facet is different than the HR facet beam. Then the AR facet beam can conform to the Gaussian distribution, whereas the HR beam also has higher order modes. This phenomenon can be explained by the angular dependence of the reflection coefficient of the coating materials and its influence on the optical mode selection (Alferov et al. 1995). The manufacturer of our lasers discovered this effect in the x-z plane far-field pattern of the lasers similar to the devices used in our prototypes. Unfortunately, the HR facet beam distribution of the lasers was not measured before they were assembled into the prototypes.

6.2 Testing of the prototypes

6.2.1 Test set-up

The schematic set-up used in the prototype testing at VTT Electronics is shown in Figure 62. A laser driver (Newport Modular Controller 8000 with 8605 LDD/TEC Driver) controlled the laser's current and temperature, and a precision current meter (Keithley 2400 SourceMeter) measured the output current of the monitoring photodiodes. Laboratory power supplies (IL-Power LPS-225 and LPS-300) adjusted the operating voltage of the FPI and piezoelectric transducer. A 2-km long launch fibre package (NK Cables FSM-2000) was inserted between the fibre pigtail and optical power meter (Newport 2832-C with 818-IS-1 Sensor) or spectrum analyser (Ando AQ-6315B) to ensure that only the single-mode output power was measured. The resolution of the spectrum analyser was 0.05 nm.
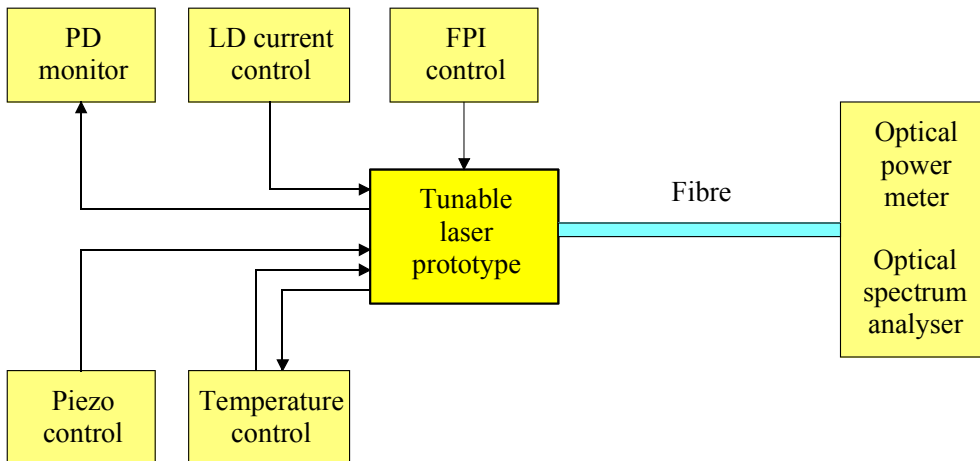
Figure 62. Schematic set-up of the prototype testing at VTT Electronics.

6.2.2 Spectral behaviour of the tuning

Three types of spectral behaviour were discovered during the prototype tuning tests. The most common was multimode lasing, where the spectrum consisted of the principal mode and several side modes, Figure 63a. During tuning the distribution of the laser power between the modes changed until the principal wavelength hopped to the adjacent longitudinal mode. This behaviour was typical in the linear tuning, where the FPI acted as a moving plane mirror.

When adjusting both the piezo and FPI control voltages it was possible to obtain quasi-single-mode lasing, Figure 63b. Then the principal mode was very strong and the side mode suppression ratio was 20 to 30 dB. When the laser tuned to the next principal mode, the spectrum usually became multimode and the piezo and FPI voltages had to be readjusted to obtain quasi-SM operation.

The third spectrum type occurred when the end of the tuning range was approached. For example, if the spectrum was near the shortest obtainable principal wavelength, the laser power began to transfer to the upper end of the tuning range as the spectrum was further tuned down. If the tuning was continued further downwards, two multimode spectra at the opposite ends of the wavelength range were obtained, Figure 63c, and, after that, the laser power shifted entirely to the upper end of the tuning range.
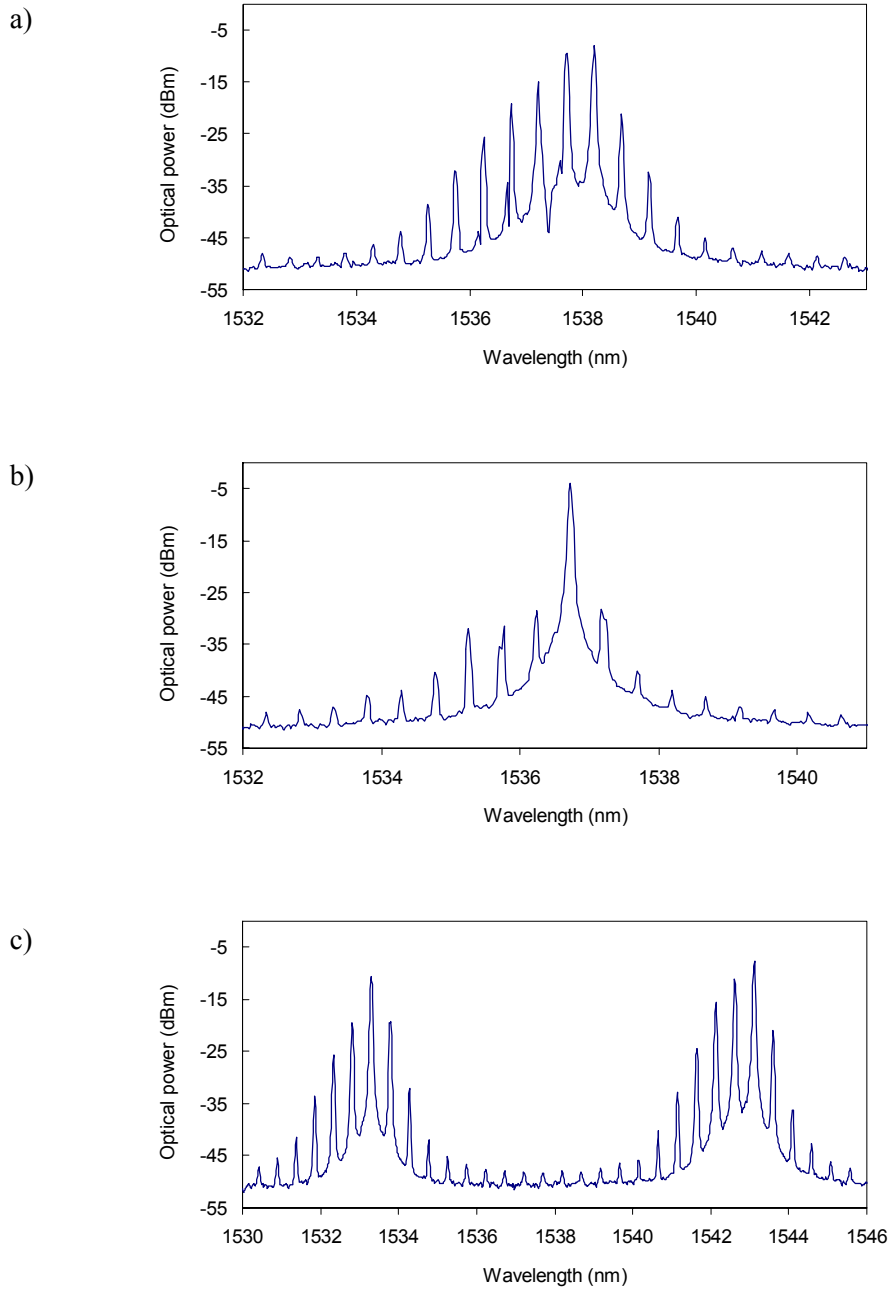
Figure 63. Output spectra types. a) Multimode b) quasi-single-mode and c) multimode at the opposite ends of the tuning range.

122

6.2.3 Prototype M1

The testing of the prototype M1 began with measuring its wavelength tuning range by keeping the control voltage of the FPI at 0 V and gradually changing the voltage over the piezoelectric transducer. In this case the resonance region (transmission peak) of the FPI is far away from the lasing wavelengths and the FPI acts like a plane mirror. In the results shown here the laser temperature was 25 °C and the drive current 90 mA unless otherwise mentioned.

The typical principal wavelength as a function of the piezo voltage is shown in Figure 64. The wavelength tuned discontinuously by mode hopping and rather linearly with the piezo voltage. The spacing between adjacent modes was 0.49 nm and the maximum tuning range was 13 nm. This same range was obtained when the laser drive current varied from 60 to 100 mA.
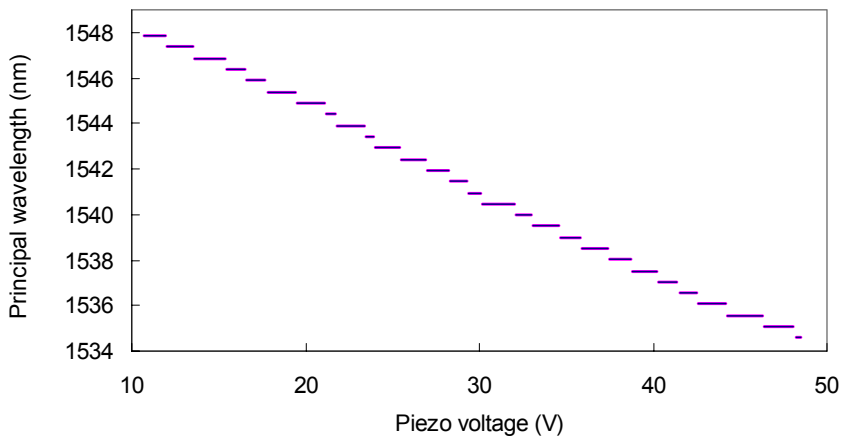
Figure 64. Typical principal wavelength of the prototype M1 in piezo tuning.

The hysteresis of the principal wavelength was measured by increasing the piezo voltage from 10 to 50 V and decreasing it back to 10 V. The largest measured difference between the wavelengths of the same principal mode was 0.03 nm. The spectral width and output power were also rather insensitive to the direction of the piezo voltage change.

When the laser drive current was raised from 80 to 100 mA, the principal wavelength shifted 0.092 nm, which corresponded to a drive current sensitivity

of 0.005 nm/mA. Larger drive current variations caused mode hops. The laser spectrum was sensitive to the temperature variations inside the module; a temperature change of 0.1 °C typically shifted the principal wavelength one or two longitudinal mode spacings, corresponding to about 0.5 to 1 nm.

The piezo-tuned spectrum consisted of the principal mode and a few side modes, Figure 65. Here the peak powers are normalised to better compare the spectra and the absolute output power is shown in Figure 66. The number of modes that contained at least 10 % of the power in the central peak varied between 1 and 4. The average root mean squared (rms) spectral width was 0.69 nm.
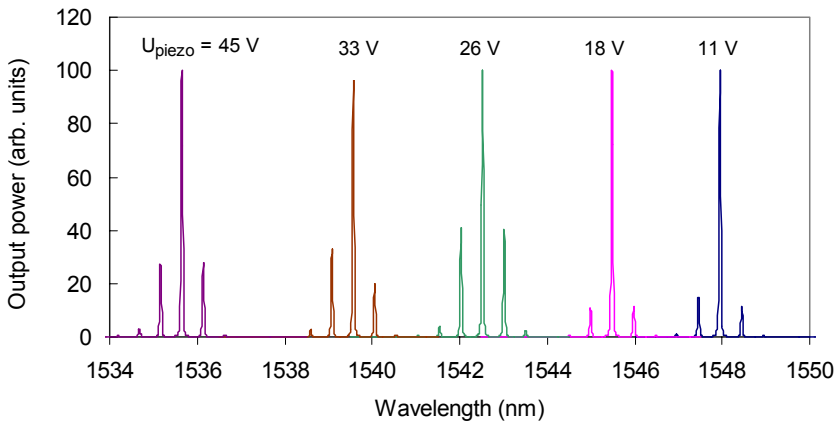
Figure 65. Superimposed spectra of the prototype M1 in piezo tuning.

The ratio of the maximum and minimum output power was 1.5, Figure 66. The average power at 70-mA and 90-mA drive current was 70 µW and 100 µW, respectively. There are three factors that affect the output power fluctuation as the function of the wavelength. First, the wavelength tuning modifies the effective reflectance of the AR facet, which changes the total power of the laser. Second, the variation in the effective reflectance also alters the power distribution between the AR and HR facets. Third, the wavelength tuning transforms the power distribution in the HR facet output beam, which changes the fibre coupling efficiency.

The linear FPI-tuning characteristics were measured by adjusting the piezo voltage so that the operation point moved to the shortest obtainable principal wavelength. Then the FPI voltage was gradually increased. The maximum range

of the linear FPI-tuning using a constant piezo voltage was 7 nm. This value is limited by the maximum displacement of the moving mirror before the FPI resonance region starts to disturb the linear tuning. The wavelength tuned discontinuously by mode hopping with a spacing of 0.49 nm.
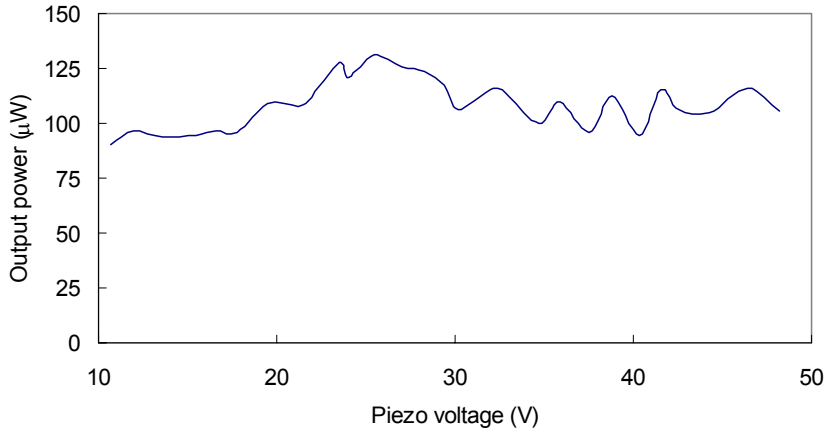
Figure 66. Output power of the prototype M1 in piezo tuning.

The entire tuning range of 13 nm can be covered by using two piezo voltages, as shown in Figure 67. Here the principal wavelength tunes nonlinearly with the FPI voltage because the movable mirror of the FPI moves nonlinearly with its control voltage (Sidorin 1999b). Otherwise, the linear FPI-tuning behaves in the same way as the piezo tuning.
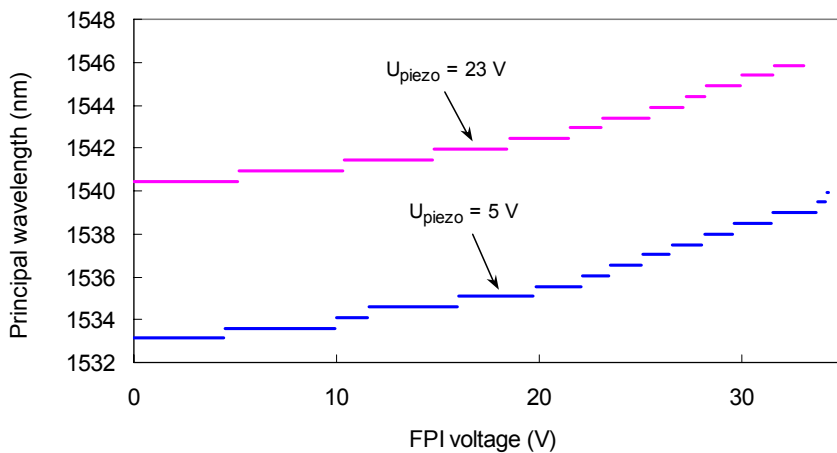
Figure 67. Principal wavelength of the prototype M1 in linear FPI-tuning.

The measured output spectra, as shown in Figure 68 where the peak powers are normalised, were similar to piezo tuning. The number of modes that contained at least 10 % of the power in the central peak varied between 1 and 4, and the average rms spectral width was 0.65 nm. The ratio of the maximum and minimum output power was 1.5, Figure 69.
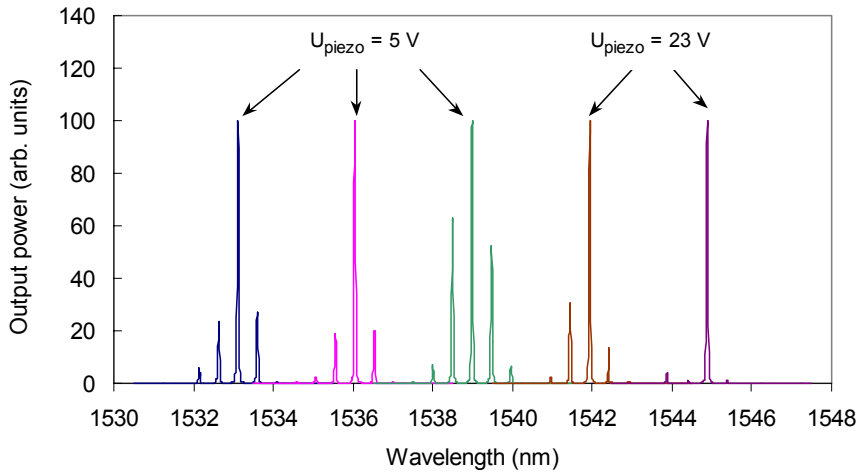

Figure 68. Superimposed spectra of the prototype M1 in linear FPI-tuning.
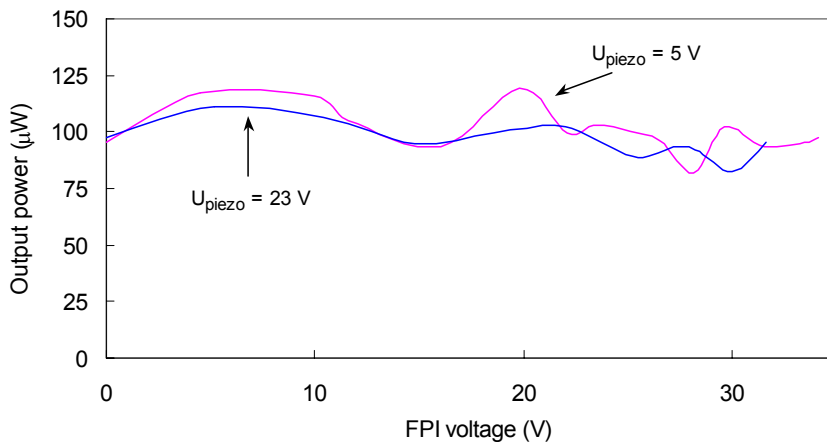
Figure 69. Output power of the prototype M1 in linear FPI-tuning.

The nonlinear FPI-tuning characteristics differ substantially from the piezo and linear FPI-tuning results. When the piezo voltage was kept constant, the maximum tuning range of the principal wavelength was only 2 nm, Figure 70. The nonlinear tuning takes place in a quite narrow FPI voltage range of 0.5 V, which requires stable control electronics.
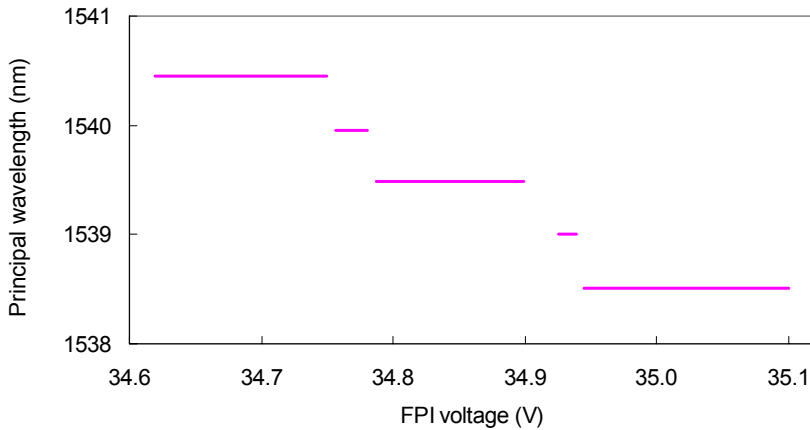
Figure 70. Principal wavelength of the prototype M1 in nonlinear FPI-tuning.

The spectra of the nonlinear tuning were much narrower than in the linear tuning, Figure 71. Typically, there was one dominating mode and the side modes contained less than 10 % of the power in the central peak. The ratio of the maximum and minimum output power was 1.2, Figure 72.
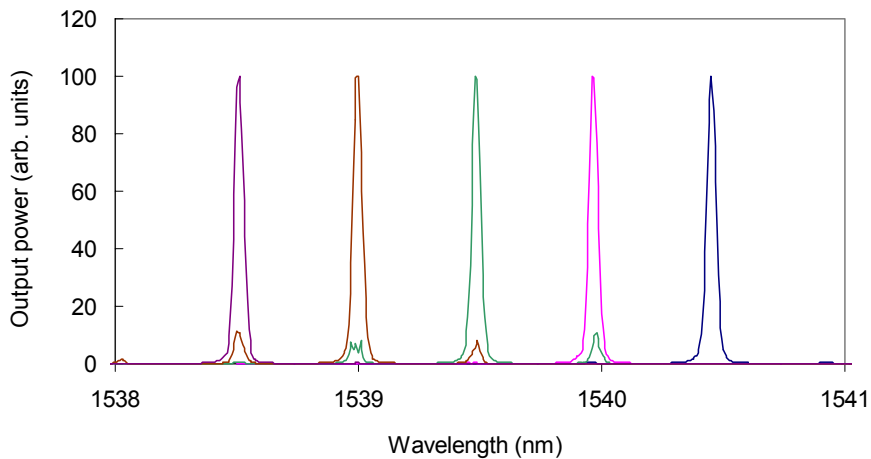
Figure 71. Superimposed spectra of the prototype M1 in nonlinear FPI-tuning.
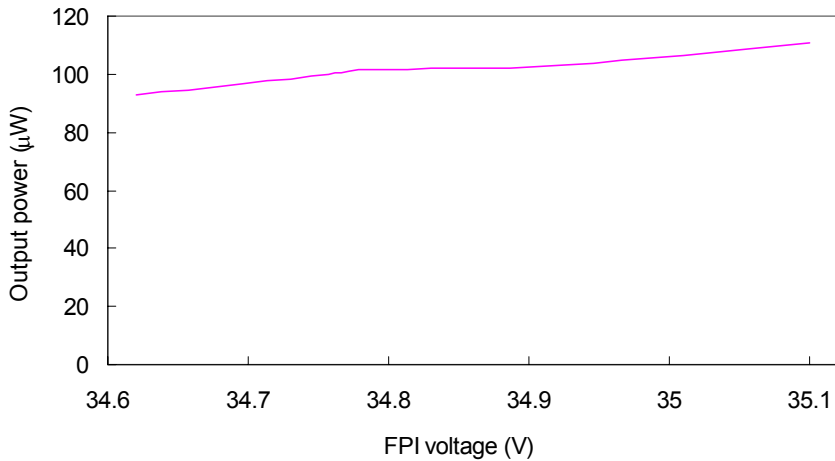
Figure 72. Output power of the prototype M1 in nonlinear FPI-tuning.

Although the nonlinear tuning region using a constant piezo voltage was small, it was possible to sweep it across the total tuning range. When simultaneously optimising both the piezo and FPI control voltages, named the combined tuning, a wavelength range of 13 nm was obtained, Figure 73. Here the FPI control voltage varied between 34 and 35 V, and the piezo voltage scanned through its one operation period – e.g., 10 to 50 V.
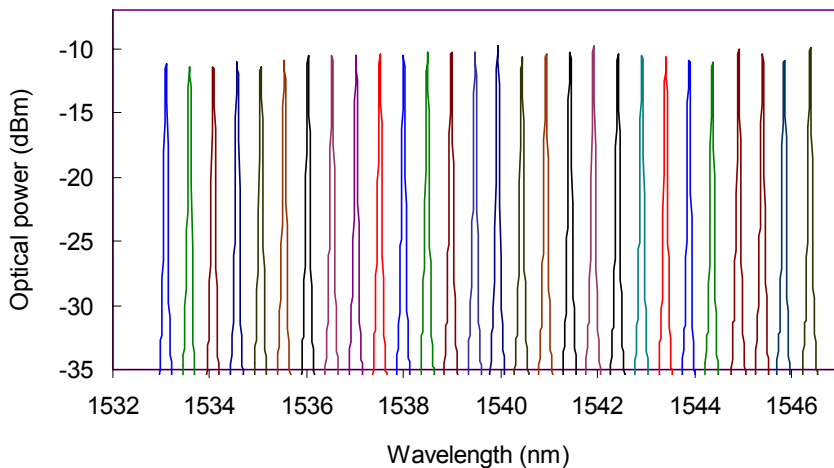
Figure 73. Superimposed spectra of the prototype M1 in combined tuning.

In combined tuning the output spectrum consisted of one dominating mode and weak side modes. The influence of the drive current on the laser spectra is shown in Figure 74. For clarity, the 70-mA graph has been lowered by 10 dB, and the 50-mA graph by 20 dB, in order to reduce overlapping. When the drive current rose from 50 to 70 mA, the same longitudinal mode dominated, but its wavelength increased by 0.08 nm. When the current increased to 90 mA, the peak power hopped to the next mode. The side mode suppression ratio at the 90-mA drive current was better than 25 dB. The main characteristics of the prototype M1 are shown in Table 12.
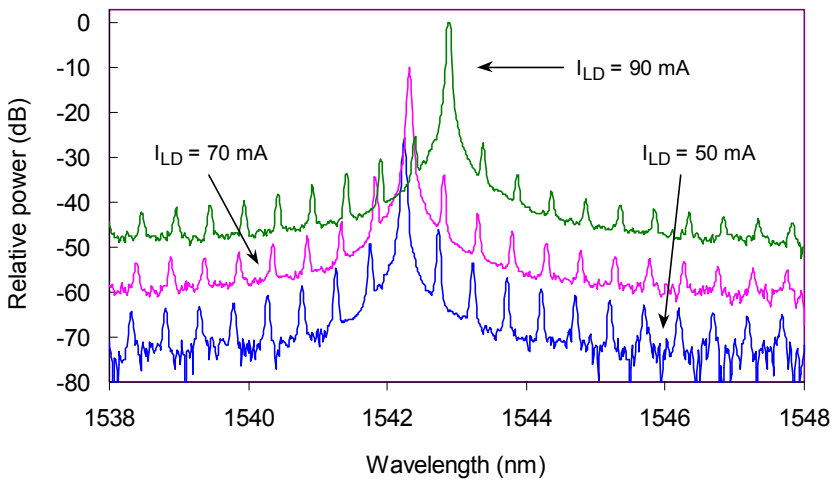
Figure 74. Spectrum of the prototype M1 in combined tuning.

It is interesting to compare the spectrum of the tunable laser with the free-running component before the FPI was assembled. Figure 75 shows that the linear tuning also narrows the spectrum. Here the free-running laser spectrum width at the level 20 dB below the central peak was $\Delta\lambda_{-20dB} = 5.2$ nm, whereas the same chip using linear or nonlinear tuning had a $\Delta\lambda_{-20dB}$ of 1.0 nm and 0.18 nm respectively.

In both multimode and single-mode tuning the side modes of the laser are suppressed compared to a free-running laser. This suppression is due to the wavelength dependent effective reflectance from the external cavity. The wavelength dependency is caused by the interference between the reflections from the FPI and from the (internal) laser facet. In multimode operation, the

129

wavelength separation between the interference maxima in the effective reflectance spectrum is $\Delta\lambda_{MM} = \lambda^2/2d$, which is a familiar rule for etalon modes.

In single-mode operation, this rule is broken. The FPI resonance band accelerates the phase shift in the function of wavelength leading to $\Delta\lambda_{SM} < \lambda^2/2d$. Therefore the wavelength dependence of the effective reflectance is stronger and the side-mode suppression ratio larger in the single-mode tuning region (Heikkinen et al. 2004).
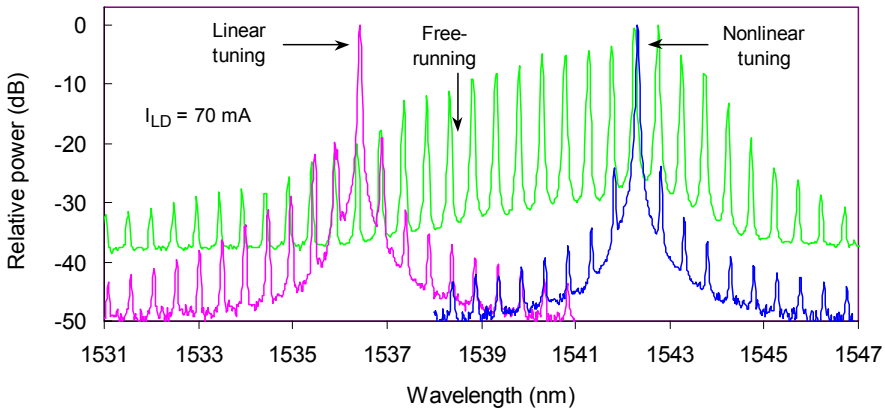
Figure 75. Spectra of the tunable and free-running laser of the prototype M1 when laser current was 70 mA.

The monitoring photodiode currents that were measured during the linear FPI-tuning are shown in Figure 76. The photodiode PD 1 monitored the power that was transmitted through the wavelength-selective beam splitter, and PD 2 measured the power reflected from it. When the laser diode was not operating, the dark current of the detectors was 0.1 nA.

We see that at low voltages when the transmission peak of the FPI is far away from the principal wavelength λ_0, both monitoring currents are fairly small. When the FPI resonance region closes in on λ_0, the current from PD 1 increases more rapidly than the current from PD 2. This is partly due to the transmittance of the beam splitter that increases with the wavelength, Figure 77. The corresponding decrease in the reflectance of the beam splitter therefore slightly weakens the increase of current from PD 2.
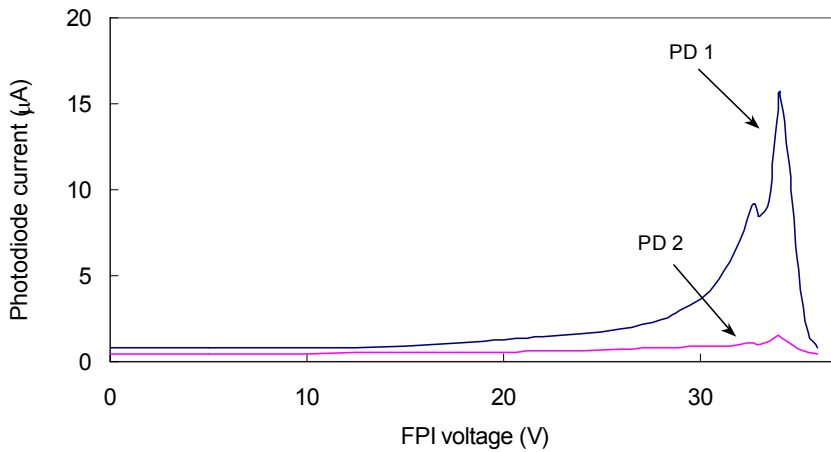
Figure 76. Monitoring photodiode currents in linear FPI-tuning.

The mean wavelength of the monitoring beam was calculated using the measured photodiode currents and spectral characteristics of the beam splitter. The transmittance graph of the beam splitter was approximated to be linear in the wavelength range from 1,535 to 1,545 nm and to have a slope of 0.067/nm.
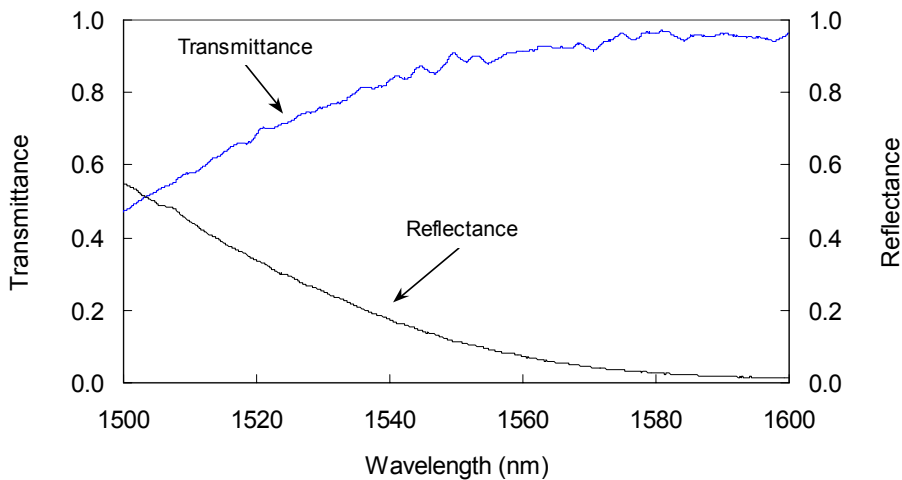
Figure 77. Measured transmittance and reflectance of the beam splitter.

The calculated values are compared to the measured mean wavelength of the fibre output in Figure 78. Both in the piezo tuning and in the linear-FPI tuning, the correspondence between the measurements and calculations is poor. These

results together with the odd photodiode current characteristics shown in Figure 76 indicate that the wavelength monitoring system needs further development.
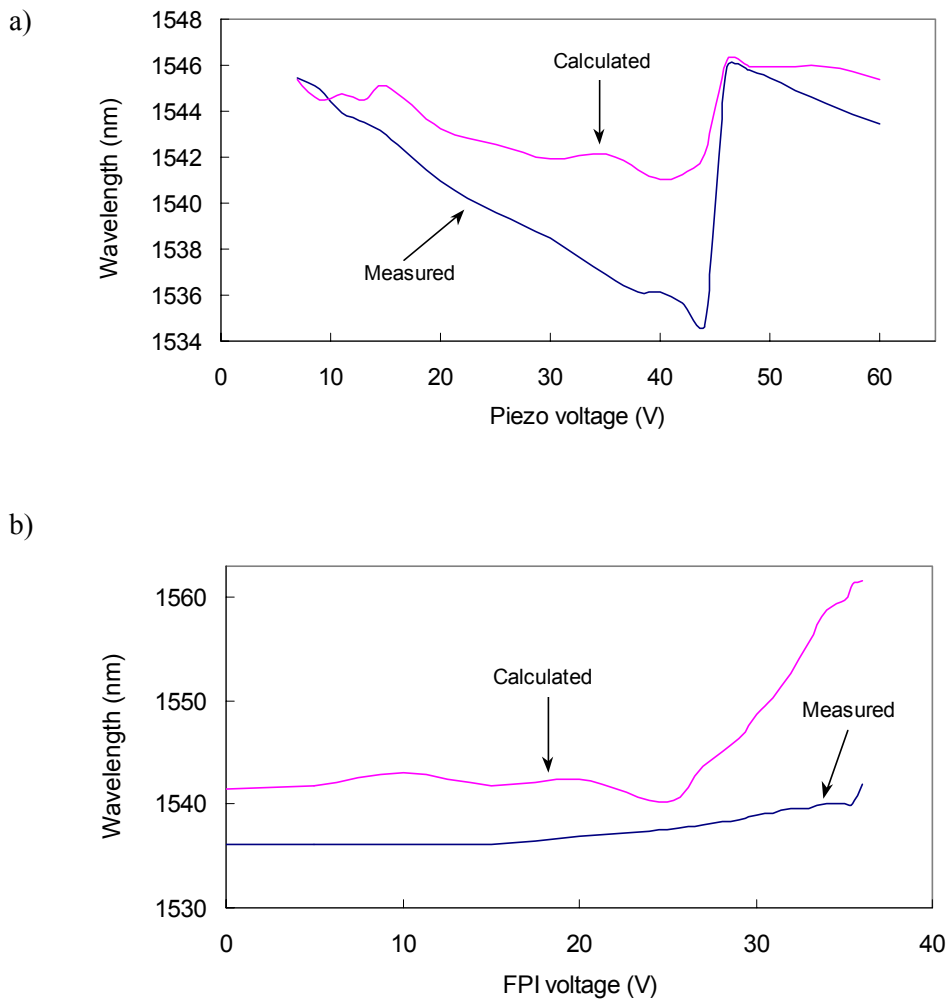
Figure 78. Mean calculated and measured wavelengths. a) In piezo tuning and b) in linear FPI-tuning.

The prototype M1 was already sealed during these measurements and it was impossible to disassemble it without serious damage to the fibre attachment. Therefore we used the unsealed prototype M3 when comparing the spectrum of

the beam coupled into the SM output fibre to the beam transmitted through the FPI. The mean wavelength of both beams as the function of the FPI control voltage is shown in Figure 79. The results are almost identical, and the small differences between them cannot explain the behaviour shown in Figure 78.
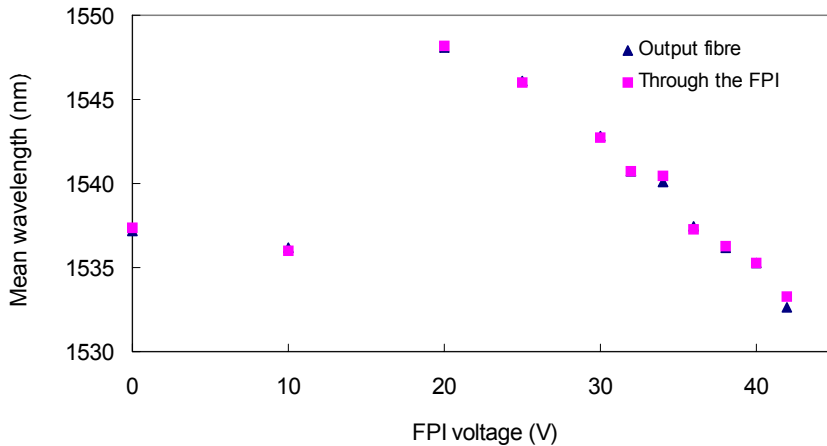
Figure 79. Mean wavelength of the prototype M3 in linear FPI-tuning.

The transverse profile of the monitoring beam was measured with a 200-µm-core fibre having a NA of 0.48 (Thorlabs FT-200-URT). Figure 80 presents the horizontal and vertical irradiance distributions measured using three FPI voltages. The ripples in the graphs resemble those that were found when measuring the HR laser facet beam distributions, Figure 60. Here we see that the irradiance in the y-z plane depends strongly on the FPI voltage – that is, output wavelength spectrum. This means that the monitoring currents are not only a function of the total power transmitted through the FPI but they also depend on the irradiance distribution that varies with the tuning. If corresponding effect is also present in the prototype M1, it can explain the peculiar monitoring current behaviour shown in Figure 76. Overall this phenomenon complicates the tunable laser wavelength monitoring.

a)

b)
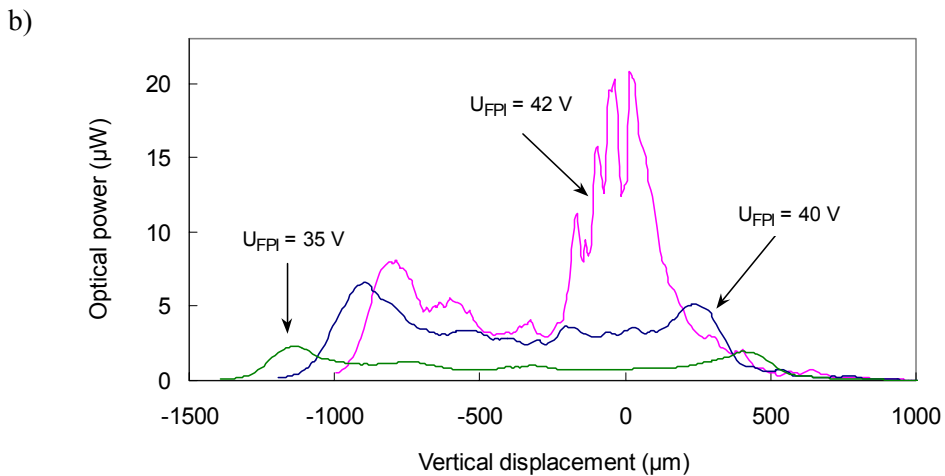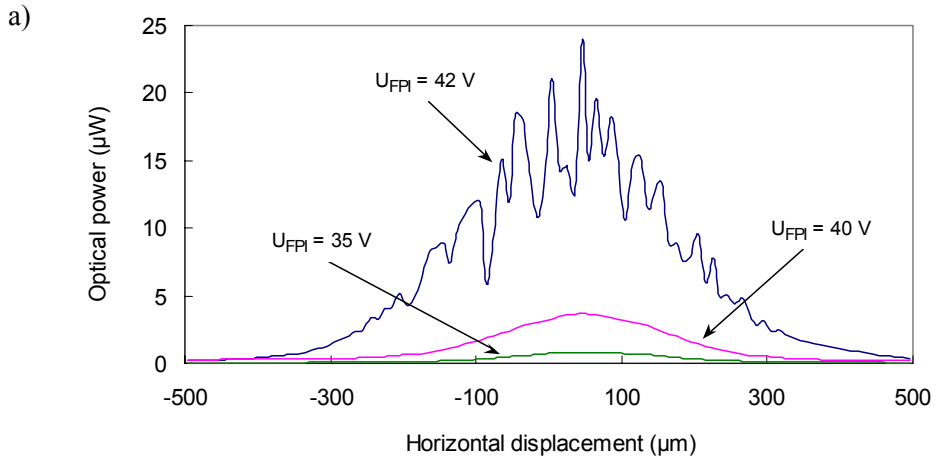
Figure 80. Irradiance distributions of the prototype M3 monitoring beam. a) In x-z plane and b) in y-z plane.

6.2.4 Prototype M2

The principal wavelength of the prototype M2 in the piezo tuning is shown in Figure 81. The laser temperature was 25 °C and the drive current 90 mA. The wavelength tuned discontinuously by mode hopping where the spacing between adjacent modes was 0.49 nm. The maximum tuning range was 8.3 nm.
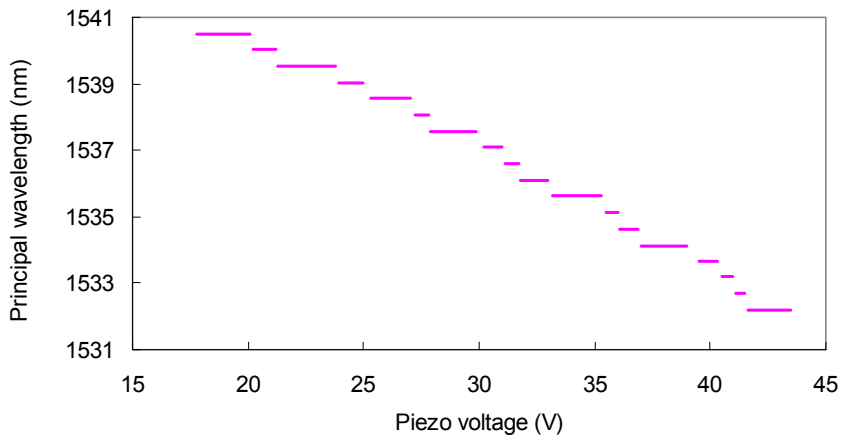
Figure 81. Typical principal wavelength of the prototype M2 in piezo tuning.

The piezo-tuned spectrum of the prototype M2 was narrower than in M1. The number of modes that contained at least 10 % of the power in the central peak varied between 1 and 3 and the average rms spectral width was 0.38 nm. The mean output power was 440 µW.

The maximum linear FPI-tuning range using a constant piezo voltage was 4.4 nm. The tuning range of 8 nm can be covered by using two piezo voltages, Figure 82. The average rms spectral width in the linear FPI-tuning was 0.65 nm.

Prototype M2 did not operate in the nonlinear FPI-tuning mode. A possible explanation for this is the fairly large separation of 115 µm between the FPI and laser. M2 also showed a different combined tuning behaviour than M1, Figure 83. The power of the principal modes varied strongly with a peak-to-peak variation of 6.5 dB, which was not present in the prototype M1. This fluctuation comes from the differences in the strength of the side modes, whereas the total laser power had a smaller peak-to-peak variation of 1.8 dB.
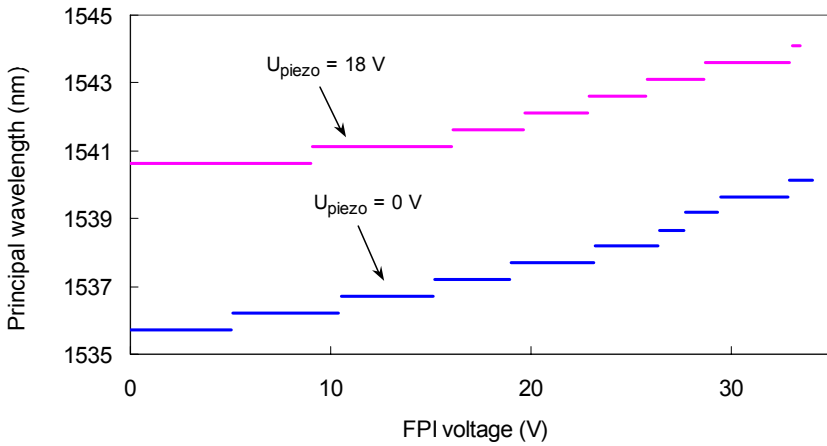
Figure 82. Principal wavelength of the prototype M2 in linear FPI-tuning.

The combined tuning range of the prototype M2 was 8 nm, in which three types of operation were observed. First, there were strongly lasing modes where the laser emission was quasi-single-mode with an SMSR of over 25 dB, Figure 84. These modes were similar to the modes of the prototype M1 in combined tuning. However, there were also intermediate modes that had an SMSR in the range of 10 to 20 dB and weak modes with very poor side mode suppression, which were not present in M1.
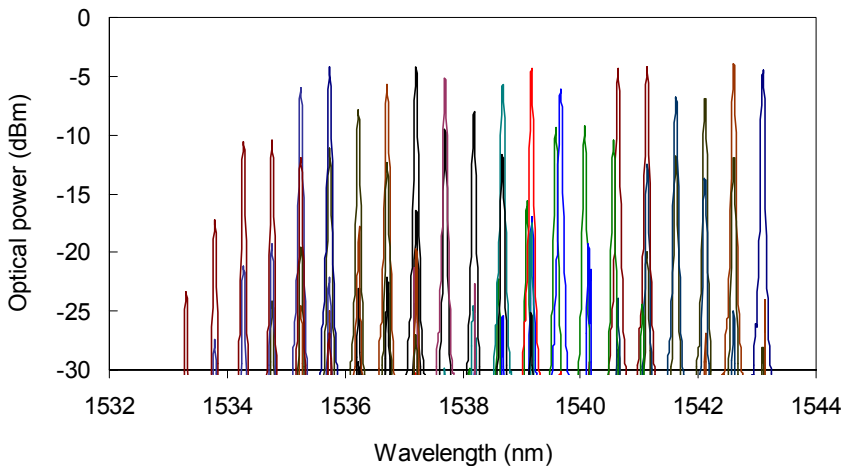
Figure 83. Superimposed spectra of the prototype M2 in combined tuning.
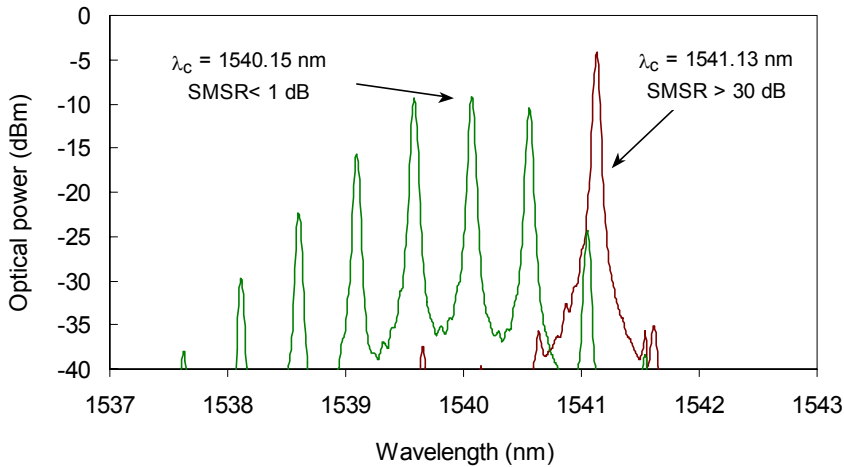
Figure 84. Quasi-single-mode and multimode spectra of the prototype M2 in combined tuning.

The weak modes were inherently insensitive to laser current or temperature changes. Although it was possible to fine-tune the wavelength of the weak modes by changing laser current or temperature, an optimum combination to obtain quasi-SM operation could not be found. The main characteristics of the prototype M2 are shown in Table 12.

The modulation characteristics of the prototype M2 were measured at Teleste Corp. in Turku using the measurement set-up schematically shown in Figure 85. The measurement equipment (HP E4400B and Rohde & Schwarz SMH signal generators, Teleste DVO 201 receiver and Rohde & Schwarz FSEA spectrum analyser) and procedures are routinely used at Teleste in the testing of the HFC network components.

In the small-signal amplitude response measurements the laser bias current was 75 mA and the optical modulation index (OMI) 10 %. The measured frequency response stayed rather flat from 300 kHz to 450 MHz and the 3-dB bandwidth was 620 MHz, Figure 86. There was a 1-dB depression around 360 MHz, which was also present when measuring the 1.31-μm fixed wavelength reference laser (LuminentOIC C-13-001A-P). Thus, the impedance matching circuit between the combiner and the tunable laser probably caused this dip. Laser current modulation raised the power of the side modes next to the principal mode about

2 dB. Otherwise the spectrum remained unchanged compared to the unmodulated operation.
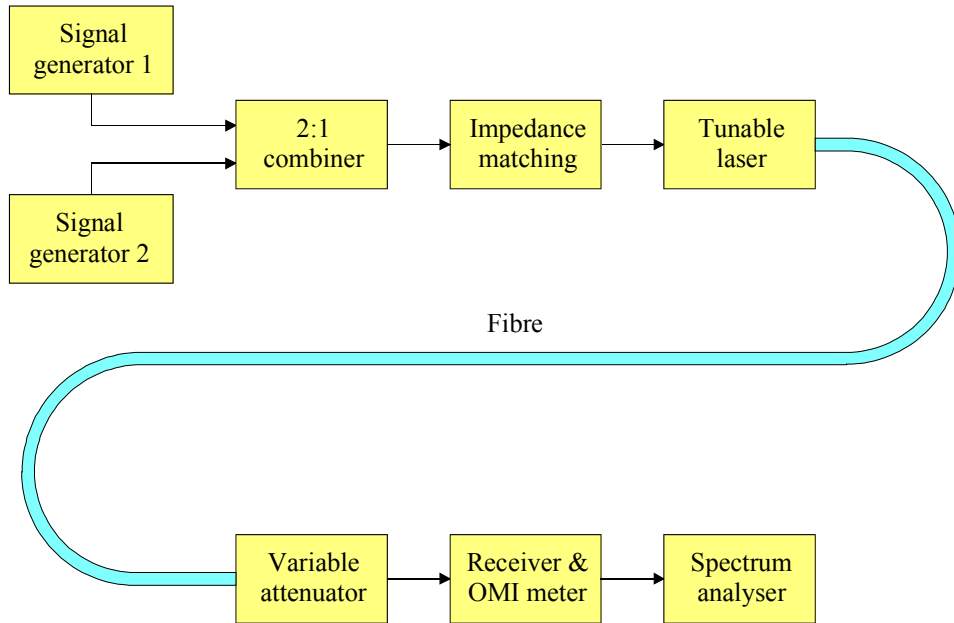
Figure 85. Schematic set-up of the modulation testing at Teleste Corp.

The second and third order distortion was measured using a bias current of 75 mA and modulation frequencies of f_1 = 32 MHz and f_2 = 22 MHz with an OMI of 10 % per channel. A 10-km long fibre spool was inserted between the pigtail of the prototype and the variable attenuator. The measured second order distortions were 47 dB ($f_1 + f_2$) and 46 dB ($f_1 - f_2$). The values are slightly higher than the 50-dB requirement set for the HFC uplink transmitters. The corresponding third order results were 67 dB ($2f_1 + f_2$), 64 dB ($2f_1 - f_2$), 64 dB ($2f_2 + f_1$) and 63 dB ($2f_2 - f_1$), when the requirement is 60 dB. The insertion of an optical isolator between the pigtail and the 10-km long fibre improved the third order distortion results from 3 to 8 dB, whereas the second order values did not change. The strength of the side modes (Figure 84) had no effect on the distortion results.

The carrier-to-noise ratio was measured at 31 MHz using a signal frequency of 32 MHz and a bandwidth of 4.75 MHz. The CNR with and without the 10-km

long fibre was 54 dB and 56 dB, respectively. Again the strength of the side modes had no effect on the results. The measured relative intensity noise (RIN) was comparable to commercial fixed wavelength DFB lasers.
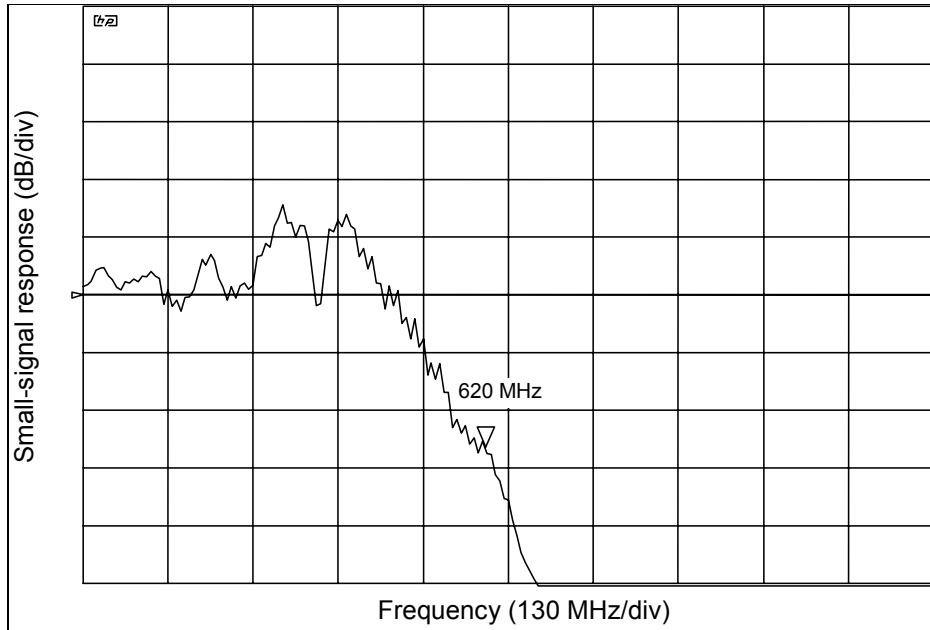
Figure 86. Frequency response of the prototype M2 (courtesy of Teleste Corp.).

6.2.5 Prototype M3

The piezo transducer of the prototype M3 did not operate properly and it was impossible to measure the piezo tuning characteristics. However, the potential tuning range was defined by changing the laser temperature by 0.5 °C so that the spectrum hopped from the upper end to the lower end. Then the maximum tuning range was from 1,531 to 1,550 nm – that is, 19 nm.

The linear FPI-tuning range using a zero piezo voltage was 9.3 nm, the average rms spectral width 1.4 nm and the mean output power 560 µW. Prototype M3 did not operate in the nonlinear FPI-tuning mode.

Because all the prototypes had a longer FPI-to-laser separation than the design value of 20 µm, verifying measurements were made using a separate laser and

FPI. The FPI was attached to the precision positioning device and brought near the AR coated facet of the laser III-2. The drive current and temperature of the laser were stabilised at 90 mA and 25 °C.

The minimum and maximum principal wavelength of the laser as the function of the FPI-to-laser separation is shown in Figure 87. The maximum tuning range at 10-µm separation was 45 nm when the FPI was non-operational and moved by the positioning device, and 20 nm when the FPI was kept stationary and tuned by its control voltage. Comparing the graphs with the performance of the prototypes, Table 12, shows that they are in fair unison.
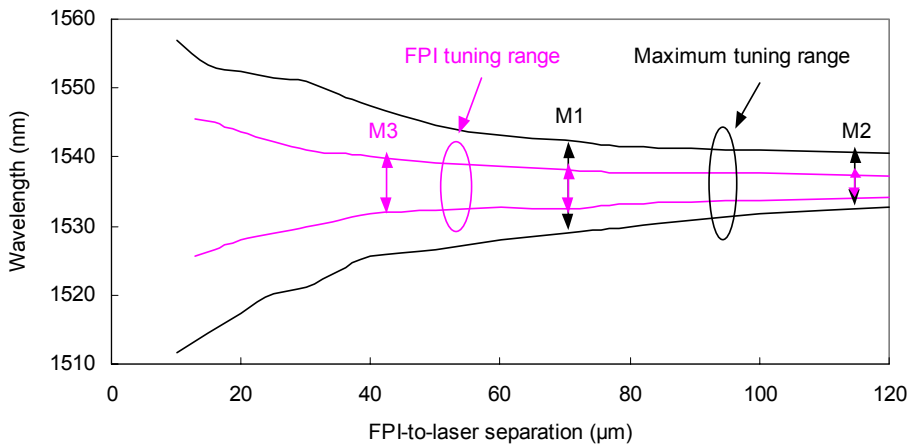
Figure 87. Minimum and maximum principal wavelength of the laser III-2 in the separate tuning experiment compared with the tuning range of the prototypes.

Table 12. Characteristics of the tunable laser prototypes.

Characteristics	M1	M2	M3
FPI-to-laser separation (µm)	75	115	42
Piezo tuning range (nm)	13	8	–
Linear FPI-tuning range (nm)	7	4	9
Nonlinear FPI-tuning range (nm)	2	–	–
Combined piezo and FPI tuning range (nm)	13	8	–
Rms spectral width in linear tuning (nm)	0.7	0.5	1.3
Average SMSR in combined tuning (dB)	26	14	–
Average output power (µW)	100	440	570

7. Discussion

This thesis clearly points out the challenges encountered when designing, assembling and testing novel tunable laser modules. First, a deep theoretical understanding of the laser physics and wavelength tuning mechanisms is essential. Without a reliable forecast of how the laser will operate and what its critical parameters are, neither proper module designs nor test procedures can be developed. The tunable laser model should predict the tuning range, laser spectrum and output power as the function of the tuning parameters and also define the critical tolerances of the components and their positions.

At present our tunable laser model is able to forecast the principal wavelength and output power characteristics, but it cannot predict the laser spectrum. When compared to the measurement results, the theory calculates the mode-hopping behaviour correctly. In addition, the simulated power values in the piezo tuning and in linear FPI-tuning are in fair correspondence to the measured ones. The simulated average output power from the HR coated laser facet at the 70-mA drive current was 4.4 mW. The measured SM fibre output powers of prototypes M2 and M3 at the same current were 0.3 mW and 0.4 mW, respectively. Considering that the realised laser-to-fibre coupling efficiency is about 10 %, the simulations seem to be able to predict the output power level. However, the simulated tuning range of 9 nm at 20-μm FPI-to-laser separation is clearly smaller than the measured 35-nm wavelength span.

The theory of the nonlinear tuning presented here is in strong conflict with the measurement results. None of the three prototypes behaved as predicted and the reason for this is not known. It seems that the model of the laser diode, and perhaps also the model of the FPI, is too simple and must be developed further.

Second, the assembly of single-mode fibre-coupled modules is demanding. Although the overall dimensions of the prototypes are macroscopic, about $2 \cdot 3 \cdot 6$ cm^3, the critical details are microscopic. For example, the target for the FPI-to-laser separation was 20 μm and the working distance of the wedge-ended fibres is only few micrometers. This means that both the module overview and the tiny details must be seen in the assembly. Additionally, it is difficult to simultaneously obtain a large magnification and a long depth of field due to optical fundamentals.

One of the challenges is the alignment of the vertically standing FPI device with the horizontal laser chip. There are six degrees of freedom – that is, three translations and three rotations – of which the FPI-to-laser separation and the pitch and yaw of the FPI are the most critical. For example, if the yaw angle is larger than 0.4°, it is impossible to bring the FPI sufficiently close to the laser. If the FPI leans towards the laser, the critical separation cannot be seen from above. Thus three microscopes must be used – one looking from above, the other from the side and the third having an adjustable field of view. Because of the need for several viewing angles, 3D mechanical design software is necessary and not only the principal components but also the electrical connections have to be included in the design; otherwise, one bonding wire can prevent seeing the critical spot from the crucial angle.

The fibre attachment trials indicate that it is possible to realise the laser-to-SM-fibre coupling using adhesive bonding. However, further studies are needed in order to improve the speed and repeatability of the process together with the reliability of the fibre attachment. If optical technologies are taken into extensive use in the access networks, the production quantities of the components must be high and the prices low. Because adhesive bonding is an economic process with low equipment investment, it has potential for these markets.

The wavelength tuning range of the prototypes was from 8 to 13 nm and output power between 100 and 570 µW. When the modules produce multimode spectra having an rms width of about 1 nm, the usable WDM channel number is low. However, the tests carried out using a separate FPI device down to a 10-µm separation from the laser chip produced a maximum tuning range of 45 nm, which covers the entire ITU C-band. If this tuning range can be exploited, and, at the same time, single-mode lasing obtained, the potential applications for our laser will increase substantially. The mode hopping behaviour is a handicap in spectroscopy, but it can be employed in WDM applications by adjusting the mode spacing equal to channel spacing – for example, to 100 GHz ITU grid.

The tests showed that the wavelength tuning is very sensitive to variations in the FPI-to-laser separation. When the separation changes about 0.8 µm the principal wavelength scans the entire tuning range. This means that with a 45-nm tuning span and 0.8-nm channel spacing, a 14-nm change in the FPI-to-laser separation produces a hop to the next channel. Therefore, the module structure must be

mechanically and thermally stable and the emission spectrum should be continuously monitored.

The output power of the prototypes is fairly low when compared with the total laser power of about 20 mW. The main reason for this is the tuning arrangement, where the output is taken from the HR coated laser facet that is inherently less powerful than the AR coated end. The output power can be somewhat increased by adjusting the laser facet reflectances.

The fibre-coupling efficiency of the solitary lasers was higher than the efficiency in the assembled prototypes. One possible explanation is that the FPI standing near the laser deteriorates the laser-to-fibre coupling. Assembling the laser chip active side down and inserting baffles that block the upper interfering beam can reduce this. In general, using more efficient coupling schemes than the butt joint, for example lensed fibres, increases the laser-to-fibre coupling efficiency. However, this will also tighten the fibre alignment tolerances.

We can compare the measured performance of the prototypes to the commercial products targeted to metro and long-haul telecommunications (Tables 2 and 3). Our modules offer a larger wavelength tuning range but lower output power than DFB lasers. Tunable DBR lasers and electrically pumped VCSELs have a wider tuning range, whereas their power levels are roughly equal to ours. External cavity lasers possess a much wider tuning range and higher output power, but they require external modulation. So, it seems that the main advantage of our modules compared to the competing technologies is the potentially low cost together with the possibility to use direct modulation up to 600 MHz.

When considering the production costs, the micromachined FPI device is one of the key components. Their uniformity was found to be rather poor – for instance, 30 % of the chips broke down before their passband reached the target value. In the operational components the control voltage for the 1,535-nm transmission peak varied from 28 to 42 V. Although silicon micromachining offers potentially low-cost components, the FPIs need development work before they can be applied in volume production. In addition, at present the maximum displacement of the moving mirror limits the FPI tuning range. Increasing the mirror movement to $\lambda/2$ would eliminate this limitation.

The tunable laser module would be more compact, if we could employ an electrostatically movable FPI, Figure 88. Here the voltage U_1 controls the transmittance band of the FPI that is comprised of two mirrors having reflectances of R_3 and R_4. This part of the device operates similarly to the FPIs used in the prototypes. The voltage U_2 adjusts the position of the FPI and replaces the present piezoelectric transducer. By simultaneously adjusting both voltages, single-mode operation could be obtained using just one electrically controlled and potentially inexpensive component.
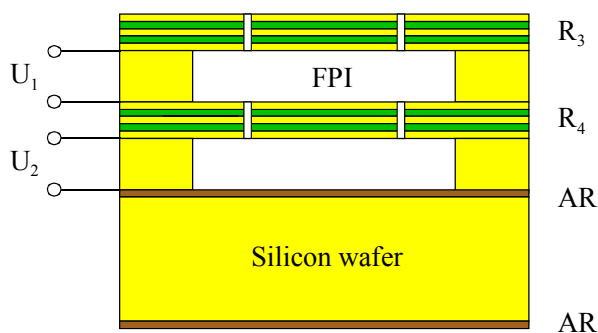
Figure 88. Schematic principle of the electrostatically movable FPI.

If we want to use tunable lasers in volume applications, such as the access networks, both the component and packaging costs of the module have to be very low. For example, the use of thermoelectric cooling should be avoided. This is problematic for the FPI-tuned laser that is very sensitive to variations in the FPI-to-laser separation. Because of this sensitivity, the operation wavelength and possibly the optical power must be monitored. The prototype measurements showed that laser monitoring through the FPI has some weaknesses. Therefore it seems wise to place the optical power and wavelength monitoring between the HR laser facet and the optical output fibre.

The operational and long-term reliability of the prototypes is not known. In principle, the FPI-tuned laser is an interferometer, which means that it is inherently very sensitive to any changes in the wavelength-tuning core. Thus, further studies are still needed to determine the true competence of our module.

8. Conclusions

The thesis introduces the design, assembly and testing of the wavelength tunable single-mode fibre-coupled laser modules. The short external cavity laser uses an electrically controlled silicon micromachined Fabry–Perot interferometer as the tuning element. The hybrid arrangement employs standard laser chips and therefore can provide a cost-effective solution for fibre optic communication and sensor applications.

The measured discontinuous tuning span of the prototypes ranged between 8 and 13 nm, and single-mode fibre output power was from 100 to 570 µW. The modules produced multimode tuning having an rms spectral width of about 1 nm. In addition, one prototype was capable of 13-nm single-mode tuning with a side mode suppression ratio of 26 dB. The modules can be electrically modulated and have a 3 dB bandwidth of over 600 MHz.

The test results show that the FPI-tuned lasers have potential for fibre optic communication applications where moderate performance suffices. The output power of the prototypes is fairly low due to the tuning arrangement, where the output is taken from the HR coated laser facet. In general, using more efficient coupling schemes than the butt joint, such as lensed fibres, increases the laser-to-fibre coupling efficiency and thereby the output power.

In volume applications, such as the access networks, both the component and packaging costs of module have to be very low. Therefore thermoelectric cooling should be avoided, which is problematic for the FPI-tuned laser that is very sensitive to variations in the FPI-to-laser separation. Because of this sensitivity, the operation wavelength and the optical power must be monitored.

At present the laser model is able to forecast the principal wavelength and output power characteristics, but it cannot predict the laser spectrum. The model of the laser diode, and perhaps the model of the FPI, are too simple and must be developed further. We should also improve the yield and reliability of the FPI devices and the fibre attachment process. In addition, the operational and long-term reliability of the module must be characterised, before we know the true competence of the FPI-tuned laser.

References

Abou-Zeid, A., Wiese, P. 1998. Interferometer with a wavelength-tuned diode laser for surface profilometry. Measurement Science and Technology, Vol. 9, pp. 1105–1110.

Ackerman, D.A., Johnson, J.E., Ketelsen, L.J-P., Geary, J.M., Asous, W.A., Walters, F.S., Freund, J.M., Hybertsen, M.S., Glogovsky, K.G., Lentz, C.W., Reynolds, C.L., Bylsma, R.B., Dean, E.J., Koch, T.L. 2001. Tunable semiconductor lasers for WDM telecommunications. IEEE Conference on Indium Phosphide and Related Materials. Pp. 571–574.

Adams, D.M., Gamache, C., Finlay, R., Cyr, M., Burt, K.M., Evans, J., Jamroz, E., Wallace, S., Woods, I., Doran, L., Ayliffe, P., Goodchild, D., Rogers, C. 2001. Module-packaged tunable laser and wavelength locker delivering 40 mW of fibre-coupled power on 34 channels. Electronics Letters, Vol. 37, No. 11, pp. 691–693.

ADC 2002. NYW-60-B Anywave tunable lasers. Product Information. 2 p.

Agere Systems 2002. C489-type 2.5 Gbits/s tunable, stabilized, metro-regional DBR laser transmitters. Preliminary Data Sheet, Rev. 2. 8 p.

Agility 2002. 3040 cw widely tunable laser assembly. Product Information. 2 p.

Aikio, J., Karioja, P. 1999. Wavelength tuning of a laser diode by using a micro-mechanical Fabry–Perot interferometer. IEEE Photonics Technology Letters, Vol. 11, No. 10, pp. 1220–1222.

Aikio, J., Sidorin, Y., Blomberg, M., Karioja, P. 1999. Wavelength tunable hybrid laser diode realized by using an electrostatically tuned silicon micromachined Fabry–Perot interferometer. Proceedings of SPIE, Vol. 3625, pp. 588–597.

Aikio, J.K., Kataja, K.J., Alajoki, T., Karioja, P., Howe, D.G. 2002. Extremely short external cavity lasers: the use of wavelength tuning effects in near field sensing. Proceedings of SPIE, Vol. 4640, pp. 235–245.

Aikio, J.K. 2004. Extremely short external cavity (ESEC) laser devices –
wavelength tuning and related optical characteristics. Doctoral thesis, University
of Oulu, Faculty of Science. In preparation.

Aizawa, T., Kamimoto, T., Tamaru, T. 1999. Measurements of OH radical
concentration in combustion environments by wavelength-modulation
spectroscopy with a 1.55-µm distributed-feedback diode laser. Applied Optics,
Vol. 38, No. 9, pp. 1733–1741.

Alcatel 2002. 1935 cw narrow band tunable laser. Product Information. 1 p.

Alder, T., Stöhr, A., Heinzelmann, R., Jäger, D. 2000. High-efficiency fiber-to-
chip coupling using low-loss tapered single-mode fiber. IEEE Photonics
Technology Letters, Vol. 12, No. 8, pp. 1016–1018.

Alferov, Zh.I., Ivanov, M.A., Il'in, Yu.V., Lyutetskiĭ, A.V., Pikhtin, N.A.,
Tarasov, I.S. 1995. Transverse mode selection in InGaAsP lasers with dielectric-
coated mirrors. Technical Physics Letters, Vol. 21, No. 3, pp. 195–197.

Amann, M-C., Schimpe R. 1990. Excess linewidth broadening in wavelength-
tunable laser diodes. Electronic Letters, Vol. 26, No. 5, pp. 279–280.

Amann, M-C., Buus, J. 1998. Tunable laser diodes. Boston: Artech House.
289 p. ISBN 0-89006-963-8

An, H.L. 2000. Theoretical investigation on the effective coupling from laser
diode to tapered lensed single-mode optical fiber. Optics Communications,
Vol. 181, pp. 89–95.

Annovazzi-Lodi, V., De-Donno, M., Donati, S., Zucchelli, L. 1997. Fabrication
of a wedge-shaped fiber endface by a self-centering technique. Journal of
Optical Communications, Vol. 18, pp. 1–3.

Aoki, Y., Kato, T., Mizuno, R.J., Iga, K. 1999. Micro-optical bench for
alignment-free optical coupling. Applied Optics, Vol. 38, No. 6, pp. 963–965.

Armiento, C.A., Tabasky, M., Jagannath, C., Fitzgerald, T.W., Shieh, C.L., Barry, V., Rothman, M., Negri, A., Haugsjaa, P.O., Lockwood, H.F. 1991. Passive coupling of InGaAsP/InP laser array and singlemode fibres using silicon waferboard. Electronics Letters, Vol. 27, No. 12, pp. 1109–1111.

Babinet, J. 1842. Note sur la transmission de la lumière par des canaux sinueux (Note on the transmission of light through winding channels). Comptes Rendus, Vol. 15, pp. 802. (In French)

Bachelot, R., Ecoffet, C., Deloeil, D., Royer, P., Lougnot, D-J. 2001. Integration of micrometer-sized polymer elements at the end of optical fibers by free-radical photopolymerization. Applied Optics, Vol. 40, No. 32, pp. 5860–5871.

Balnicki, A. 2001. Metro networks: the next killer app for DWDM. Lightwave, Vol. 18, No. 6, pp. 172–176.

Bandwidth9 2002. Tunable optical transmitters – MetroFlex™ G2 series. Preliminary Specifications. 2 p.

Berger, J.D., Zhang, Y., Grade, J.D., Lee, H., Hrinya, S., Jerman, H., Fennema, A., Tselikov, A., Anthon, D. 2001. Widely tunable external cavity diode laser using a MEMS electrostatic rotary actuator. ECOC 2001. Pp. 198–199.

Berry, R.W., Brace, D.J., Ravenscroft, I.A. 1978. Optical fiber system trials at 8 Mbits/s and 140 Mbits/s. IEEE Transactions on Communications, Vol. COM-26, No. 7, pp. 1020–1027.

Birks, T.A., Kenny, R.P., Oakley, K.P., Cryan, C.V. 1990. Elimination of water peak in optical fibre taper components. Electronics Letters, Vol. 26, No. 21, pp. 1761–1762.

Bludau, W., Rossberg, R.H. 1985. Low-loss laser-to-fiber coupling with negligible optical feedback. Journal of Lightwave Technology, Vol. LT-3, No. 2, pp. 294–302.

Blue Sky Research 2002. Programmable laser PRL 1550 series, C-band. Product Information. 3 p.

Bogatov, A.P., Eliseev, P.G., Ivanov, L.P., Logginov, A.S., Manko, M.A., Senatorov, K.Ya. 1973. Study of the single-mode injection laser. IEEE Journal of Quantum Electronics, Vol. QE-9, No. 2, pp. 392 – 394.

Bonenfant, P., Rodriguez Moral, A. 2002. Regional optical transport networks. Journal of Optical Networking, Vol. 1, No. 1, pp. 9–17.

Borella, M.S., Jue, J.P., Banerjee, D., Ramamurthy, B., Mukherjee, B. 1997. Optical components for WDM lightwave networks. Proceedings of the IEEE, Vol. 85, No. 8, pp. 1274–1307.

Boucart, J., Pathak, R., Zhang, D., Beaudoin, M., Kner, P., Sun. D., Stone, R.J., Nabiev, R.F., Yuen, W. 2003. Long wavelength MEMS tunable VCSEL with InP–InAlGaAs bottom DBR. IEEE Photonics Technology Letters, Vol. 15, No. 9, pp. 1186–1188.

Boudreau, R., Zhou, P., Bowen, T. 1998. Wafer scale photonic-die attachment. IEEE Transactions on Components, Packaging, and Manufacturing Technology – Part B, Vol. 21, No. 2, pp. 136–139.

Bozóki, Z., Sneider, J., Gingl, Z., Mohácsi, Á., Szakáll, M., Bor, Z., Szabó, G. 1999. A high-sensitivity, near-infrared tunable-diode-laser-based photoacoustic water-vapour-detection system for automated operation. Measurement Science and Technology, Vol. 10, pp. 999–1003.

Breedis, J.B. 2001. Monte Carlo tolerance analysis of a passively aligned silicon waferboard package. Proceedings of 51st Electronic Components and Technology Conference, Orlando, FL., USA, 29 May – 1 June 2001, pp. 247–254.

Bruce, E. 2002. Tunable lasers. IEEE Spectrum, Vol. 39, No. 3, pp. 35–39.

Cassidy, D.T., Bruce, D.M., Ventrudo, B.F. 1991. Short-external-cavity module for enhanced single-mode tuning of InGaAsP and AlGaAs semiconductor diode lasers. Review of Scientific Instruments, Vol. 62, No. 10, pp. 2385–2388.

Chan, C.C., Jin, W., Ho, H.L., Wang, D.N, Wang, Y. 2001. Improvement of measurement accuracy of fibre Bragg grating sensor systems by use of gas absorption lines as multi-wavelength references. Electronics Letters, Vol. 37, No. 12, pp. 742–743.

Chanclou, P., Thual, M., Lostec, J., Auvray, P., Caulet, J., Joulié, G., Poudoulec, A., Clavel, B. 1998. Highly efficient collective coupling between laser diode array and lensed fiber ribbon. Electronics Letters, Vol. 34, No. 3, pp. 273–274.

Charlet, G., Lanne, S., Pierre, L., Simonneau, C., Tran, P., Mardoyan, H., Brindel, P., Gorlier, M., Antona, J-C., Molina, M., Sillard, P., Godin, J., Idler, W., Bigo, S. 2003. Cost-optimized 6.3 Tbit/s-capacity terrestrial link over 17×100km using phase-shaped binary transmission in a conventional all-EDFA SMF-based system. OFC 2003. Pp. PD25-1 – PD25-3.

Chen, W.T., Wang, L.A. 2000. Laser-to-fiber coupling scheme by utilizing a lensed fiber integrated with a long-period fiber grating. IEEE Photonics Technology Letters, Vol. 12, No. 5, pp. 501–503.

Cheng, W-H., Sheen, M-T., Wang, G-L., Wang, S-C., Kuang, J-H. 2001. Fiber alignment shift formation mechanisms of fiber-solder-ferrule joints in laser module packaging. Journal of Lightwave Technology, Vol. 19, No. 8, pp. 1177–1184.

Cohen, L.G., Schneider, M.V. 1974. Microlenses for coupling junction lasers to optical fibers. Applied Optics, Vol. 13, No. 1, pp. 89–94.

Cohen, M.S., Cina, M.F., Bassous, E., Oprysko, M.M., Speidell, J.L. 1991. Passive laser-fiber alignment by index method. IEEE Photonics Technology Letters, Vol. 3, No. 11, pp. 985–987.

Cohen, D.A., Skogen, E.J., Marchand, H., Coldren, L.A. 2001. Monolithic chemical sensor using heterodyned sampled grating DBR lasers. Electronics Letters, Vol. 37, No. 22, pp. 1358–1360.

Coldren, L.A., Corzine, S.W. 1995. Diode lasers and photonic integrated circuits. New York: John Wiley & Sons. 594 p. ISBN 0-471-11875-3

Coldren, L.A., Fish, G.A., Akulova, Y., Barton, J.S., Johansson, L., Coldren, C.W. 2004. Tunable semiconductor lasers: a tutorial. Journal of Lightwave Technology, Vol. 22, No. 1, pp. 193–202.

Colladon, D. 1842. Sur les réflexions d'un rayon de lumière à l'intérieur d'une veine liquide parabolique. (On the reflection of a light beam inside a parabolic liquid vein). Comptes Rendus, Vol. 15, pp. 800–802. (In French)

Corning 2002. SMF-28™ optical fiber. Product Information. 4 p.

Cox, W.R., Chen, T., Ussery, D., Hayes, D.J., Tatum, J.A., MacFarlane, D.L. 1996. Microjetted lenslet triplet fibers. Optics Communications, Vol. 123, pp. 492–496.

Daniel, R.G., McNesby, K.L., Miziolek, A.W. 1996. Application of tunable diode laser diagnostics for temperature and species concentration profiles of inhibited low-pressure flames. Applied Optics, Vol. 35, No. 21, pp. 4018–4025.

Datta, M., Hu, Z., Dagenais, M. 2003. A novel method for fabrication of a hybrid optoelectronic packaging platform utilizing passive-active alignment. IEEE Photonics Technology Letters, Vol. 15, No. 2, pp. 299–301.

Datta, M., Dagenais, M. 2003. High coupling efficiency actively aligned laser modules using micro-heaters and pre-compensation. Proceedings of 53rd Electronic Components and Technology Conference, New Orleans, LA., USA, 27–30 May 2003. Pp. 1312–1317.

Dautartas, M.F., Fisher, J., Luo, H., Datta, P., Jeantilus, A. 2002. Hybrid optical packaging, challenges and opportunities. Proceedings of 52th Electronic Components and Technology Conference, San Diego, CA., USA, 28–31 May 2002. Pp. 787–793.

Day, T. 2001. External-cavity tunable diode lasers for network deployment. OFC 2001. Pp. TuJ4-1–TuJ4-3.

Day, T., Thompson, C., and Lee, J. 2002. Widely tunable laser technologies: meeting the need of tomorrow's networks. Proceedings of SPIE, Vol. 4652, pp. 186–196.

Delorme, F. 1998. Widely tunable 1.55-µm lasers for wavelength-division-multiplexed optical fiber communications. IEEE Journal of Quantum Electronics, Vol. 34, No. 9, pp. 1706–1716.

Dowd, P., Johnson, S.R., Feld, S.A., Adamcyk, M., Chaparro, S.A., Joseph, J., Hilgers, K., Horning, M.P., Shiralagi, K., Zhang, Y-H. 2003. Long wavelength GaAsP/GaAs/GaAsSb VCSELs on GaAs substrates for communication applications. Electronics Letters, Vol. 39, No. 13, pp. 987–988.

Duarte, F.J. (ed.). 1995. Tunable lasers handbook. San Diego, CA: Academic Press. 476 p. ISBN 0-12-222695-X

Edwards, C.A., Presby, H.M., Dragone, C. 1993. Ideal microlenses for laser to fiber coupling. Journal of Lightwave Technology, Vol. 11, No. 2, pp. 252–257.

Edwards, C.S., Barwood, G.P., Bell, S.A., Gill, P., Stevens, M. 2001. A tunable diode laser absorption spectrometer for moisture measurements in the low parts in 10^9 range. Measurement Science and Technology, Vol. 12, pp. 1214–1218.

Eisenstein, G., Vitello, D. 1982. Chemically etched conical microlenses for coupling single-mode lasers into single-mode fibers. Applied Optics, Vol. 21, No. 19, pp. 3470–3474.

Enochs, S. 1987. Opto-mechanical stability of a laser-diode module with soldered fiber. Proceedings of 7th Annual International Electronics Packaging Conference, Boston, MA., USA, November 1987. Pp. 799–804.

Enochs, S. 1989. Optomechanical packaging for extended temperature performance. Proceedings of SPIE, Vol. 1043, pp. 338–343.

Flanagan, C., Trask, S., Heyler, R. 2003. Direct-coupling retention using laser soldering: technical and economic benefits. Proceedings of 53rd Electronic Components and Technology Conference, New Orleans, LA., USA, 27–30 May 2003. Pp. 1308–1311.

Fu, Y., Bryan, N.K.A., Shing, O.N. 2000. Integrated micro-cylindrical lens with laser diode for single-mode fiber coupling. IEEE Photonics Technology Letters, Vol. 12, No. 9, pp. 1213–1215.

Fujitsu 2000. FLD5F6CA Tunable LD module with wavelocker for long haul and metropolitan DWDM applications. Product Information. 2 p.

Fuller, M. 2001. Infant tunable-laser market has promising future. Lightwave, Vol. 18, No. 8, pp. 187–198.

Galarza, M, De Mesel, K., Verstuyft, S., Aramburu, C., Moerman, I., Van Daele, P., Baets, R., López-Amo, M. 2002. 1.55-μm InP-InGaAsP Fabry-Pérot lasers with integrated spot size converters using antiresonant reflecting optical waveguides. IEEE Photonics Technology Letters, Vol. 14, No. 8, pp. 1043–1045.

Ghafouri-Shiraz, H, Aruga, T. 1996. Improvement of coupling efficiency between a 0.82 μm wavelength laser diode and a VAD single-mode fibre by conical microlenses. Opto & Laser Technology, Vol. 28, No. 5, pp. 367–371.

Gnauck, A.H., Raybon, G., Chandrasekhar, S., Leuthold, J., Doerr, C., Stulz, L., Agarwal, A., Banerjee, S., Grosz, D., Hunsche, S., Kung, A., Marhelyuk, A., Maywar, D., Movassaghi, M., Liu, X., Xu, C., Wei, X., Gill, D.M. 2002. 2.5 Tb/s (64×42.7 Gb/s) transmission over 40×100 km NZDSF using RZ-DPSK format and all-Raman-amplified spans. OFC 2002. Pp. FC2-1–FC2-3.

Golikova, E.G., Gorbylev, V.A., Il'in, Yu.V., Kureshov, V.A., Leshko, A.Yu., Lyutetskiĭ, A.V., Pikhtin, N.A., Ryaboshtan, Yu.A., Simakov, V.A., Tarasov, I.S., Tret'yakova, E.A., Fetisova, N.V. 2000. Mesastripe single-mode separately bounded lasers based on InGaAsP/InP heterostructures obtained by VPE of organometallic compounds. Technical Physics Letters, Vol. 26, No. 4, pp. 295–297.

Goralski, W. 2001. Optical networking & WDM. Berkeley, CA: Osborne/ McGraw-Hill. 556 p. ISBN 0-07-213078-4

Halbritter, H., Riemenschneider, F., Jacquet, J., Provost, J-G., Sagnes, I., Meissner, P. 2004. AM and RIN of a tunable optically pumped 1.6-μm VCSEL. IEEE Photonics Technology Letters, Vol. 16, No. 3, pp. 723–725.

Hall, R.N., Fenner, G.E., Kingsley, J.D., Soltys, T.J., Carlson, R.O. 1962. Coherent light emission from GaAs junctions. Physical Review Letters, Vol. 9, No. 9, pp. 366–368.

Harroff, E. 2001. KPNQwest 'rings out' broadband capacity. Lightwave, Vol. 18, No. 10, pp. 1–54.

Hayashi, I., Panish, M.B., Foy, P.W., Sumski, S. 1970. Junction lasers which operate continuously at room temperature. Applied Physics Letters, Vol. 17, No. 3, pp. 109–111.

Hecht, E. 1990. Optics. 2nd ed. Reading, MA: Addison–Wesley. 676 p. ISBN 0-201-11609-X

Hecht, J. 1999a. City of light: the story of fiber optics. New York: Oxford University Press. 316 p. ISBN 0-19-510818-3

Hecht, J. 1999b. Understanding fiber optics. 3rd ed. Upper Saddle River, NJ: Prentice Hall. 617 p. ISBN 0-13-956145-5

Hecht, J. 2002. Transmission at 40 Gbit/s requires taming tough technical problems. Laser Focus World, Vol. 38, No. 2, pp. 87–93.

Heikkinen, V., Tukkiniemi, K., Vähäkangas, J., Hannula, T. 1991. Packaging considerations of fiber optic laser sources. Proceedings of SPIE, Vol. 1533, pp. 115–121.

Heikkinen, V., Aikio, J., Alajoki, T., Hiltunen, J., Mattila, A-J., Ollila, J., Karioja, P. 2004. Single-mode tuning of a 1540-nm diode laser using a Fabry−Perot interferometer. IEEE Photonics Technology Letters, Vol. 16, No. 4, pp. 1164–1166.

Henry, C.H., Kazarinov, R.F. 1986. Instability of semiconductor lasers due to optical feedback from distant reflectors. IEEE Journal of Quantum Electronics, Vol. QE-22, No. 2, pp. 294–301.

Hinkley, E.D., Kelley, P.L. 1971. Detection of air pollutants with tunable diode lasers. Science, Vol. 171, No. 3972, pp. 635 – 639.

Holman, J.P. 1997. Heat transfer. 8th ed. New York: McGraw–Hill. 696 p. ISBN 0-07-114320-3

Hsieh, J.J., Shen, C.C. 1977. Room-temperature cw operation of buried-stripe double-heterostructure GaInAsP/InP diode lasers. Applied Physics Letters, Vol. 30, No. 8, pp. 429–431.

Hunziker, W., Bolz, E., Melchior, H. 1992. Elliptically lensed polarisation maintaining fibers. Electronics Letters, Vol. 28, No. 17, pp. 1654–1656.

Hübner, B., Vollrath, G., Ries, R., Gréus, C., Janning, H., Rönneberg, E., Kuphal, E., Kempf, B., Göbel, R., Fiedler, F., Zengerle, R., Burkhard, H. 1997. Laser diodes with integrated spot-size transformer as low-cost optical transmitter elements for telecommunications. IEEE Journal of Selected Topics in Quantum Electronics, Vol. 3, No. 6, pp. 1372–1383.

Iiyama, K., Maeda, T., Takamiya, S. 2000. Phase-decorrelated FMCW reflectometry for long optical fiber characterization by using a laser diode with modulated external-cavity. IEICE Transactions on Electronics, Vol. E83-C, No. 3, pp. 428–434.

Iolon 2002. Apollo™ tunable laser. Product Information. 2 p.

Iseki, T., Tai, H., Kimura, K. 2000. A portable remote methane sensor using a tunable diode laser. Measurement Science and Technology, Vol. 11, pp. 594–602.

ITU – T Recommendation G.692. 1998. Optical interfaces for multi-channel systems with optical amplifiers. Geneva: International Telecommunication Union. 31 p.

ITU – T Recommendation G.694.1 2002. Spectral grids for WDM applications: DWDM frequency grid. Geneva: International Telecommunication Union. 5 p.

ITU – T Recommendation G.694.2 2003. Spectral grids for WDM applications: CWDM wavelength grid. Geneva: International Telecommunication Union. 4 p.

JDS Uniphase 2002. Temperature tunable 10 mW WDM laser for direct modulation in links up to 180 km CQF413/608 series. Product Bulletin. 5 p.

Jeon, H., Verdiell, J-M., Ziari, M., Mathur, A. 1997. High-power low-divergence semiconductor lasers for GaAs-based 980-nm and InP-based 1550-nm applications. IEEE Journal of Selected Topics in Quantum Electronics, Vol. 3, No. 6, pp. 1344–1350.

Jiang, M., Lu, C-C., Chen, P., Zhou, J-H., Cai, J., McCallion, K., Knopp, K.J., Wang, P.D., Azimi, M., Vakhshoori, D. 2001. Error free 2.5 Gb/s transmission over 125 km conventional fiber of a directly modulated widely tunable vertical cavity surface emitting laser. OFC 2001. Pp. TuJ3-1–TuJ3-3.

Jones, M.W., Kao, K.C. 1969. Spectrophotometric studies of ultra low loss optical glasses II: double beam method. Journal of Scientific Instruments (Journal of Physics E), Vol. 2, pp. 331–335.

Joyce, W.B., DeLoach, B.C. 1984. Alignment of Gaussian beams. Applied Optics, Vol. 23, No. 23, pp. 4187–4196.

Järvenpää, P. 2001. DXO100 – a reliable solution for expanding your network. Teleste News & Views, No. 2, p. 14.

Kallimani, K.I., O'Mahony, M.J. 1998. Relative intensity noise for laser diodes with arbitrary amounts of optical feedback. IEEE Journal of Quantum Electronics, Vol. 34, No. 8, pp. 1438–1446.

Kalonji, N., Semo, J. 1994. High efficiency, long working distance laser diode to singlemode fibre coupling arrangement. Electronics Letters, Vol. 30, No. 11, pp. 892–894.

Kao, K.C., Hockham, G.A. 1966. Dielectric-fibre surface waveguides for optical frequencies. Proceedings of the IEEE, Vol. 133, No. 7, pp. 1151–1158.

Kapron, F.P., Keck, D.B., Maurer, R.D. 1970. Radiation losses in glass optical waveguides. Applied Physics Letters, Vol. 17, No. 10, pp. 423–425.

Karioja, P., Nousiainen, S., Hannula, T. 1989. The feasibility of an intra-machine fiber optic communication network. Proceedings of EFOC/LAN 89, Amsterdam, 12–16 June 1989. Pp. 76–80.

Karioja, P., Tammela, S., Tervonen, A., Honkanen, S., 1995. Passive fiber optic bus using bidirectional integrated optic buss access couplers. Optical Engineering, Vol. 34, No. 9, pp. 2551–2559.

Karioja, P., Ollila, J., Putila, V-P., Keränen, K., Häkkilä, J., Kopola, H. 2000. Comparison of active and passive fiber alignment techniques for multi-mode laser pigtailing. Proceedings of 50th Electronic Components and Technology Conference, Las Vegas, USA, 21–24 May 2000. Pp. 244–249.

Karstensen, H. 1988. Laser diode to single-mode fiber coupling with ball lenses. Journal of Optical Communications, Vol. 9, No. 2, pp. 42–49.

Kartalopoulos, S.V. 2000. Introduction to DWDM technology: data in a rainbow. New York: IEEE Press. 258 p. ISBN 0-7803-5399-4

Kato, D. 1973. Light coupling from a stripe-geometry GaAs diode laser into an optical fiber with spherical end. Journal of Applied Physics, Vol. 44, No. 6, pp. 2756–2758.

Kato, K., Nishi, I. 1990. Low-loss laser diode module using a molded aspheric glass lens. IEEE Photonics Technology Letters, Vol. 2, No. 7, pp. 473–474.

Kawano, K., Mitomi, O., Yanagibashi, M., Nozawa, T. 1989. Efficient highly stable laser diode module for single-mode fiber employing a combination of hemispherical ended GRIN rod lens and virtual fiber. Applied Optics, Vol. 28, No. 11, pp. 2012–2016.

Keck, D.B., Maurer, R.D., Schultz, P.C. 1973. On the ultimate lower limit of attenuation in glass optical waveguides. Applied Physics Letters, Vol. 22, No. 7, pp. 307–309.

Kim, J-M., Yasuda, K, Shin, Y-E., Fujimoto, K. 2002. 3-D highly precise self-alignment process using surface tension of liquid resin material. IEICE Transactions on Electronics, Vol. E85-C, No. 7, pp. 1491–1498.

Kner, P., Kageyama, T., Boucart, J., Stone, R., Sun. D., Nabiev, R.F., Pathak, R., Yuen, W. 2003. A long-wavelength MEMS tunable VCSEL incorporating a tunnel junction. IEEE Photonics Technology Letters, Vol. 15, No. 9, pp. 1183–1185.

Knopp, K.J., Vakhshoori, D., Wang, P.D., Azimi, M., Jiang, M., Chen, P., Matsui, Y., McCallion, K., Baliga, A., Sakhitab, F., Letsch, M., Johnson, B., Huang, R., Jean, A., DeLargy, B., Pinzone, C., Fan, F., Liu, J., Lu, C., Zhou, J., Zhu, H., Gurjar, R., Tayebati, P., MacDaniel, D., Baorui, R., Waterson, R., VanderRhodes, G. 2001. High power MEMS-tunable vertical-cavity surface-emitting lasers. Digest of the LEOS Summer Topical Meetings, paper TuA1.3. 2 p.

Kobayashi, K., Mito, I. 1988. Single frequency and tunable laser diodes. Journal of Lightwave Technology, Vol. 6, No. 11, pp. 1623–1633.

Kondo, K. 1991. Butterfly-type semiconductor laser diode modules. Anritsu Technical Review, No. 14, pp. 4–11. ISSN 0914-7195

Koplow, J.P., Kliner, D.A.V., Goldberg, L. 1998. Development of a narrow-band, tunable, frequency-quadrupled diode laser for UV absorption spectroscopy. Applied Optics, Vol. 37, No. 18, pp. 3954–3960.

Korotky, S.K., Gnauck, A.H., Kasper, B.L., Campbell, J.C., Veselka, J.J., Talman, J.R., McCormick, A.R. 1987. 8 Gbit/s transmission experiment over 68 km of optical fiber using a Ti:LiNbO$_3$ external modulator. Journal of Lightwave Technology, Vol. LT-5, No. 10, pp. 1505–1509.

Kuang, J-H., Sheen, M-T., Wang, S-C., Chen, C-H., Cheng, W-H. 1999. Crack formation mechanism in laser-welded Au-coated invar materials for semiconductor laser packaging. IEEE Transactions on Advanced Packaging, Vol. 22, No. 1, pp. 94–100.

Kuang, J-H., Sheen, M-T., Wang, S-C., Wang, G-L., Cheng, W-H. 2001. Post-weld-shift in dual-in-line laser package. IEEE Transactions on Advanced Packaging, Vol. 24, No. 1, pp. 81–85.

Laude, J-P. 2002. DWDM fundamentals, components, and applications. Boston: Artech House. 282 p. ISBN 1-58053-177-6

Li, T-N., Freude, W. 1991. Taper coupling of laser diode to singlemode fibre: influence of fibre field shape. Electronics Letters, Vol. 27, No. 13, pp. 1202–1203.

Li, G.S., Nabiev, R.F., Yuen, W., Jansen, M., Davis, D., Chang-Hasnain, C.J. 2001. Electrically-pumped directly-modulated tunable VCSEL for metro DWDM applications. ECOC 2001. Pp. 220–221.

Lin, C-F., Su, Y-S., Wu, B-R. 2002a. External-cavity semiconductor laser tunable from 1.3 to 1.54 μm for optical communication. IEEE Photonics Technology Letters, Vol. 14, No. 1, pp. 3–5.

Lin, Y., Liu, W., Shi, F.G. 2002b. Laser welding induced alignment distortion in butterfly laser module packages: effect of welding sequence. IEEE Transactions on Advanced Packaging, Vol. 25, No. 1, pp. 73–78.

Lin, Y., Liu, W., Shi, F.G. 2002c. Adhesive joint design for high yield & low cost assembly of fiberoptic devices. Proceedings of 52th Electronic Components and Technology Conference, San Diego, CA., USA, 28–31 May 2002. Pp. 662–666.

Linke, R.A. 1984. Direct gigabit modulation of injection lasers − structure-dependent speed limitations. Journal of Lightwave Technology, Vol. LT-2, No. 1, pp. 40–43.

Liu, A.Q., Zhang, X.M., Murukeshan, V.M., Lam, Y.L. 2001. A novel integrated micromachined tunable laser using polysilicon 3-D mirror. IEEE Photonics Technology Letters, Vol. 13, No. 5, pp. 427–429.

Liu, A.Q., Zhang, X.M., Murukeshan, V.M., Lu, C., Cheng, T.H. 2002. Micromachined wavelength tunable laser with an extended feedback model. IEEE Journal on Selected Topics in Quantum Electronics, Vol. 8, No. 1, pp. 73–79.

Lübken, F-J., Dingler, F., von Lucke, H., Anders, J., Riedel, W.J., Wolf, H. 1999. MASERATI: a rocketborne tunable diode laser absorption spectrometer. Applied Optics, Vol. 38, No. 25, pp. 5338–5349.

Maiman, T.H. 1960. Stimulated optical radiation in ruby. Nature, Vol. 187, pp. 493–494.

Mandell, M. 2000. 120 000 leagues under the sea. IEEE Spectrum, Vol. 37, No. 4, pp. 50–54.

Marciante, J.R., van Tartwijk, G.H.M., Agrawal, G.P. 1997. Spatial feedback effects in narrow-stripe index-guided semiconductor lasers. IEEE Journal of Quantum Electronics, Vol. 33, No. 3, pp. 469–473.

Marshall, I.W. 1986. Low loss coupling between semiconductor lasers and single-mode fibre using tapered lensed fibres. British Telecom Technology Journal, Vol. 4, No. 2, pp. 114–121.

Mason, B., Barton, J., Fish, G.A., Coldren, L.A., DenBaars, S.P. 2000. Design of sampled grating DBR lasers with integrated semiconductor optical amplifiers. IEEE Photonics Technology Letters, Vol. 12, No. 7, pp. 7672–764.

Matthews, M.B., Macdonald, B.M. Preston, K.R. 1990. Optical components – the new challenge in packaging. IEEE Transactions on Components, Hybrids, and Manufacturing Technology, Vol. 13, No. 4, pp. 798–806.

Mears, R.J., Reekie, L., Jauncey, I.M., Payne, D.N. 1987. Low-noise erbium-doped fibre amplifier operating at 1.54 µm. Electronics Letters, Vol. 23, pp. 1026–1028.

Mickelson, A.R., Basavanhally, N.R., Lee, Y-C. (eds.). 1997. Optoelectronic packaging. New York: Wiley-Interscience. 261 p. ISBN 0-471-11188-0

Miller, C., Li, T., Miller, J., Bao, F., Hsu, K. 1998. Multiplexed fiber gratings enhance mechanical sensing. Laser Focus World, Vol. 34, No. 3, pp. 119–123.

Miyata, H., Kaito, Y., Kai, Y., Onaka, H., Nakazawa, T., Doi, M., Seino, M., Chikama, T., Kotaki, Y., Wakao, K., Komiyama, M., Kunikane, T., Yonetani, H., Sakai, Y. 2000. Fully dynamic and reconfigurable optical add/drop multiplexer on 0.8 nm channel spacing using AOTF and 32-wave tunable LD module. OFC 2000, Vol. 4. Pp. 287–289.

Modavis, R.A., Webb, T.W. 1995. Anamorphic microlens for laser diode to single-mode fiber coupling. IEEE Photonics Technology Letters, Vol. 7, No. 7, pp. 798–800.

Moerman, I., Van Daele, P.P., Demeester, P.M. 1997. A review on fabrication technologies for the monolithic integration of tapers with III-V semiconductor devices. IEEE Journal of Selected Topics in Quantum Electronics, Vol. 3, No. 6, pp. 1308–1320.

Mondal, S.K., Shi, F.G. 2001. Novel lensed-fiber offset coupling scheme to reduce reflected intensity noise in optimizing carrier-to-noise ratio. Optics Communications, Vol. 199, pp. 399–405.

Morimoto, T., Yashiki, K., Kudo, K., Sasaki, T. 2002. Wavelength-selectable microarray light sources for DWDM photonic networks. IEICE Transactions on Electronics, Vol. E85-C, No. 4, pp. 982–989.

Morris, A.S. 2001. In search of transparent networks. IEEE Spectrum, Vol. 38, No. 10, pp. 47–51.

Multiplex 2002. MTX-TEML Multi-channel tunable transmitter with integrated electro-absorption modulator. Preliminary Data Sheet. 4 p.

Murata, N., Nishi, S., Hosono, S. 1996. UV-curable transparent adhesives for fabricating precision optical components. Journal of Adhesion, Vol. 59, pp. 39–50.

Murata, N. 1998. Adhesives for optical devices. Proceedings of 48th Electronic Components and Technology Conference, Settle, WA., USA, 25–28 May 1998. Pp. 1178–1185.

Nangalia, S., Koopman, N., Rogers, V., Beranek, M.W., Hager, H.E., Ledbury, E.A., Loebs, V.A., Miao, E.C., Tang, C.H., Pico, C.A., Swenson, E.J., Hatzis, D., Li, P., Luck, C. 1997. Fluxless, no clean assembly of optoelectronic devices with PADS. Proceedings of 47th Electronic Components and Technology Conference, 18–21 May 1997, San Jose, CA., USA. Pp. 755–762.

NEMI 2002. 2002 NEMI roadmap – Optoelectronics. National Electronics Manufacturing Initiative, Inc., Herndon, VA, USA.
http://www.nemi.org/roadmapping/status.html

New Focus 2001. TLS 420C Widely tunable laser subsystem for optical networks. Product Information. 4 p.

Newton 2001. New widely tunable lasers for optical networks. Internet document, available at http://www.intec.rug.ac.be/newton/. 7 p.

Nortel Networks 2001. ML-20 Tunable VCSEL. Preliminary Datasheet. 4 p.

Nortel Networks 2002a. LCW508ET Tunable DFB laser – 8 channel. Preliminary Datasheet. 4 p.

Nortel Networks 2002b. LG10M 10 Gb/s GaAs MZ modulator with tunable VCSEL. Preliminary Datasheet. 5 p.

Norton, P., Chia, P., Braggins, T., Levinstein, H. 1971. Extended wavelength tuning of $Pb_{1-x}Sn_xTe$ lasers. Applied Physics Letters, Vol. 18, No. 4, pp. 158–159.

Nöding, M. and Amann, M-C. 1998. FMCW-lidar with widely tunable laser diodes: influence of the tuning behaviour on the distance measurement. Journal of Optics, Vol. 29, pp. 212–215.

Ogura, A., Kuchiki, S., Shiraishi, K., Ohta, K., Oishi, I. 2001. Efficient coupling between laser diodes with a highly elliptic field and single-mode fibers by means of GIO fibers. IEEE Photonics Technology Letters, Vol. 13, No. 11, pp. 1191–1193.

Okiyama, T., Nishimoto, H., Yokota, I., Touge, T. 1988. Evaluation of 4-Gbit/s optical fiber transmission distance with direct and external modulation. Journal of Lightwave Technology, Vol. 6, No. 11, pp. 1686–1692.

Ovadia, S. 2001. Broadband cable TV access networks: from technologies to applications. Upper Saddle River, NJ: Prentice Hall. 464 p. ISBN 0-13-086421-8

Pat. US 4,329,190. 1982. Process for attaching optical fiber to semiconductor die. Motorola, Inc. (Berg, H.M., Lewis, G.L.). Appl. No. 45,903, 6 June 1979. 11 May 1982. 4 p.

Pat. US 5,048,919. 1991. Low-stress coupling of electrooptical device to optical fiber. Bell Communications Research, Inc. (Ladany, I.). Appl. No. 593,787, 5 October 1990. 17 September 1991. 6 p.

Pat. US 5,311,610. 1994. Low-stress coupling of electrooptical device to optical fiber. Bell Communications Research, Inc. (Ladany, I., Reith, L.A.). Appl. No. 41,027, 31 March 1993. 10 May 1994. 8 p.

Pat. US 5,561,523. 1996. Electrically tunable Fabry–Perot interferometer produced by surface micromechanical techniques for use in optical material analysis. Vaisala Oy (FI). (Blomberg, M., Orpana, M. & Lehto, A.). Appl. No. 386,773, 10 February 1995. 1 October 1996. 9 p.

Pat. US 6,192,059. 2001. Wavelength-tunable laser configuration. Valtion Teknillinen Tutkimuskeskus (FI) & Board of Regents on Behalf of Optical Sciences Center (US). (Karioja, P & Sidorin, Y.). Appl. No. 09/293,064, 16 April 1999. 20 February 2001. 9 p.

Pat. WO 02052324. 2002. Process for coupling optical elements to optoelectronic devices. Emcore Corp. (Anderson, G.R., Armendariz, M.G., Bryan, R.P., Carson, R.F., Chu, D., Duckett, E.B. III, Giunta, R.K., Mitchell, R.T., McCormick, F.B., Peterson, D.W., Rising, M.A., Reber, C.A., Reysen, B.H.). Appl. No. PCT/US01/43279, 20 November 2001. 4 July 2002. 71 p.

Pate, B. 2001. Automating optoelectronic packaging. Journal of Surface Mount Technology, Vol. 14, No. 3, pp. 7–12.

Petermann, K. 1995. External optical feedback phenomena in semiconductor lasers. IEEE Journal of Selected Topics in Quantum Electronics, Vol. 1, No. 2, pp. 480–489.

Pezeshki, B., Vail, E., Kubicky, J., Yoffe, G., Zou, S., Heanue, J., Epp, P., Rishton, S., Ton, D., Faraji, B., Emanuel, M., Hong, X., Sherback, M., Agrawal, V., Chipman, C., Razazan, T. 2002. 20-mW widely tunable laser module using DFB array and MEMS selection. IEEE Photonics Technology Letters, Vol. 14, No. 10, pp. 1457–1459.

Powell, A. 2000. Modeling alignment shift of soldered optical fiber. Proceedings of 50th Electronic Components and Technology Conference, Las Vegas, USA, 21–24 May 2000. Pp. 997–1001.

Presby, H.M., Edwards, C.A. 1992a. Near 100 % efficient fiber microlenses. Electronics Letters, Vol. 28, No. 6, pp. 582–584.

Presby, H.M., Edwards, C.A. 1992b. Efficient coupling of polarization-maintaining fiber to laser diodes. IEEE Photonics Technology Letters, Vol. 4, No. 8, pp. 897–899.

Presby, H.M., Giles, C.R. 1993. Asymmetric fiber microlenses for efficient coupling to elliptical laser beams. IEEE Photonics Technology Letters, Vol. 5, No. 2, pp. 184–186.

Rantanen, T. 2000. Multiwavelength transmission in HFC networks. Teleste News & Views, No. 1, pp. 4–6.

Rassaian, M., Beranek, M.W. 1999. Quantitative characterization of 96.5Sn3.5Ag and 80Au20Sn optical fiber solder bond joints on silicon micro-optical bench substrates. IEEE Transactions on Advanced Packaging, Vol. 22, No. 1, pp. 86–93.

Ratowsky, R.P., Yang, L., Deri, R.J., Chang, K.W., Kallman, J.S., Trott, G. 1997. Laser diode to single-mode fiber ball lens coupling efficiency: full-wave calculation and measurements. Applied Optics, Vol. 36, No. 15, pp. 3435–3438.

Rodriguez-Moral, A., Bonenfant, P., Baroni, S., Wu, R. 2000. Optical data networking: protocols, technologies, and architectures for next generation optical transport networks and optical internetworks. Journal of Lightwave Technology, Vol. 18, No. 12, pp. 1855–1870.

Rupprecht, H., Woodall, J.M., Pettit, G.D. 1967. Efficient visible electroluminescence at 300°K from $Ga_{1-x}Al_xAs$ p-n junctions grown by liquid-phase epitaxy. Applied Physics Letters, Vol. 11, No. 3, pp. 81–83.

Ruprecht, P.A., Brandenburger, J.R. 1992. Enhancing diode laser tuning with a short external cavity. Optics Communications, Vol. 93, No. 1–2, pp. 82–86.

Saitoh, A., Gotoh, T., Tanaka, K. 2000. Chalcogenide-glass microlenses attached to optical-fiber end surfaces. Optics Letters, Vol. 25, No. 24, pp. 1759–1761.

Sasaki, J., Itoh, M., Tamanuki, T., Hatakeyama, H., Kitamura, S., Shimoda, T., Kato, T. 2001. Multiple-chip precise self-aligned assembly for hybrid integrated optical module using Au-Sn solder bumps. IEEE Transactions on Advanced Packaging, Vol. 24, No. 4, pp. 569–575.

Schicketanz, D., Schubert, J. 1972. Coupling losses between laser diodes and multimode glass fibres. Optics Communications, Vol. 5, No. 4, pp. 291 – 292.

Shah, V.S., Curtis, L., Vodhanel, R.S., Bour, D.P., Young, W.C. 1990. Efficient power coupling from a 980-nm, broad-area laser to a single-mode fiber using a wedge-shaped fiber endface. Journal of Lightwave Technology, Vol. 8, No. 9, pp. 1313–1318.

Shannon, G., Palen, E. 2002. Laser-weld attachment enables repeatable submicron precision. Optical Manufacturing, Vol. 1, No. 2, pp. 18–21.

Shaw, M., Galeotti, R., Coppo, G. 2001. Method of fixing an optical fibre in a laser package. Proceedings of 51st Electronic Components and Technology Conference, Orlando, FL., USA, 29 May – 1 June 2001. Pp. 1441–1446.

Shi, H.X., Cohen, D.A., Barton, J., Majewski, M., Coldren, L.A., Larson, M.C., Fish, G.A. 2002. Dynamic range of widely tunable sampled-grating DBR lasers. Electronics Letters, Vol. 38, No. 4, pp. 180–181.

Shiraishi, K., Ohnuki, H., Hiraguri, N., Matsumura, K., Ohishi, I., Kazami, H. 1997. A lensed-fiber coupling scheme utilizing a graded-index fiber and a hemispherically ended coreless fiber tip. Journal of Lightwave Technology, Vol. 15, No. 2, pp. 356–363.

Shiraishi, K., Kuroo, S-I. 2000. A new lensed-fiber configuration employing cascaded GI-fiber chips. Journal of Lightwave Technology, Vol. 18, No. 6, pp. 787–794.

Shuke, K., Yoshida, T., Nakano, M., Kawatani, A., Uda, Y. 1999. 1.5-M to 622-Mb/s fiber-optic transmitters and receivers packaged in reflow solderable surface mount housings. IEEE Journal of Selected Topics in Quantum Electronics, Vol. 5, No. 2, pp. 217–223.

Sidorin, Y., Howe, D. 1997. Diode-laser-to-waveguide butt coupling: extremely short external cavity. Applied Optics, Vol. 36, No. 18, pp. 4273–4277.

Sidorin, Y., Blomberg, M., Karioja, P. 1999a. Demonstration of a tunable hybrid laser diode using an electrostatically tunable silicon micromachined Fabry–Perot interferometer device. IEEE Photonics Technology Letters, Vol. 11, No. 1, pp. 18–20.

Sidorin, Y., Karioja, P., Blomberg, M. 1999b. Novel tunable laser diode arrangement with a micromachined silicon filter: feasibility. Optics Communications, Vol. 164, pp. 121–127.

Smith, D.R. 1982. Advances in optical fibre communications. Physics Bulletin, Vol. 33, pp. 401–403.

Smith, W.J. 2000. Modern optical engineering. 3rd ed. New York: McGraw–Hill. 617 p. ISBN 0-07-136360-2

Steele, R.V. 2003. Review and forecast of the laser markets, part II: diode lasers. Laser Focus World, Vol. 39, No. 2, pp. 63–76.

Streetman, B.G., Banerjee, S. 2000. Solid state electronic devices. 5th ed. Upper Saddle River, NJ: Prentice Hall. 558 p. ISBN 0-13-026101-7

Sumida, M., Takemoto, K. 1982. Lens aberration effect on a laser-diode-to-single-mode-fibre coupler. Electronics Letters, Vol. 18, No. 14, pp. 586–587.

Sunaga, Y., Takahashi, R., Tokoro, T., Kobayashi, M. 2000. 2 Gbit/s small form factor fiber-optic transceiver for single mode optical fiber. IEEE Transactions on Advanced Packaging, Vol. 23, No. 2, pp. 176–181.

Suzuki, M., Nakanishi, T., Tsuzuki, N., Murata, N. 1990. A stable laser module with UV-curable resin for single-mode subscriber use. Proceedings of 40th Electronic Components and Technology Conference, Las Vegas, NV., USA, 20–23 May 1990. Pp. 200–205.

Svelto, O. 1998. Principles of lasers. 4th ed. New York: Plenum Press. 604 p. ISBN 0-306-45748-2

Tan, M.R.T. 2002. Progress in long wavelength VCSELs. Proceedings of 15th Annual Meeting of the IEEE Lasers and Electro-Optics Society, 10–14 November 2002, vol. 1, pp. 269–270.

Tang, Z., Zhang, R., Shi, F.G. 2001a. Effects of angular misalignments on fiber-optic coupling alignment automation. Optics Communications, Vol. 196, pp. 173–180.

Tang, Z., Zhang, R., Mondal, S.K., Shi, F.G. 2001b. Optimization of fiber-optic coupling and alignment tolerance for coupling between a laser diode and a wedged single-mode fiber. Optics Communications, Vol. 199, pp. 95–101.

Tarraf, A., Riemenschneider, F., Strassner, M., Daleiden, J., Irmer, S., Halbritter, H., Hillmer, H., Meissner, P. 2004. Continuously tunable 1.55-µm VCSEL implemented by precisely curved dielectric top DBR involving tailored stress. IEEE Photonics Technology Letters, Vol. 16, No. 3, pp. 720–722.

Tohmori, Y., Ishii, H., Oohashi, H., Yoshikuni, Y. 2002. Wavelength-tunable semiconductor light sources for WDM applications. IEICE Transactions on Electronics, Vol. E85-C, No. 1, pp. 21–26.

Tummala, R.R., Rymaszevski, E.J. 1989. Microelectronics packaging handbook. New York: Van Nostrand Reinhold. 1194 p. ISBN 0-442-20578-3

Tunvic 2001. Micromechanical widely tunable VCSEL for WDM telecommunication systems. Internet document. 5 p.
Available at http://www.athene-darmstadt.de/tunvic/.

Uenishi, Y., Tsugai, M., Mehregany, M. 1995. Hybrid-integrated laser-diode micro-external mirror fabricated by ⟨110⟩ silicon micromachining. Electronics Letters, Vol. 31, No. 12, pp. 965–966.

Uenishi, Y., Honma, K., Nagaoka, S. 1996. Tunable laser diode using a nickel micromachined external mirror. Electronics Letters, Vol. 32, No. 13, pp. 1207–1208.

Vassallo, C., van der Keur, J.M. 1992. Ultimate coupling performances for microlensed fibers. Electronics Letters, Vol. 28, No. 20, pp. 1913–1915.

Vawter, G.A., Smith, R.E., Hou, H., Wendt, J.R. 1997. Semiconductor laser with tapered-rib adiabatic-following fiber coupler for expanded output-mode diameter. IEEE Photonics Technology Letters, Vol. 9, No. 4, pp. 425–427.

Ventrudo, B.F., Cassidy, D.T. 1993. Interference fringes in the far field of short-external-cavity InGaAsP diode lasers: a method for longitudinal mode control. Applied Optics, Vol. 32, No. 33, pp. 6620–6627.

Weidel, E. 1974. Light coupling from a junction laser into a monomode fibre with a glass cylindrical lens on the fibre end. Optics Communications, Vol. 12, No. 1, pp. 93–97.

Wenke, G., Zhu, Y. 1983. Comparison of efficiency and feedback characteristics of techniques for coupling semiconductor lasers to single-mode fiber. Applied Optics, Vol. 22, No. 23, pp. 3837–3844.

Wesström, J-O., Bergerengen, J., Sarlet, G., Gustafsson, Y., Szabo, P., Broberg, B. 2001. GCSRs and other widely tunable lasers. Digest of the LEOS Summer Topical Meetings, paper TuA2.2. 2 p.

Wesström, J-O., Hammerfeldt, S., Buus, J., Siljan, R., Laroy, R., de Vries, H. 2002. Design of a widely tunable modulated grating Y-branch laser using the additive Vernier effect for improved super-mode selection. IEEE 18th International Semiconductor Laser Conference. Pp. 99–100.

Wilson, R.G. 1998. Ball-lens coupling efficiency for laser-diode to single-mode fiber: comparison of independent studies by distinct methods. Applied Optics, Vol. 37, No. 15, pp. 3201–3205.

Wilson, G.C., Wood, T.H., Stiles, J.A., Feldman, R.D., Delavaux, J-M.P., Daugherty, T.H., Magill, P.D. 1999. FiberVista: an FTTH or FTTC system delivering broadband data and CATV services. Bell Labs Technical Journal, Vol. 4, No. 1, pp. 300–322.

Witham, C.R., Beranek, M.W., Carlisle, B.R., Chan, E.Y., Koshinz, D.G. 2000. Fiber-optic pigtail assembly and attachment alignment shift using a low-cost robotic platform. Proceedings of 50th Electronic Components and Technology Conference, Las Vegas, USA, 21–24 May 2000. Pp. 21–25.

Wongcharoen, T., Rahman, B.M.A., Rajarajan, M., Grattan, K.T.V. 2001. Spot-size conversion using uniform waveguide sections for efficient laser-fiber coupling. Journal of Lightwave Technology, Vol. 19, No. 5, pp. 708–716.

Yan, X., Mašanović, M.L., Skogen, E.J., Hu, Z., Blumenthal, D.J., Coldren, L.A. 2002. Optical mode converter integration with InP-InGaAsP active and passive

waveguides using a single regrowth process. IEEE Photonics Technology Letters, Vol. 14, No. 9, pp. 1249–1251.

Yang, J., Darveaux, R., Greenwood, J. 2002. Low cost uncooled mini-DIL module for pump laser. Proceedings of 52nd Electronic Components and Technology Conference, San Diego, CA., USA, 28–31 May 2002. Pp. 811–814.

Yariv, A. 1989. Quantum electronics. New York: John Wiley & Sons. 676 p. ISBN 0-471-60997-8

Yoda, H., Shiraishi, K. 2001. A new scheme of a lensed fiber employing a wedge-shaped gradient-index fiber tip for the coupling between high-power laser diodes and single-mode fibers. Journal of Lightwave Technology, Vol. 19, No. 12, pp. 1910–1917.

Yong-Qi, F., Bryan, N.K.A., Shing, O.N. 2000. Diffractive optical elements with continuous relief fabricated by focused ion beam for monomode fiber coupling. Optics Express, Vol. 7, No. 3, pp. 141–147.

Yong-qi, F., Bryan, N.K.A. 2001. Hybrid microdiffractive-microrefractive lens with a continuous relief fabricated by use of focused-ion-beam milling for single-mode fiber coupling. Applied Optics, Vol. 40, No. 32, pp. 5872–5876.

Zemax 2003. Zemax® optical design program. User's Guide, version February 4, 2003. San Diego, CA: ZEMAX Development Corporation. 569 p.

Zengerle, R., Hübner, B., Gréus, C., Burkhard, H., Janning, H., Kuphal, E. 1995. Monolithic integration of DFB laser with spot-size transformer for highly efficient laser fibre coupling. Electronics Letters, Vol. 31, No. 14, pp. 1142–1143.

Zhang, X.M., Liu, A.Q., Tang, D.Y., Lu, C. 2004. Discrete wavelength tunable laser using microelectromechanical systems technology. Applied Physics Letters, Vol. 84, No. 3, pp. 329–331.

Zory, P.S. (ed.). 1993. Quantum well lasers. San Diego, CA: Academic Press. 504 p. ISBN 0-12-781890-1

Appendix A: Diode laser tuning basics

Fundamental laser diode characteristics

Semiconductor lasers are key devices for optoelectronics due to their superior performance – such as small size, low power consumption, high efficiency, long lifetime, flexibility for selecting wavelength, and adaptability for photonic integrated circuits (Amann and Buus 1998, p. ix). Most lasers used in optical communications networks are based on materials that are compounds of elements from columns III and V of the periodic table. The emission wavelength is determined both by the properties of the gain medium and the physical structure of the laser cavity surrounding the active medium.

Quaternary alloys of InGaAsP can be grown lattice-matched on InP substrates, Figure A.1. Lattice matching to InP occurs if the Ga and As mole fractions are chosen such that (Amann and Buus 1998, p. 15)

$$x = \frac{0.452y}{1-0.031y}, \tag{A.1}$$

where x is the mole fraction of Ga and y is the mole fraction of As. Then the band gap energy E_g of $In_{1-x}Ga_xAs_yP_{1-y}$ can be approximated as (Amann and Buus 1998, p. 15)

$$E_g[eV] = 1.35 + 0.668x - 1.068y + 0.758x^2 \tag{A.2}$$
$$+ 0.078y^2 - 0.069xy - 0.332x^2y + 0.03xy^2 .$$

So, the variation of compositions on both the column III and column V sublattices provides the flexibility to choose a particular band gap while providing lattice matching to the substrate. The resulting band gaps range from 0.75 to 1.35 eV, which correspond to wavelengths from 920 to 1,655 nm. Fibre optic telecommunication lasers typically operate in the 1,310 nm or 1,550 nm transmission windows. In tunable lasers the band gap energy determines the maximum operating wavelength.
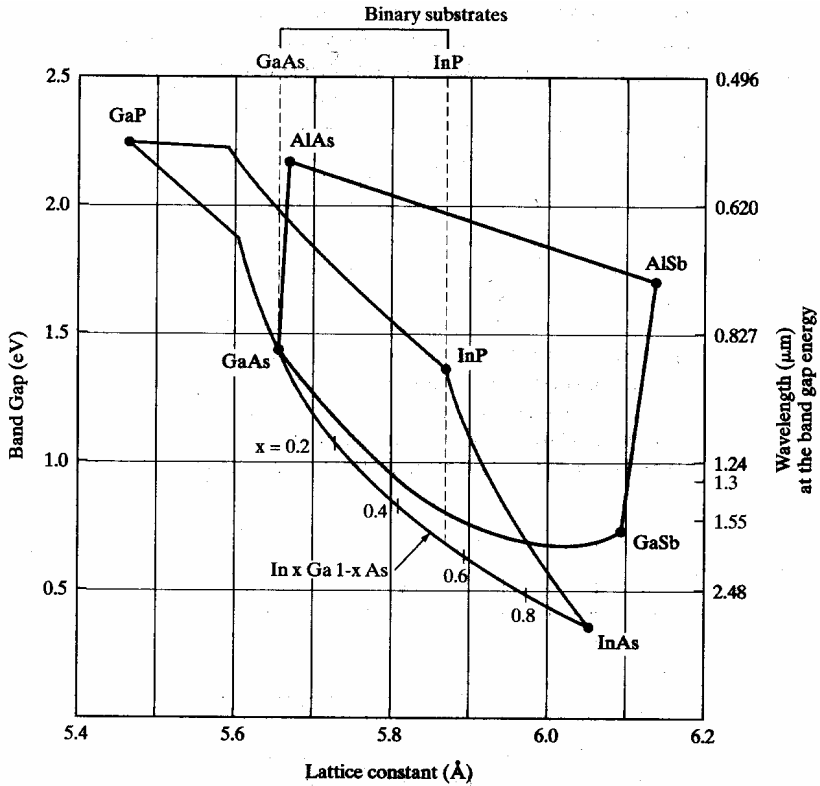
Figure A.1. Relationship between band gap and lattice constant for alloys in the InGaAsP and AlGaAsSb systems (Streetman and Banerjee 2000, p. 19).

The propagation of a monochromatic plane wave in an isotropic medium can be characterised by the complex propagation constant, which is also called the wave number (Amann and Buus 1998, p. 7)

$$\beta = k_0 n = k_0 (n' + jn'') , \tag{A.3}$$

where n is the complex refractive index of the medium, n' and n'' are the real and imaginary parts of the complex refractive index, and k_0 is the free-space propagation constant

$$k_0 = \frac{\omega}{c} = \frac{2\pi}{\lambda} , \tag{A.4}$$

where ω is the angular frequency of the wave, c is the free-space speed of light $\approx$ $3.0 \cdot 10^8$ m/s, and λ is the wavelength of the wave.

Assuming a uniform transverse electric and magnetic (TEM) plane wave, we can deduce (Amann and Buus 1998, p. 8) that the optical gain g and loss α are

$$g = -\alpha = 2k_0 n''. \qquad (A.5)$$

Electrons in solids obey Fermi-Dirac statistics that define the distribution of electrons over a range of permitted energy levels at thermal equilibrium. The Fermi-Dirac distribution function W(E) giving the probability that an available state at energy E will be occupied by an electron at absolute temperature T is (Streetman and Banerjee 2000, p. 81)

$$W(E) = \left[1 + \exp\left(\frac{E - E_F}{kT} \right) \right]^{-1}, \qquad (A.6)$$

where E_F is the energy of the Fermi level and k is Boltzmann's constant $\approx 1.38 \cdot 10^{-23}$ J/K. Thus an energy state at the Fermi level has a probability of ½ of being occupied by an electron.

In a semiconductor, optical gain may be achieved if the stimulated emission in a strongly pumped region exceeds the optical losses, which requires population inversion. This can be achieved by applying a forward bias into the p-n junction that injects electrons and holes into the transition region. The population inversion at a junction can be described using the concept of quasi-Fermi levels (Streetman and Banerjee 2000, p. 401). The occupation probability distributions for the charge carriers are

$$W_c(E) = \left[1 + \exp\left(\frac{E - E_{Fc}}{kT} \right) \right]^{-1} \quad \text{and} \qquad (A.7)$$

A3

$$W_v(E) = \left[1 + \exp\left(\frac{E - E_{Fv}}{kT} \right) \right]^{-1}, \qquad \text{(A.8)}$$

where $W_c(E)$ is the probability distribution and E_{Fc} is the quasi-Fermi level for electrons in the conduction band, and $W_v(E)$ is the probability distribution and E_{Fv} is the quasi-Fermi level for holes in the valence band.

The band structure and Fermi-Dirac occupation probability distributions in an inverted semiconductor are shown in Figure A.2. Band-to-band transitions only occur for photon energies

$$E = h\nu \geq E_g, \qquad \text{(A.9)}$$

where h is Planck's constant $\approx 6.63 \cdot 10^{-34}$ Js and ν is the frequency of the emitted radiation.
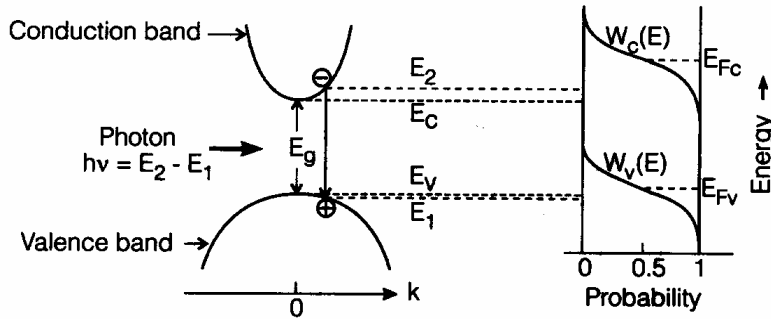
Figure A.2. Principal band structure and Fermi-Dirac distributions for an inverted semiconductor. Here, k denotes the electron wave vector (Amann and Buus 1998, p. 9).

The optical gain by stimulated emission for a photon with an energy hν dominates the absorption if the separation between the quasi-Fermi levels exceeds the band gap energy (Amann and Buus 1998, p. 10)

$$E_{Fc} - E_{Fv} \geq h\nu \geq E_g. \qquad \text{(A.10)}$$

The separation of the quasi-Fermi levels requires carrier injection by means of an electric current. The transition from absorption to gain occurs at $E_{Fc} - E_{Fv} = 0$ when the injected carrier density is denoted N_{tr} and is called the transparency carrier density. In InGaAsP lasers operating at 1,550 nm, N_{tr} is typically about 10^{18} cm^{-3} (Svelto 1998, p. 109).

Because of the energetic distribution of the occupied electronic states and the smooth transition of the Fermi-Dirac function, the resulting optical gain is spectrally broadened. Schematic semiconductor gain curves for various carrier densities neglecting phonon-assisted indirect transitions and any additional loss mechanisms are shown in Figure A.3.
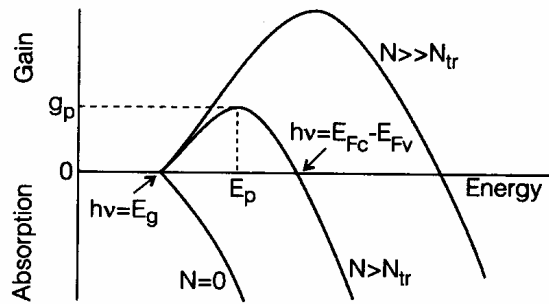
Figure A.3. Schematic optical gain curves for a semiconductor with carrier densities below and above N_{tr} (Amann and Buus 1998, p. 10).

The optical gain occurs in the energy range determined in Equation A.10 with the gain peak g_p at the gain peak photon energy E_p. Therefore, by increasing the injected carrier density we can widen the gain curve and the tunable wavelength range. For typical gain coefficients of interest in bulk semiconductor lasers ($20 \leq g \leq 80$ cm^{-1}) we can be reasonably approximate g_p as a linear function of N

$$g_p(N) = a(N - N_{tr}),$$ (A.11)

where a is the gain parameter that typically ranges from $1 \cdot 10^{-16}$ to $3 \cdot 10^{-16}$ cm^2 for InGaAsP at the 1,550-nm wavelength (Svelto 1998, p. 108). In Fabry–Perot lasers operating at this wavelength the gain curve is typically several tens of nanometers wide (Amann and Buus 1998, p. 26).

Zorabedian lists typical tuning ranges $\Delta\lambda_{tune}$ obtained from single bulk double-heterostructure (DH) laser material systems and emission centre wavelengths λ_c (Duarte 1995, p. 363). From these values he deduces an empirical expression for the maximum tuning range

$$\Delta\lambda_{tune} \approx 4.2\cdot10^{-5}\lambda_c^{\ 2}, \qquad (A.12)$$

where λ_c is given in nanometers. So, the typical maximum tuning range for the bulk DH laser operating at 1,550 nm is about 100 nm. The tuning range for the equivalent multiple quantum well (MQW) laser is 200 nm.

In transverse and lateral single-mode Fabry–Perot lasers the resonance conditions of the cavity defines a set of longitudinal modes (Amann and Buus 1998, p. 25)

$$\lambda_N = \frac{2n'_{eff}(\lambda_N)L}{N}, \qquad (A.13)$$

where N is an integer denoting the longitudinal mode number, λ_N is the wavelength of the Nth longitudinal mode, $n'_{eff}(\lambda_N)$ is the real part of the effective refractive index at λ_N, and L is the physical length of the cavity. Because the cavity of the edge emitting lasers is very long compared with the emission mode wavelengths, the longitudinal mode number is usually large. For example, if the cavity length is 700 μm and $n'_{eff}(1{,}550\,\text{nm}) = 3.3$, we can calculate that at 1,550 nm wavelength $N \approx 3{,}000$.

Considering a relatively small number – such as 10 – of longitudinal modes centred at λ_N, Equation A.13 defines a comb-shaped mode spectrum with an almost constant mode spacing (Amann and Buus 1998, p. 25)

$$\Delta\lambda_m = \lambda_N - \lambda_{N+1} \approx \frac{\lambda_N^{\ 2}}{2n_{g,eff}L}, \qquad (A.14)$$

where

$$n_{g,eff} = n'_{eff}(\lambda_N) - \lambda_N \frac{dn'_{eff}}{d\lambda}\bigg|_{\lambda_N} \tag{A.15}$$

is the effective group index that includes the dispersion of $n'_{eff}(\lambda)$ around λ_N.

Typically, $n'_{g,eff}(1{,}550\ nm) \approx 4$, so that when the cavity length is 700 μm, $\Delta\lambda_m$ equals to 0.43 nm. Because the gain curve of the active material is much wider than the mode spacing, the laser operation is usually not single-mode but occurs with different amplitudes in many longitudinal modes. The emission spectrum of the laser with the gain peak wavelength λ_p equal to λ_N is shown in Figure A.4. While the longitudinal mode at $\lambda_N = \lambda_p$ exhibits the largest power, the neighbouring modes can also carry a significant part of the total laser emission.
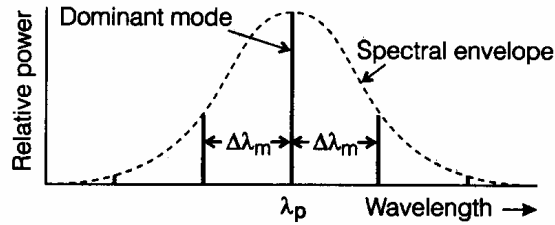
Figure A.4. Longitudinal emission spectrum of Fabry–Perot laser diode (Amann and Buus 1998, p. 26).

The width of the spectral envelope depends on the breadth of the gain bandwidth of the active medium. The multimode spectrum of the InGaAsP FP lasers operating at 1,550-nm usually extends over a few nanometers and the emission occurs in about 4 to 10 longitudinal modes (Amann and Buus 1998, p. 26).

The longitudinal modes have a finite line width caused by the spontaneous emission into the lasing mode. Whereas photons generated by the stimulated emission add in phase to the lasing mode, the phase associated with a spontaneously released photon is random. The line shape is mainly Lorentzian and the Schawlow–Townes–Henry line width for diode lasers $\Delta\nu_{STH}$ can be written as (Amann and Buus 1998, p. 70)

$$\Delta v_{STH} = \frac{h v_g{}^2 (\alpha_i + \alpha_m) \alpha_m n_{sp}}{8\pi P_1} \left(1 + \alpha_H{}^2\right), \qquad (A.16)$$

where $v_g = c/n_{g,eff}$ is the group velocity of the photons, α_i is the internal loss of the cavity, α_m is the end face mirror loss, P_1 is the optical power per facet, n_{sp} is the spontaneous emission coefficient, and α_H is the correction factor for diode lasers.

We can calculate at 1,550 nm when $n_{g,eff} = 4$, $\alpha_i = \alpha_m = 30$ cm^{-1}, $n_{sp} = 2.5$, $\alpha_H = 6$, and $P_1 = 1$ mW, that $\Delta v_{STH} \approx 50$ MHz, which corresponds to a wavelength band of $0.4 \cdot 10^{-3}$ nm. This means that the fundamental lower limit for the diode laser line width is very low, if we compare it to the DWDM specifications where the basic channel separation is 100 GHz (ITU 1998).

The development of modern epitaxial techniques allowed the controlled growth of semiconductor heterostructures on the atomic scale and it became possible to produce very thin layer structures, quantum wells (QW), in which quantization effects of the confined carriers occur. This yields larger optical gain per electron-hole pair and lower threshold currents than in the bulk lasers (Amann and Buus 1998, p. 33). QW lasers are important in almost every application because of their better performance over conventional laser diodes. The physics and applications of quantum well lasers are treated in many textbooks, such as (Yariv 1989, Zory 1993).

Tuning schemes

After the successful development of InGaAsP single-mode laser diodes in the early 1980s, the realisation of electronically tunable lasers became an important issue of worldwide research (Kobayashi and Mito 1988). This effort has mainly been driven by the increasing demand on transmission capacity in optical communications systems.

A simplified schematic representation of what users expect from an electronically tunable laser is shown in Figure A.5. For most applications, a single-mode light source is required with two control currents or voltages that

define the optical power and wavelength separately and independently. Therefore, the optical power should only depend on the control current I_a, while the laser wavelength should only be dependent on the tuning current I_t.

Keeping the laser current constant, the wavelength should be a smooth and hysteresis-free function of the tuning current, Figure A.5b. At a constant tuning current, the optical power vs. laser current characteristics should show a linear dependence on I_a above the threshold current I_{th} with constant emission wavelength, Figure A.5c.
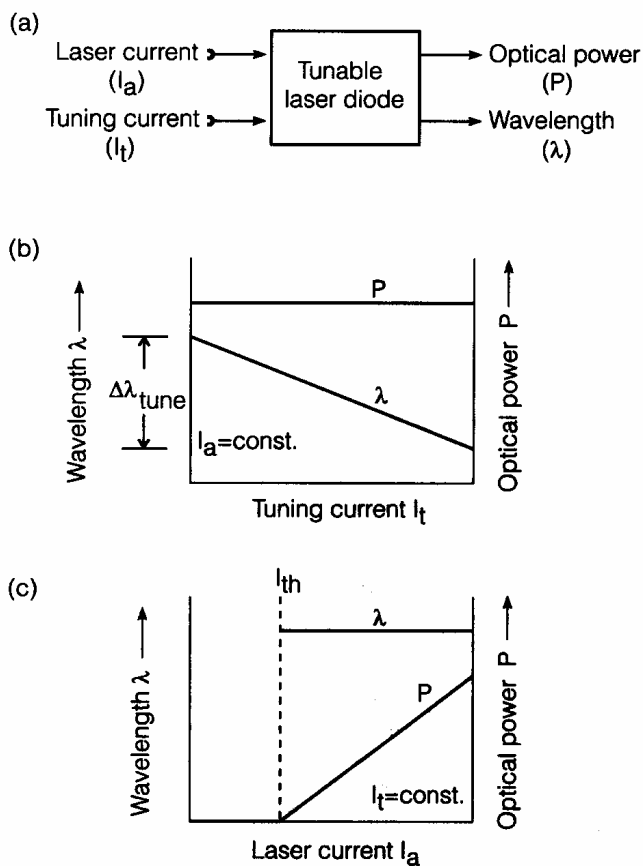
Figure A.5. Idealised tunable laser diode. a) Schematic diagram, b) relationship between wavelength and power when laser current is constant and c) relationship between power and wavelength when tuning current is constant (Amann and Buus 1998, p. 2).

Experience has shown that such an ideal performance is difficult to obtain. The wavelength tuning mechanisms in laser diodes generally affect the optical losses, so that the optical power changes during tuning. Equally, the optical power control by the laser current affects the device temperature and thus the emission wavelength (Amann and Buus 1998, p. 3).

In addition, the electronic tuning can lead to wavelength jumps or hysteresis effects. The continuous tuning may require the precise and simultaneous adjustments of multiple wavelength control currents. Because the wavelength depends on temperature and device ageing, this makes the use of the device complicated. As with other electronic components, comfortable use of the device is one of the most important characteristics in practice, and this can decisively influence their suitability to commercial applications (Amann and Buus 1998, p. 3).

Depending on how the tuning is performed and which device structure is used, we can distinguish between three basic schemes: continuous, discontinuous and quasi-continuous tuning, Figure A.6. The ideal tuning scheme for most practical applications is the continuous tuning. Here the laser wavelength is tuned smoothly in small steps without mode changes, while all other laser parameters are kept as constant as possible. The small step means that the wavelength increment is smaller than the laser line width (Equation A.16).
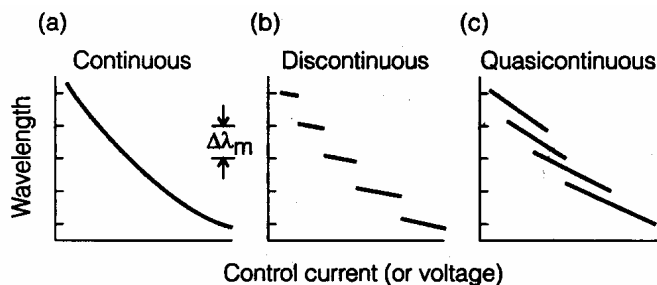

Figure A.6. Tuning schemes. a) Continuous, b) discontinuous and c) quasi-continuous (Amann and Buus 1998, p. 76).

Continuous tuning requires the simultaneous mutual adjustment of the cavity gain peak wavelength and the comb-mode spectrum. Due to the stringent requirements, the tuning range is smallest in this tuning scheme and seems to be limited to about 15 nm at 1,550-nm wavelength (Amann and Buus 1998, p. 77).

Larger tuning ranges can be achieved by allowing for longitudinal mode changes during tuning, Figure A.6b. Now, the tunability of the comb-like spectrum represents no limitation on the total tuning range, which is determined solely by the cavity gain characteristics. Therefore, tuning spans over 200 nm have been obtained in the 1,300 ... 1,550-nm wavelength range (Lin et al. 2002a). Unfortunately, with this tuning scheme, it is not possible to access all wavelengths within the tuning range.

An intermediate tuning behaviour can be achieved with the quasi-continuous tuning scheme, Figure A.6c. This is accomplished by joining overlapping small regions that are continuously tunable within a single longitudinal mode to achieve large wavelength coverage. Here the total tuning range is limited by the tunability of the cavity gain characteristics, while the tuning of the comb-mode spectrum only occurs over about one longitudinal mode spacing.

Author(s)
Heikkinen, Veli

Title
Tunable laser module for fibre optic communications

Abstract

This thesis deals with the design, realisation, and testing of the wavelength tunable 1540-nm laser prototypes that are intended for fibre optic communications. The short external cavity laser uses an electrically controlled silicon micromachined Fabry–Perot interferometer (FPI) device as the tuning element. First, the most common techniques for the diode laser wavelength tuning and applications for these devices are reviewed. Then the ways of coupling laser power into the single-mode (SM) optical fibre are considered and the characteristics of the fibre attachment methods are studied. The design, assembly and testing of three prototypes is introduced. Their discontinuous tuning spans range between 8 and 13 nm and their output power between 100 and 570 µW. The modules produce multimode tuning having an rms spectral width of about 1 nm. In addition, one prototype is capable of single-mode tuning with a side mode suppression ratio of 26 dB. The measured wavelength span is the widest reported single-mode tuning range obtained from a short external cavity Fabry–Perot diode laser without temperature tuning. The laser module can be electrically modulated up to over 600 MHz. The test results show that the FPI-tuned diode lasers can provide a cost-effective solution for optical communication applications. The study also confirms that it is possible to realise the laser-to-SM-fibre coupling using adhesive bonding. Further studies are needed in order to improve the speed and repeatability of the process together with the reliability of the fibre attachment. In addition, the operational and long-term reliability of the module must be characterised.

This thesis deals with the design, realisation, and testing of the wavelength tunable 1540-nm laser prototypes that are intended for fibre optic communications. The short external cavity laser uses an electrically controlled silicon micromachined Fabry-Perot interferometer (FPI) device as the tuning element. First, the most common techniques for the diode laser wavelength tuning and applications for these devices are reviewed. Then the ways of coupling laser power into the single-mode (SM) optical fibre are considered and the characteristics of the fibre attachment methods are studied. The design, assembly and testing of three prototypes is introduced. Their discontinuous tuning spans range between 8 and 13 nm and their output power between 100 and 570 µW. The modules produce multimode tuning having an rms spectral width of about 1 nm. In addition, one prototype is capable of single-mode tuning with a side mode suppression ratio of 26 dB. The measured wavelength span is the widest reported single-mode tuning range obtained from a short external cavity Fabry-Perot diode laser without temperature tuning. The laser module can be electrically modulated up to over 600 MHz. The test results show that the FPI-tuned diode lasers can provide a cost-effective solution for optical communication applications. The study also confirms that it is possible to realise the laser-to-SM-fibre coupling using adhesive bonding. Further studies are needed in order to improve the speed and repeatibility of the process together with the reliability of the fibre attachment. In addition, the operational and long-term reliability of the module must be characterised.

Veli Heikkinen